

**An iterative-triple-energy window approach to cross-talk correction in quantitative small animal Tc-99m and In-111 single photon emission computed tomography**

By

**Paul Prior**

A thesis submitted to  
The Faculty of Graduate and Postdoctoral Affairs  
In partial fulfillment of the requirements for the degree of

**Master of Science**

**in**

**Medical Physics**

Carleton University  
Ottawa, Ontario

© 2014, Paul Prior

# Abstract

---

Dual isotope Single Photon Emission Computed Tomography (SPECT) permits *in vivo* measurements of two separate signals simultaneously, but the quantitative accuracy of these measurements is degraded due to the presence of cross-talk. An iterative-triple-energy window (TEW) method was developed to correct for cross-talk in In-111 and Tc-99m dual-isotope SPECT. The correction was evaluated in comparison to other TEW-based methods in phantoms and *in vivo*. In phantoms containing different  $\frac{Tc-99m}{In-111}$  activity fractions, scattered In-111 photons falsely detected as Tc-99m (cross-talk) resulted in an over-estimation of Tc-99m activity by up to 80%. Application of the iterative TEW resulted in quantification of total Tc-99m activity within 5% of the truth across the largest range of activity fractions. *In vivo*, modified TEW and iterative TEW both quantified total heart Tc-99m activity within 5% in a rat, but the iterative TEW was superior to the modified TEW in removing cross-talk in regions of mostly In-111.

# Acknowledgements

---

First and foremost, I'd like to thank my supervisor, Glenn Wells, for his constant advice and criticism of this work.

I'd like to thank Daniel Duan for his help with the well-counter measurements and trouble-shooting with this device. Also, thank you to Dan and Lihui Wei for producing the In-111 liposome, used in the *in vivo* portion of this study.

I'd also like to thank Julia Lockwood for her help with learning to use the SPECT camera, in setting up some phantom experiments, as well as her work handling the small animals in the *in vivo* portion of this study.

Thanks also to Rachel Timmins for getting me up to speed on this project and helping me with some intricacies.

Thanks to Jared for letting me use his SPECT and CT reconstruction software. This project would not have been possible without this, as well as his help in figuring out some of the intricacies of his software.

Also, thanks to Tong Xu for reading and providing feedback on a draft of this thesis.

Last but not least, thanks to my friends and family for all the moral support!

# Statement of Originality

---

I wrote the MATLAB script in order to apply the iterative TEW mentioned throughout the study. I also wrote the code to perform a modified version of the template-based Partial Volume Effect Compensation developed by Shcherbinin [1].

I performed the experiments to determine the energy resolution of each camera head, and also carried out the analysis on these experiments by myself. Most of the well-counter measurements were done by Daniel Duan. I did most of the analysis for calibration of the well-counter for the energy window used, but Daniel also played a role in this.

Julia Lockwood taught me to use the SPECT camera and dose calibrator. Once I was more comfortable, most of the camera operation was done by me. I designed and performed the data acquisition and analysis for the phantom portion of the study. During the *in vivo* part of this study, Julia was responsible for the animal care and injection of the rats with the radioisotopes during the *in vivo* SPECT work as well as the excision of the rat heart. I cut the rat hearts into samples and performed the planar SPECT acquisitions on the tools and samples. The segmentation of the rat SPECT images was done manually by me. I also carried out all of the analysis for the determination of the gold standard (gamma counter) Tc-99m activity in each heart.

Jared Strydhorst wrote the SPECT and CT reconstruction programs used throughout the study.

I have presented this work twice in the form of a poster:

1. P. Prior and R. G. Wells, "A modified iterative Triple Energy Window (TEW) approach to cross-talk correction in dual isotope In-111/Tc-99m small animal SPECT," in *Imaging Network of Ontario proceedings of the 12<sup>th</sup> ImNO Symposium*, pp 106, 2014.
2. P. Prior, R. Timmins, R. G. Wells, "An iterative Triple Energy Window (TEW) Approach to Cross-talk Correction in Small Animal Tc-99m and In-111 SPECT," in *University of Ottawa Heart Institute's 27<sup>th</sup> Annual Research Day Abstract Booklet*, pp 20, 2014.

I have also presented this work twice in the form of oral presentations:

1. P. Prior, R. Timmins, R. G. Wells, "An iterative triple energy window (TEW) approach to cross-talk correction in quantitative small animal Tc-99m and In-111 SPECT," in *2014 Molecular Function & Imaging Symposium Program Book*, pp 20, 2014.
2. P. Prior, R. Timmins, R. G. Wells, "An iterative triple energy window (TEW) approach to cross-talk correction in quantitative small animal Tc-99m and In-111 SPECT," in *COMP 2014 Conference proceedings*, pp 13, 2014.

# Table of Contents

---

Abstract.....	i
Acknowledgements.....	iii
Statement of Originality.....	iv
List of Tables.....	viii
List of Figures.....	ix
Glossary of Acronyms.....	xiii
1 Introduction .....	15
1.1 Small Animal Research.....	16
1.2 Tracers in Nuclear Medicine.....	17
1.3 Photon Interactions with Matter.....	18
1.3.1 Photoelectric Effect.....	18
1.3.2 Compton Scatter.....	19
1.3.3 Pair Production.....	20
1.4 The Gamma Camera.....	21
1.4.1 Collimator .....	22
1.4.2 Scintillation Detectors.....	26
1.4.3 Photomultiplier Tubes.....	27
1.4.4 Event Positioning/Energy Information .....	28
1.5 Energy Windowing .....	29
1.6 Dual-Isotope SPECT .....	30
1.7 Image Reconstruction.....	31
1.7.1 Filtered Back-Projection .....	31
1.7.2 Iterative Methods .....	33
1.8 Photon Attenuation Correction.....	34
1.9 Scatter Compensation Methods.....	37
1.9.1 Adjusting the Attenuation Map.....	39
1.9.2 DEW .....	39
1.9.3 TEW .....	40

1.9.4	Modified TEW .....	42
1.9.5	Convolution Methods.....	45
1.9.6	Analytic Models.....	46
1.9.7	Monte-Carlo (MC) Methods.....	46
1.9.8	Effective Scatter Source Estimation (ESSE) .....	47
1.9.9	Iterative TEW.....	48
1.10	Partial Volume Effect Compensation (PVEC).....	52
1.10.1	Avoiding the problem .....	55
1.10.2	Fixing the problem at the source.....	56
1.10.3	Template-Based approach.....	56
1.11	<i>Ex-Vivo</i> Validation tools in SPECT .....	58
1.11.1	Well counter (gamma counter) .....	59
1.11.2	Dose Calibrator .....	61
1.12	Objectives/Hypotheses .....	61
2	Methods and Materials .....	63
2.1	Scatter and Calibration Constants .....	63
2.2	Phantom Validation.....	67
2.2.1	Phantom Preparation.....	68
2.2.2	Data Acquisition .....	69
2.2.3	Image Processing .....	70
2.2.4	Image Analysis.....	72
2.3	<i>In vivo</i> Validation.....	76
2.3.1	Animal Model .....	76
2.3.2	Data Acquisition .....	77
2.3.3	Image Processing .....	81
2.3.4	Analysis.....	85
3	Results .....	87
3.1	Scatter and Calibration Constants .....	87
3.2	Phantom Validation.....	92
3.3	<i>In Vivo</i> Validation .....	103
4	Discussion.....	111

5	Conclusions and Future Directions.....	122
5.1	Conclusions .....	122
5.2	Future Directions.....	123
	References .....	126

# List of Tables

---

Table 1-1: Common radio-isotopes used in SPECT [8] .....	17
Table 2-1: Activities used in the mixed isotope phantom experiment are shown below. Errors represent the error in calibration for each isotope, quoted in the owner's manual.	68
Table 2-2: Energy windows used for all experiments .....	70
Table 2-3: Mass, heart mass, Tc-99m injected activity and In-111 injected activity of each rat. ....	79
Table 3-1: Detector response to 140keV Tc-99m photons and 171keV In-111 photons.	90
Table 3-2: Cross-talk fractions with different corrections applied. ....	95
Table 3-3: Comparison of iterative TEW (ITER) to modified TEW (MOD) across the different activity fractions based on total activity and accuracy of activity estimate. ....	102
Table 3-4: Fractional activity present in samples, as well as gold standard activities for each rat, decay corrected to the beginning of the 4 <sup>th</sup> helical SPECT acquisition. The asterisk represents the larger uncertainty present in rat 4 gold standard activity measurement due to one of the samples being counted outside of the linear range of the well-counter. ....	108
Table 3-5: Normalized activity recovery for total-heart activity compared against the well-counter measurements .....	109
Table 3-6: Residual scatter left in the LV cavity by three different scatter-subtracted images: modified TEW, iterative TEW, and standard TEW. ....	109

# List of Figures

---

Figure 1-1: Depiction of Compton Scatter. An incident photon scatters off of a loosely-bound electron and ends up with direction  $\theta$ , donating energy to the electron. .... 20

Figure 1-2: A 2-D schematic of the principal function of the parallel-hole collimator. It is designed to accept photons (arrows) traveling perpendicular to the detector-crystal surface by absorbing photons that do not have this desired direction. .... 22

Figure 1-3: Configuration of a single-pinhole collimator. In this diagram, the star represents a radioactive source,  $h$  is the pinhole-to-source distance,  $f$  is the focal length of the pinhole,  $d$  is the width of the pinhole, and  $\alpha$  is the acceptance angle of the pinhole. . 26

Figure 1-4: The charge amplification process accomplished by a PMT with 5 dynodes. Light photons interact at the photocathode to produce electrons via the photoelectric effect. The arrows represent the electron paths, and the number of electrons increases after interacting with each dynode. The electrons are accelerated by a high potential difference,  $\Delta V_i$ , across each dynode. .... 27

Figure 1-5: “Energy-windowing” to produce separate projections for hypothetical isotopes A and B. In the absence of scatter, the activity distributions of A and B can be accurately quantified by separately reconstructing the projections in window A and window B. .... 30

Figure 1-6 Left: The true source distribution. Centre: Back-projection, 128 projections. 32

Figure 1-7: Schematic of an energy spectrum resulting from a dual isotope acquisition of Tc99m (140keV emission) & In111 (171 and 245keV) is the solid black line. The resulting Tc99m activity is overestimated due to a combination of self-scatter, as well as cross-talk caused by In111 scatter into the Tc99m window. Scatter is shown as the dotted line. .... 38

Figure 1-8: Simplified version of a Tc99m & In111 spectrum. The total counts are the solid black line, and the dotted curve is the contribution of scatter to the detected counts. The narrow windows surrounding the Tc-99m window ( $Scat_{low}$  and  $Scat_{high}$ ) are the TEW scatter windows. In this setup, scatter is over-estimated due to the presence of un-scattered photons in the scatter windows. .... 41

Figure 1-9: Depiction of the overlap of Tc-99m and In-111 un-scattered photons into the TEW high scatter window due to the proximity of the photo-peaks of the respective isotopes. The shaded regions represent the parts of the un-scattered photon energy distribution that are incorrectly assumed to be scattered photons. .... 44

Figure 1-10: Simplified version of a Tc99m & In111 (245keV emission omitted) spectrum. The total counts are the solid black line, and the dotted curve is the contribution of scatter to the detected counts. The small windows surrounding the Tc-99m window ( $Scat_{low}$  and  $Scat_{high}$ ) are the TEW scatter windows. .... 50

Figure 1-11: Depiction of the NSA filter. It takes a negative projection element (-e) and spreads the negative value evenly with each of its immediate neighbours, replacing its value with 0.....	51
Figure 1-12: Simulated representation of PVE. The total activity of the true source (dashed line) is under-estimated because some photons originating within the ROI are placed outside the ROI in the reconstructed image due to non-zero spatial resolution of the system.....	53
Figure 1-13: PVE with three neighbouring structures. Due to finite spatial resolution, there is a bias in SPECT activity estimates due to counts from the ROI placed outside the ROI in the reconstructed image, as well as counts from neighbouring structures detected within the ROI.....	54
Figure 2-1: Simplified version of a Tc99m & In111 (245keV emission omitted) spectrum. The total counts are the solid black line, and the dotted curve is the contribution of scatter to the detected counts. The small windows surrounding the Tc-99m window (Scat <sub>low</sub> and Scat <sub>high</sub> ) are the TEW scatter windows. ....	63
Figure 2-2: Depiction of the NSA filter. It takes a negative projection element (-e) and spreads the negative value evenly with each of its immediate neighbours, replacing its value with 0.....	63
Figure 2-3: The plastic cylinder phantom used in the study.....	67
Figure 2-4: ROI used to determine activity of plastic cylinder phantoms (blue). The grayscale image is the CT scan and the jet colour-map image is the co-registered SPECT image, with voxel intensities normalized to 1. Left: ROI used in avoiding the partial volume effect. Right: ROI used when PVEC is applied. SPECT image is left out on the right for easier comparison of the ROI to the CT image. ....	72
Figure 2-5: Block diagram describing the SPECT/CT acquisition process for each rat. A CT scan was acquired for attenuation correction and anatomical information. Four SPECT acquisitions were done for each rat: two with only Tc-99m-tetrofosmin present, and two with both Tc-99m-tetrofosmin and In-111-liposome present. ....	79
Figure 2-6: Tc-99m planar gamma camera image of background (left), tools (centre), samples (right). Quantitative information from these acquisitions was used to determine the fraction of Tc-99m heart activity retained in the samples after sectioning the heart into 40 pieces.....	80
Figure 2-7 top: Coronal (bottom-left), sagittal (top-left), and transverse (right) slices of the heart (colour) after iterative TEW scatter correction co-registered with CT reconstruction (grayscale). The SPECT image is scaled such that the maximum voxel intensity value is 100. ....	82
Figure 2-8: 3-D-rendered image of the heart ROI used to aid in manual segmentation of myocardia in SPECT images. ....	83
Figure 2-9: 3-D surface used to estimate average background activity in template-based PVEC (red ROI). Left to right: trans-axial, coronal, sagittal slices.....	84

Figure 3-1: Energy spectra of the different camera heads in response to 140keV Tc99m photons. The red dots are the Counts/keV acquired in each bin, the solid black line is the result of the Gaussian + Linear fit of the spectrum, and the dashed black line is the Gaussian portion of the fit, which represents the scatter-subtracted energy spectrum. .... 88

Figure 3-2: Energy spectra of the different camera heads in response to 171keV In-111 photons. The red dots are the Counts/keV acquired in each bin, the solid black line is the result of the Gaussian + Linear fit of the spectrum, and the dashed black line is the Gaussian portion of the fit, which represents the scatter-subtracted energy spectrum. .... 89

Figure 3-3: Calibration curve between gamma counter (cpm) and dose calibrator ( $\mu$ Ci). 91

Figure 3-4: View of the central coronal slice of the plastic cylinder phantom containing only In111. (a) is the In111 window image, (b) is the uncorrected Tc99m image, (c) is the Tc99m image with modified TEW applied, (d) is the Tc99m image with iterative TEW applied, and (e) is the Tc99m image with standard TEW applied. The intensity values are transformed using the natural logarithm in order to view the full range of counts. .... 93

Figure 3-5: The amount of cross-talk present as a function of the depth from the top of the container. The left side represents slices selected at the top of the phantom, while the right sides of the curves represent slices selected at the bottom of the phantom. .... 94

Figure 3-6: Comparison of the different correction methods in projection space. For each TEW-based method, the residual cross-talk fraction is determined after conserving counts, truncating negatives, and after doing selective mean filtering before truncating with projections a) not pre-filtered, and b) pre-filtered with a 2D Gaussian function ( $\sigma = 0.5 \text{ mm}$ ). All errors are  $<0.0001$ . .... 97

Figure 3-7: The effect of filtering projections analyzed in projection space. Error for all residual scatter measurements assuming Poisson counting statistics was  $< 0.001$  and therefore error bars are too small to be seen in this figure. .... 98

Figure 3-8: Quantitative results of the mixed Tc99m/In111 phantom experiment. Without correction for scatter, In-111 activity is overestimated by less than 5%, but is not dependent on the Tc-99m activity present. Without scatter correction, measured Tc-99m activity is dependent on the relative activity of In-111. Standard TEW consistently over-subtracts. Modified TEW and iterative TEW produce similar results if the Tc-99m/In-111 activity fraction is  $> 1$ . Iterative TEW is significantly more accurate in phantoms with activity fractions  $< 1$ . .... 100

Figure 3-9: Central coronal and trans-axial slices of rat 1 images. The left images are uncorrected for scatter before the injection of In-111-liposome. The right side shows the reconstructed images after the injection of In-111 liposome uncorrected for scatter, with modified TEW scatter correction, and with iterative TEW scatter correction. The injection of In111 degrades contrast between the myocardia and heart chambers in the uncorrected Tc99m image. The modified TEW and iterative TEW visually restore the lost contrast. .... 103

Figure 3-10: TACs for total-heart SPECT Tc99m activity, normalized to the total heart activity in the uncorrected images from scan 1 for each rat. Vertical error bars represent standard deviation of the mean normalized activity between the 6 rats. Horizontal error bars represent the standard error on the time of each acquisition since the start of scan 1. Uncorrected for cross-talk, the uncorrected Tc-99m activity increased noticeably after the injection of In-111-liposome. Corrections for cross-talk all removed this increase, and restored the general exponential clearance. .... 104

Figure 3-11: Curve stripping used to delineate Tc99m activity from In111 activity. Error bars representing Poisson noise in counting and summing 40 samples for each data point are too small to be seen. Beyond day 2, it is assumed that only In-111 activity is present (diamonds). The data in this time-range is used to model the In-111 count-rate present between day 0 and day 2 (dashed line). Tc-99m count-rate (dots) is determined by subtracting the In-111 model from the measured total count-rate (squares). .... 106

Figure 3-12: Fraction of counts retained in samples based on the planar gamma camera acquisitions. The modified TEW results (right hand side) were used to determine the fraction of total activity that was retained in the samples after physically sectioning each of the hearts into 40 pieces. .... 107

Figure 4-1: Depiction of a scatter spectrum that would result in a TEW under-correction due to the non-ideal assumption that the scatter profile (dashed line) between the scatter windows (boxes) is linear (solid line). .... 114

Figure 4-2: Determining the sensitivity of the normalized activity recovery to  $\epsilon$ , the scaling of the estimated proportion of In-111 primary counts appearing in  $Scat_{high}$ . .... 116

# Glossary of Acronyms

---

CAD	Coronary Artery Disease
CT	Computed Tomography
DEW	Dual Energy Window
ESSE	Effective Scatter Source Estimation
FBP	Filtered-Back-Projection
FOV	Field of View
HEAP	High-Energy, All-Purpose
LEAP	Low-Energy, All-Purpose
LEHR	Low-Energy, High-Resolution
LV	Left Ventricle
MC	Monte Carlo
MEAP	Medium-Energy, All-Purpose
MLEM	Maximum Likelihood Expectation Maximization
NSA Filter	Negative-Selective-Averaging Filter
OSEM	Ordered Subset Expectation Maximization
PET	Positron Emission Tomography
PMT	Photomultiplier Tube
PVE	Partial Volume Effect
PVEC	Partial Volume Effect Correction/Compensation
RV	Right Ventricle
SPECT	Single Photon Emission Computed Tomography
TAC	Time Activity Curves
TEW	Triple Energy Window
XTF	Cross Talk Fraction

# 1 Introduction

Single Photon Emission Computed Tomography (SPECT) is a noninvasive functional imaging modality that is commonly used to aid in the diagnosis of cardiac disorders, tumors, and infections. As a noninvasive modality, SPECT allows us to see inside the body without the risks inherent in surgery<sup>1</sup> [2]. As a functional imaging modality, SPECT is used to analyze biological function, rather than observe anatomical structure. In contrast to x-ray-based modalities which image anatomical structure based on the differential attenuation of an external photon source, the signal in SPECT comes from photons emitted inside the scanner's field of view (FOV). The detected photons are the gamma emissions of radioactive isotopes. Radioactive isotopes can often be attached to biological molecules, called tracers, by a radio-chemist without affecting the important functions of the molecules. Detection of the isotopes by their emissions is then used to infer the bio-distribution of the tracer and evaluate the biological function under study. Depending on the type of SPECT acquisition, the tracer images can be used to aid doctors in the diagnosis of disease, and can also be used in fundamental biological research with small animal models.

This thesis begins by covering the background material fundamental to research in small animal SPECT (chapter 1). This includes the applications of small animal SPECT in the field of molecular biology, the important steps in the imaging chain (the emission, detection, reconstruction, and interpretation of the signal), as well as essential

---

<sup>1</sup> Not everyone characterizes nuclear imaging as noninvasive, due to act of injecting activity into the patient that is involved in SPECT procedures.

physical processes that must be corrected for in quantitative SPECT studies. This thesis addresses the problem of cross-talk in dual-isotope SPECT which occurs when Compton scattered photons from a higher-energy-emitting isotope are detected in a window designated for a lower-energy-emitting isotope, resulting in an overestimate of activity of the lower-energy-emitting isotope. Section 1.9 reviews common methods that have been used to correct for scatter and cross-talk, and presents a solution to the problem (iterative triple-energy-window correction, section 1.9.9) for dual isotope SPECT studies using Tc-99m and In-111 as the radioactive tracers. The iterative TEW correction method was validated in phantom studies<sup>2</sup> as well as *in vivo* in a rat's heart. The methods describing the validation experiments are given in chapter 2. Experimental data and results of the analysis are presented in chapter 3, and a discussion of the results is in chapter 4. Conclusions, the future of scatter correction and the contribution of SPECT to small animal research are explored in chapter 5.

## 1.1 Small Animal Research

SPECT plays an important role in small animal research. The parallels between the genetic make-up of humans and other animals have been well documented, and are the focus of many studies [3, 4, 5]. For example, since the mouse genome was mapped in 2002—1 year following the complete mapping of the human genome— the mouse genome has been altered in order to mimic processes that ultimately lead to human disease [6]. Small-animal research is now frequently used to improve our understanding

---

<sup>2</sup> A phantom is an inanimate object that acts as a radioactive source distribution for the camera in place of a live subject.

of human disease, develop means to combat these diseases and then translate these into clinical treatments [7].

Many dedicated small-animal SPECT cameras have been developed with the necessary improvements in spatial resolution to image the smaller organs of rats, mice and other laboratory animals. The key advantage that SPECT offers to small animal research is that it permits *in vivo* analysis of disease progression, where quantitative analysis can be performed without sacrificing the animal. This reduces the cost of research on small animals, allows longitudinal research—where the same subject can be followed and studied over a long period of time—and opens the possibility for many new studies that would not be possible without an *in vivo* imaging technology [6].

## 1.2 Tracers in Nuclear Medicine

In SPECT, the origin of the signal comes from the tracer; a tracer is a radioactive isotope bound to a biological molecule in order to track the distribution of the molecule under study. A list of common radio-isotopes used in SPECT with their properties is outlined in Table 1-1.

Table 1-1: Common radio-isotopes used in SPECT [8]

Radio-isotope	Half life	Decay Mode	Primary Emission Energy (keV)
Tc-99m	6.0h	Isomeric Transition	140.5
In-111	2.8d	Electron Capture	171.3, 245.4
I-123	13.2h	Electron Capture	159
Tl-201	73h	Electron Capture	X-rays (69-83), 135, 167

Tc-99m is by far the most common isotope used in SPECT. Different Tc-99m-labeled tracers have been developed to image a wide variety of biological functions. At the University of Ottawa’s Heart Institute (UOHI) Tc-99m is commonly bound to a

tetrofosmin molecule and used clinically to image blood flow (perfusion) in the heart. By comparison of reconstructed rest and stress Tc-99m-tetrofosmin SPECT images of the heart, a cardiologist can determine areas of heart muscle tissue (myocardium) that lack blood and hence oxygen supply (ischaemia) in patients with suspected coronary artery disease (CAD) [9]. If the oxygen supply gets too low, then the heart tissue will die (infarct). Similar studies can be done using a rat model of CAD, providing quantitative measurements of myocardial infarct [10].

## 1.3 Photon Interactions with Matter

As we have all seen first-hand from a young age, visible light ( $E \approx 1 - 3\text{eV}$ ) will readily be reflected, refracted and absorbed by many materials. Compared to visible light, gamma radiation is more energetic by 5 orders of magnitude. Gamma photons are much more penetrating, and due to their low wavelengths, cannot be refracted like low energy visible light. The three major mechanisms by which gamma rays in medical physics interact and transfer energy to matter are the photoelectric effect, Compton scattering, and pair production [11].

### 1.3.1 Photoelectric Effect

The photoelectric effect occurs when an incident photon is totally absorbed by a target atom. To conserve energy, the atom ejects an electron with kinetic energy given by equation 1-1:

$$E_{electron} = E_{0,photon} - BE. \quad 1-1$$

$E_{\text{electron}}$  is the kinetic energy of the ejected electron,  $E_{0, \text{photon}}$  is the initial energy of the photon, and BE is the binding energy of the ejected electron. If the incident photon has less energy than the binding energy of the least energetic electron, the photoelectric effect is impossible.

An incident photon is more likely to interact with electrons with binding energies close to the photon energy. Thus, if the photon has sufficient energy, it will be more likely to interact with the most tightly bound electrons in an atom. When the photon energy is sufficient to eject an inner-shell electron, this leaves a vacancy in the atom. As a result, an outer-shell electron will drop its energy level to take its place. The difference in energy of the two shells is emitted as a characteristic x-ray, unique to the atom where the absorption occurs. This interaction mechanism is most probable when low-energy gamma rays interact with materials of high atomic numbers.

### 1.3.2 Compton Scatter

In contrast to the photoelectric effect, which is more likely to involve the most tightly bound electrons, Compton scatter is a mechanism that tends to involve the most loosely bound electrons of an atom. As shown in Figure 1-1, in this type of interaction, the photon deflects off of a loosely-bound electron. After the collision, the photon's direction and energy decrease according to the laws of energy and momentum conservation. An atomic electron absorbs the lost energy and is ejected from the atom.

Applying conservation of energy and momentum, one can show that the energy of the scattered photon  $E_f$  is a function of the initial photon energy  $E_0$ , the rest mass of an electron  $m_0c^2$ , and the scattering angle of the photon  $\theta$  in equation 1-2:

$$E_f = \frac{E_0}{1 + \frac{E_0}{m_0 c^2} (1 - \cos \theta)} \quad 1-2$$

One can also show that it is impossible for a photon to transfer all of its energy to the electron via Compton scattering using energy and momentum conservation. This means that this process begins with one unbound energetic particle and results in two unbound energetic particles, even in the limiting cases.

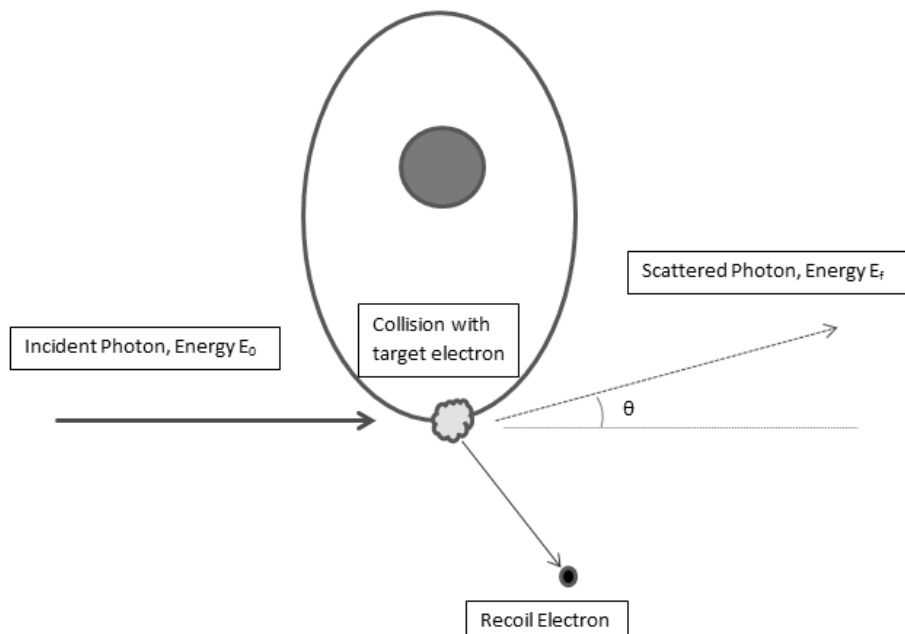


Figure 1-1: Depiction of Compton Scatter. An incident photon scatters off of a loosely-bound electron and ends up with direction  $\theta$ , donating energy to the electron.

### 1.3.3 Pair Production

Pair production is the production of an electron-positron pair, resulting from the interaction between the photon and the electric field of the nucleus [12]. Since the rest mass of the electron-positron pair is 1.022MeV, this is the minimum photon energy required for pair production to occur. Most SPECT isotopes do not emit photons at this

energy, and therefore pair production is not possible. Any additional energy that the incident photon had before interacting with the electric field is conserved in the form of kinetic energy of the newly-formed charged particles. Unlike in Compton scattering, the photon ceases to exist after donating its energy to the electron-positron pair.

## **1.4 The Gamma Camera**

The ultimate goal of SPECT is to produce a 3-D image of the distribution of a radioactive tracer inside the subject based on the signal detected outside of the subject. Hal Anger developed the Gamma Camera (also called the Anger Camera) in 1958 to image Gamma emissions [13]. The general design is still commonly used for nuclear imaging today. It consists of a collimator, scintillation crystal, an array of photomultiplier tubes (PMTs), radiation shielding, and energy discriminating and positioning electronics [13].

### 1.4.1 Collimator

The collimator is the first part of the gamma camera that the photon emitted from the isotope encounters. It is designed to select photons traveling in a specific direction by absorbing photons that do not move along the required path. This absorptive collimation is the limiting factor in terms of sensitivity of the system. Without the directionality provided by the collimator, producing a 3-D image based on separate projections would be much more difficult. A common type of collimator is the parallel-hole collimator, illustrated in Figure 1-2.

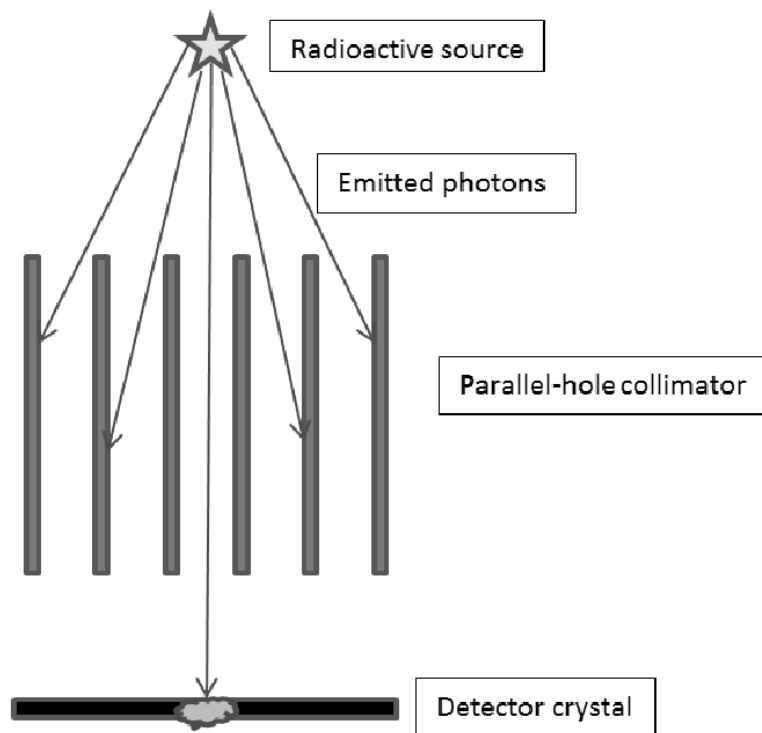


Figure 1-2: A 2-D schematic of the principal function of the parallel-hole collimator. It is designed to accept photons (arrows) traveling perpendicular to the detector-crystal surface by absorbing photons that do not have this desired direction.

Only photons (arrows) travelling perpendicular (within a small acceptance angle) to the detector surface will make it through the holes in the collimator, and interact with the detector crystal. Any photons striking the collimator at angles greater than the acceptance angle are absorbed. As gamma rays travel in straight lines, knowing the direction that the ray is travelling in tells us the direction of a vector drawn from the position of the detection event to the position of the origin of the radioactive decay, though it does not tell us the distance to the origin of the decay.

There is some error in the assumption that all photons that make it through the parallel-hole collimator will be travelling in a direction perpendicular to the detector. Based on the width of the apertures, photons travelling at small angles to the perpendicular will be accepted. Narrowing the apertures improves the spatial resolution (due to smaller acceptance angles), but simultaneously lowers the sensitivity of the system. The collimator's septa are made up of heavy elements, which have high stopping powers. Lead ( $Z = 82$ ) is the most common material used, due to its high stopping power and relatively low cost [13]. Even with the use of heavy elements in the septa, there is still the possibility of septal penetration, especially when imaging with higher-energy photons. This further degrades the image resolution.

Depending on the situation, one might require high resolution without worrying too much about the sensitivity, or vice versa. The different isotopes used in SPECT also emit radiation with different energies. Collimators are, therefore, classified according to the energy of the isotopes to be imaged and the desired sensitivity. Four types of parallel-hole collimators that are routinely used clinically are: LEHR (low-energy, high-

resolution), LEAP (low-energy, all purpose), MEAP (medium-energy, all-purpose), and HEAP (high-energy, all-purpose) [13].

Other collimator geometries are also possible, and one of the geometries gaining in popularity is the pinhole geometry. As the name suggests, these collimators use one or more pinholes to focus different versions of the same image onto the detectors. This geometry is becoming prevalent clinically in cardiac SPECT [14], and in small animal imaging [15, 16], due to the magnifying effects of pinholes that lead to significant resolution improvement. In small-animal pinhole imaging, it is possible to obtain resolution below 0.5mm [17]. A disadvantage of this collimator is that using a single pinhole results in very low sensitivity since only photons travelling through the pinhole will reach the detector [17]. To combat this, sensitivity can be increased by focusing separate images through multiple pinholes.

Assuming no septal penetration, the position-dependent sensitivity of pinhole SPECT can be described as equation 1-3:

$$g = \frac{d^2 \sin^3 \theta}{16h^2}. \quad 1-3$$

Here,  $g$  is the sensitivity,  $d$  is the geometric diameter of the aperture,  $\theta$  is the angle of incidence and  $h$  is the perpendicular distance from the aperture to the source [18].

The resolution of the image produced at the detector, defined as the full-width at half-maximum of the point-spread function, can be given as equation 1-4:

$$FWHM = d \left( 1 + \frac{1}{M} \right). \quad 1-4$$

In this equation,  $d$  is the pinhole diameter, and  $M$  is the magnification of the pinhole. The magnification depends on the spatial position of the source ( $h$ ) compared to the focal length of the pinhole ( $f$ ), and will be highest when the source-to-pinhole distance is minimal.

When accounting for septal penetration, one normally replaces the pinhole diameter  $d$ , with an effective diameter  $d_e$  [18]. The effective diameter can be described as equation 1-5 [19, 20]:

$$d_e = \sqrt{d(d + \frac{2}{\mu} \tan^2 \frac{\alpha}{2}) + \frac{2}{\mu^2} \tan^2 \frac{\alpha}{2}}. \quad 1-5$$

In this equation,  $d$  is the pinhole diameter,  $\mu$  is the linear attenuation coefficient of the collimator material, and  $\alpha$  is the acceptance angle of the pinhole. The geometry of the pinhole collimator is displayed in Figure 1-3.

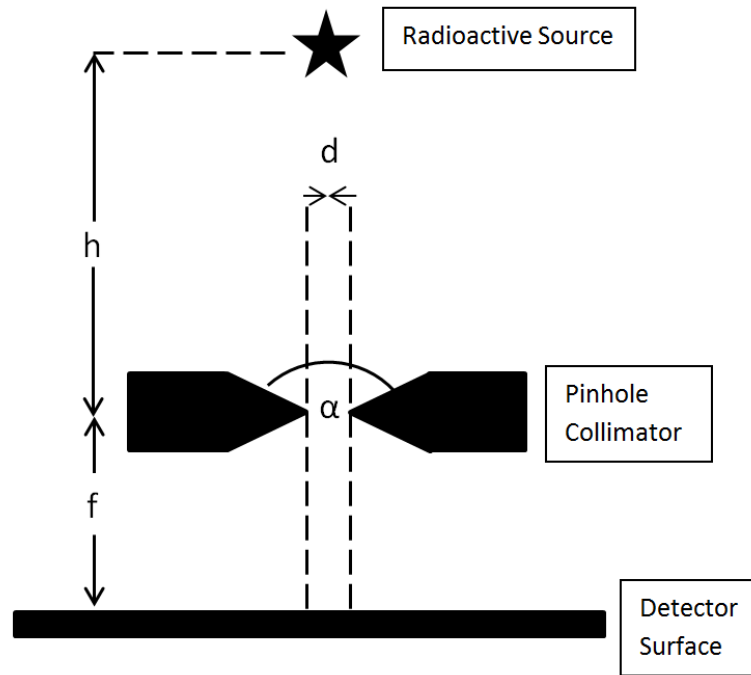


Figure 1-3: Configuration of a single-pinhole collimator. In this diagram, the star represents a radioactive source,  $h$  is the pinhole-to-source distance,  $f$  is the focal length of the pinhole,  $d$  is the width of the pinhole, and  $\alpha$  is the acceptance angle of the pinhole.

#### 1.4.2 Scintillation Detectors

Assuming the collimator is working properly, the relatively small number of photons that pass through will have the desired directionality to produce a projection image onto the underlying detector crystal. The function of the scintillation crystal is to absorb the gamma photon through photoelectric and Compton (section 1.3.2) interactions [21], and convert the high energy photon into multiple visible and ultraviolet (UV) photons. The energy of the incident photon can be determined based on the light output of the scintillation crystal [13]. There is a tradeoff with sensitivity and resolution of the scintillation crystal. Increasing the thickness of the crystal will stop more gamma rays, improving sensitivity, but degrades resolution based on the larger distance between the location of the scintillation event and the next stage of detection: the PMTs.

### 1.4.3 Photomultiplier Tubes

For each gamma-ray-detection, PMTs take the multiple UV or visible-light photons produced by the scintillation crystal as the input and convert them into multiple photo-electrons. As shown in Figure 1-4, PMTs consist of a photocathode, anode and multiple dynodes. The photocathode absorbs the incident photons from the scintillation crystal, and converts them into photoelectrons via the photoelectric effect (described in section 1.3.1). The conversion rate is typically on the order of 20-25% [13]. The electron then interacts with the dynodes, which amplify them into more electrons, increasing the signal intensity by a factor of 3 to 6 per dynode. There is a high voltage difference between each dynode that is used to accelerate the electrons along the path. The resulting current, which has been amplified by 7-8 orders of magnitude, [11] is collected at the anode.

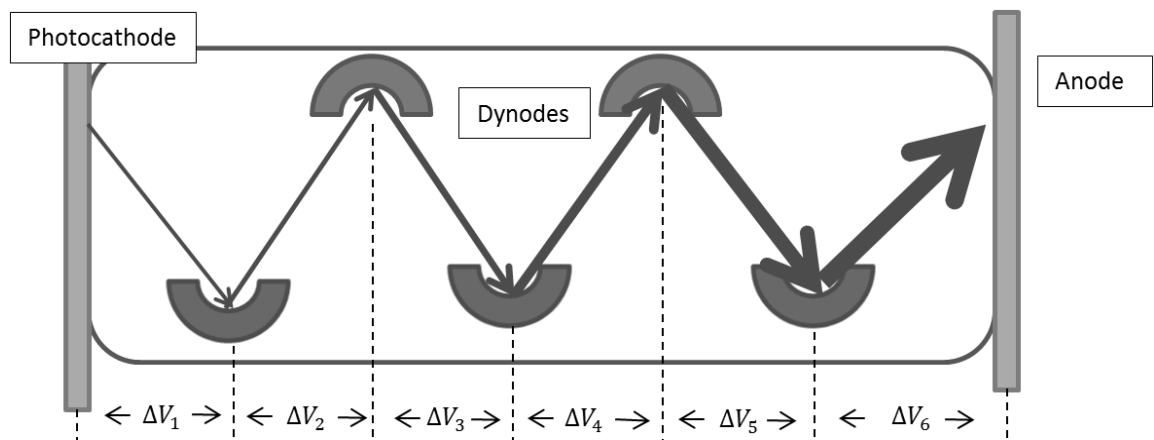


Figure 1-4: The charge amplification process accomplished by a PMT with 5 dynodes. Light photons interact at the photocathode to produce electrons via the photoelectric effect. The arrows represent the electron paths, and the number of electrons increases after interacting with each dynode. The electrons are accelerated by a high potential difference,  $\Delta V_i$ , across each dynode.

#### 1.4.4 Event Positioning/Energy Information

The flash of visible or UV light produced by the scintillation crystals after stopping a gamma ray generates a current at the anode of many PMTs (for example, 1 detector head on the Bioscan NanoSPECT/CT preclinical system contains 33 PMTs), due to the spread of the flash. To determine the 2-D location of the event along the surface of the detector, it is assumed that the amplitude of the signal at each anode is inversely proportional to the distance from the scintillation event.

Positioning and pulse/energy discrimination were originally done with clever analog circuitry, calculating weighted sums of the PMT output signals to produce (x,y) coordinates as well as energy information of each event [13]. At present, the positional and energy information from the PMTs are digitized and maximum likelihood positioning algorithms are generally used to determine the locations and energies of events [13, 22]. The digitization of the signal allows for more knowledge of the system to be incorporated into the event localization and energy estimation, such as the use of calibration data and linearity/uniformity corrections [13]. To organize the set of detected events, the crystal surface is divided into a 2-D array of elements called pixels. After the pixel corresponding to the detection is determined, it is incremented by 1 count in the image corresponding to the energy of the photon.

The accuracy with which an event is positioned on the crystal is referred to as the intrinsic resolution. It depends on errors caused by the depth of interaction of the gamma rays within the crystal, as well as PMT array and positioning electronics. Combining the intrinsic resolution  $R_i$  with the pinhole resolution (equation 1-4) in quadrature gives the net resolution of the projected image [23], given in equation 1-6:

$$R_{net} = \sqrt{\left(d_e + \frac{d_e}{M}\right)^2 + \frac{R_i^2}{M^2}}$$

## 1.5 Energy Windowing

As the energy of each detected gamma-ray is measured, the detected events can also be sorted based on gamma-ray energy. This process, called windowing, has become standard practice in clinical and pre-clinical SPECT. Many systems also allow acquisition in *list mode*, where the specific energy, location of detection, time of detection, and other information is recorded individually for each detected event. With list mode, projections can be sorted after the acquisition based on the photon energy and the time detected during the scan. List mode provides incredible flexibility to the user, but such a high amount of information requires a great deal of computer memory and so is not available on many SPECT systems.

A typical energy window used for Tc-99m SPECT imaging with NaI(Tl) detectors has a 20% width centered at the emission energy of Tc-99m [126keV, 154keV]. This type of window is called the photo-peak window. Using a window to discard counts outside of this range is important mainly to reduce the detection of photons that have scattered prior to detection, which would degrade the resolution of the image. It will also reduce the detection of background counts, since only background within the energy window will be accepted. Windowing, however, is not sufficient in eliminating problems associated with Compton scatter, the process described in section 1.3.2. Other windows can be used to capture different parts of the spectrum to approximate scatter. This

problem and solutions in relation to single isotope and dual isotope SPECT are discussed further in section 1.9.

## 1.6 Dual-Isotope SPECT

The ability to sort out the projections into separate images based on the energy of the detected photons naturally offers the possibility of dual-isotope imaging in SPECT. Shown in Figure 1-5, isotope A and isotope B are differentiated by accepting counts in the left window as A and the right window as B. In the absence of scatter the detected signals are accurately represented as Gaussian functions centered at the emission energy and FWHM representing the energy resolution of the detection system.

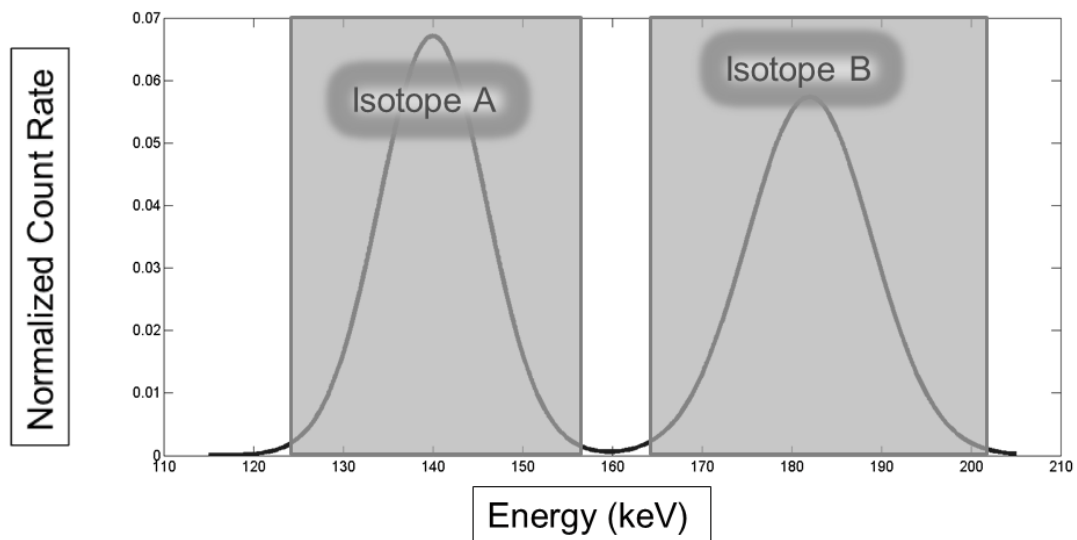


Figure 1-5: “Energy-windowing” to produce separate projections for hypothetical isotopes A and B. In the absence of scatter, the activity distributions of A and B can be accurately quantified by separately reconstructing the projections in window A and window B.

The observed spectrum from a single isotope follows the normal distribution because the detection of a single event represents the sum of a large number of light photons (produced at the scintillation crystal), converted into a sum of many electrons (produced by the PMTs). There is a random uncertainty associated with these and other processes at each stage of the detection chain [24]. According to the central limit theorem, the sum of a large number of randomly distributed variables will be normally distributed about the mean of the random values.

## **1.7 Image Reconstruction**

After acquiring a set of 2-D projections from different angles, an image reconstruction technique is used to produce a 3-D distribution of activity. Traditionally, this was done using an analytic method called Filtered Back-Projection (FBP). In modern SPECT reconstruction, however, iterative techniques are most common because they allow correction for important physical processes, such as scatter and attenuation.

### **1.7.1 Filtered Back-Projection**

The mathematical theory for FBP was introduced by Johann Radon in the early 20<sup>th</sup> century [25], before the application to medical physics was apparent. The general idea is that if collimated (for example, using parallel-hole collimation) projection profiles are obtained at various angles around an object emitting radiation, the counts recorded at a given detector pixel, at a particular angle, represent the value of the line integral through the activity distribution in the object [13]. Back-projecting this value (shown in Figure 1-6, centre) means distributing the projection element's value evenly between

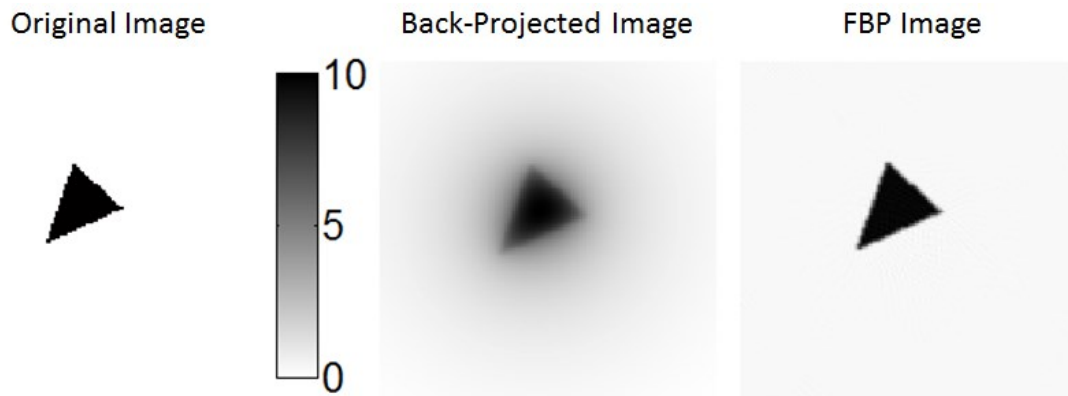


Figure 1-6 Left: The true source distribution. Centre: Back-projection, 128 projections. Right: FBP, 128 projections. There is a noticeable blur in the back-projected image due to variation in sampling frequency caused by the rotating acquisition geometry. Using a ramp-filter (FBP) removes this blur.

each voxel along the line it came from [13]. This is done for all projections acquired from all angles, and the summed result is a blurry version of the true image [13].

The main component of the blur in the back-projected image is a result of the variation in sampling density caused by the rotating acquisition geometry. Compensation for this blurring requires filtering the image with a ramp filter which is a linear function when applied in the Fourier domain [13]. The principle goal of this filter is to balance the sampling density by suppressing low spatial frequencies and enhancing high spatial frequencies. This combination of back-projecting and filtering is called filtered-back-projection. The filtered-back-projected image of a small source is shown on the right of Figure 1-6. The main advantage of FBP is that it is an analytic solution to the problem and therefore is computationally cheap [26]. The problem with FBP is that it is impossible to model attenuation and scatter within the algorithm [13]. It therefore cannot give accurate quantitative results in any activity distributions.

### 1.7.2 Iterative Methods

Iterative reconstruction algorithms use the concepts of projection and back-projection, but do not assume that the back-projection operation of the original projections gives the true activity distribution. Iterative algorithms begin with an initial guess of the activity distribution (for example, a uniform activity distribution in the FOV), and then simulates the projections that would be produced if a SPECT acquisition was performed on the image. The projections are compared to the true measured projections and used to update the estimated activity distribution. This process continues until convergence is reached.

A popular iterative reconstruction algorithm is the Maximum Likelihood Expectation Maximization (MLEM) method, described in equation 1-7:

$$a_i^{n+1} = \frac{a_i^n}{\sum_j \tilde{M}_{ji}} \sum_j \frac{\tilde{M}_{ji} p_j}{\sum_i \tilde{M}_{ji} a_i^n} \quad 1-7$$

In this equation,  $a_i^n$  is the current image estimate at voxel  $i$  after iteration  $n$ ,  $a_i^{n+1}$  is the next image estimate,  $p_j$  is the *actual* number of counts detected at projection pixel  $j$ , and  $\tilde{M}_{ji}$  is the probability of detecting a photon from image voxel  $i$  at projection element  $j$ .

The factor  $\frac{1}{\sum_j \tilde{M}_{ji}}$  is the normalization factor, which corrects for the weighting of the number of voxels that contribute to each pixel such that when the forward projection matches the measured projection, the voxel values  $a_i$  do not change. This approach to reconstruction allows accurate correction for attenuation (and scatter), modeling the

effects in the forward projection estimate. This method also permits the inclusion of noise in the reconstruction, which FBP does not incorporate [13, 26].

## 1.8 Photon Attenuation Correction

A gamma ray emitted by a radiotracer inside the subject has a finite probability of interacting with the subject tissues before making it to the detector. Assuming narrow beam geometry (meaning that photons will not scatter from outside the path into the FOV of the detector), a photon beam of initial intensity  $I_0 [s^{-1}m^{-2}]$  will end up with intensity  $I(x)$  after passing through an absorber of linear attenuation coefficient  $\mu_l$ , described in equation 1-8.

$$I(x) = I_0 e^{-\mu_l x} \quad 1-8$$

Here,  $\mu_l$  is a constant that depends on the density and chemical composition of the absorber. To remove the dependence on density, the attenuation coefficient is more commonly expressed in tables as a mass attenuation coefficient  $\mu_m = \frac{\mu_l}{\rho}$ . The mass attenuation coefficient  $\mu_m$  is often described as a cross section, since the units are  $[\frac{m^2}{g}]$ .

The attenuation cross section can be broken down into cross sections for specific types of interactions. As described in section 1.3, the most important interactions of photons with matter in SPECT are the photoelectric effect and Compton scatter. Thus,  $\mu_m$  can be expressed as equation 1-9, where  $\tau$  is the photoelectric cross section and  $\sigma$  is the Compton cross section [12].

$$\mu_m = \tau + \sigma \quad 1-9$$

If the attenuating material is not homogeneous, then a narrow beam emitted at coordinate  $r_i$  in the direction  $\theta$  and detected at  $r_f$  will have a relative transmitted intensity described by equation 1-10:

$$\frac{I}{I_0} = \exp\left(-\int_{r_i}^{r_f} \mu_l(r, \theta) dr\right). \quad 1-10$$

At each infinitesimal point along the line from  $r_i$  to  $r_f$ , the beam will be travelling through a material with a linear attenuation coefficient specific to the location along the path. Therefore, the resulting attenuation coefficients along the path can be described by the line integral  $\int_{r_i}^{r_f} \mu_l(r, \theta) dr$ .

As a result, if no correction for attenuation is made, the reconstructed image will contain inaccuracies based on the amount of attenuating media present during the acquisition. For example, if a source of activity is diluted and thoroughly mixed with water in a spherical container, there will be a significant underestimation of activity at the center of the sphere, while smaller underestimations will be present at the edges. Due to smaller subject sizes, this is less of a problem when imaging small animals compared to humans, but is still important for accurate quantification. For example, mouse sized Monte-Carlo simulations determined that attenuation effects cause quantification errors of up to -18% for Tc-99m or In-111 and -41% for I125 [27].

To correct for photon attenuation, many modern SPECT cameras are equipped with built in Computed Tomography (CT) cameras. Since CT generates a 3-D image of

the anatomical structure of the subject based on the differential attenuation of an external x-ray source, a map of attenuation coefficients  $\mu_l(x, y, z)$  can be generated.

The most common approach for converting CT values to attenuation coefficients for photons of a specific energy involves a bi-linear piecewise relationship as described in [13, 28] and has been used to convert CT values to 140keV Tc-99m attenuation coefficients [29]. The resulting map of attenuation coefficients is used to adjust the probability matrix  $\tilde{M}_{ji}$ , described in section 1.7.2 and used in the iterative reconstruction of SPECT projections to simulate the attenuation that occurs between the points of emission and detection.

Strydhorst and Wells [30] evaluated the effects of attenuation in a small animal nanoSPECT/CT system [31] using phantom studies of small cylinders with known Tc-99m activity concentrations set inside concentric cylinders filled with water. The Tc-99m activity concentration was underestimated by 8% in a 9mm diameter cylinder and by 30% in the 52mm diameter cylinder. Applying CT-based attenuation correction as described above resulted in an overestimation of activity concentration by < 1% for the 9mm phantom and overestimation by 5% in the 52mm phantom. *In vivo*, using Tc-99m-tetrofosmin (uptakes in the rat myocardium), uptake was overestimated by  $5 \pm 3\%$  compared to well counter measurements if only attenuation correction was applied.

Wu et al. [32] used a U-SPECT-II multi-pinhole small-animal SPECT system and a 45mm diameter cylinder phantom of known Tc-99m activity concentration to determine the accuracy of absolute activity quantification of the system. Without attenuation or scatter correction, the Tc-99m activity concentration in the phantom was underestimated

by 18.7%. After applying a first order post-reconstruction attenuation correction method developed by Chang [33], the activity concentration in the phantom was overestimated by 9.2%.

## 1.9 Scatter Compensation Methods

The overestimations of activity after applying only correction for attenuation in the studies mentioned in section 1.8 are not likely the result of shortfalls in the attenuation correction procedures; the overestimations result from photons that scatter within the phantom and are still detected within the energy window set for Tc-99m. Using a standard photo-peak window, a Tc-99m photon that would have otherwise been detected at 140keV could scatter up to  $53^\circ$  and still be detected within the energy window. Because narrow-beam attenuation coefficients were used (assuming that scattered photons would not be detected), the detection of singly, doubly, or multiply scattered photons cause the activity over-estimation. For a given SPECT system, the amount of scatter detected depends on the geometry and composition of the source within the FOV.

When imaging with more than one isotope, correction for scatter is more complicated due to the presence of self-scatter as well as cross-talk. Cross-talk is a special type of scatter unique to multi-isotope SPECT. It occurs when photons of the higher-energy-emitting tracer scatter in the subject and are detected within the energy window designated for the lower-energy-isotope. While standard corrections for self-scatter would work for the higher-energy-isotope, the lower-energy-isotope requires special correction for cross-talk.

Cross-talk for Tc-99m & In-111 dual isotope SPECT is illustrated in the form of an energy spectrum in Figure 1-7. In this spectrum, Tc-99m activity would be overestimated by approximately 25% due to a combination of self-scatter and cross-talk. The amount of cross-talk is proportional to the activity concentration of In-111.

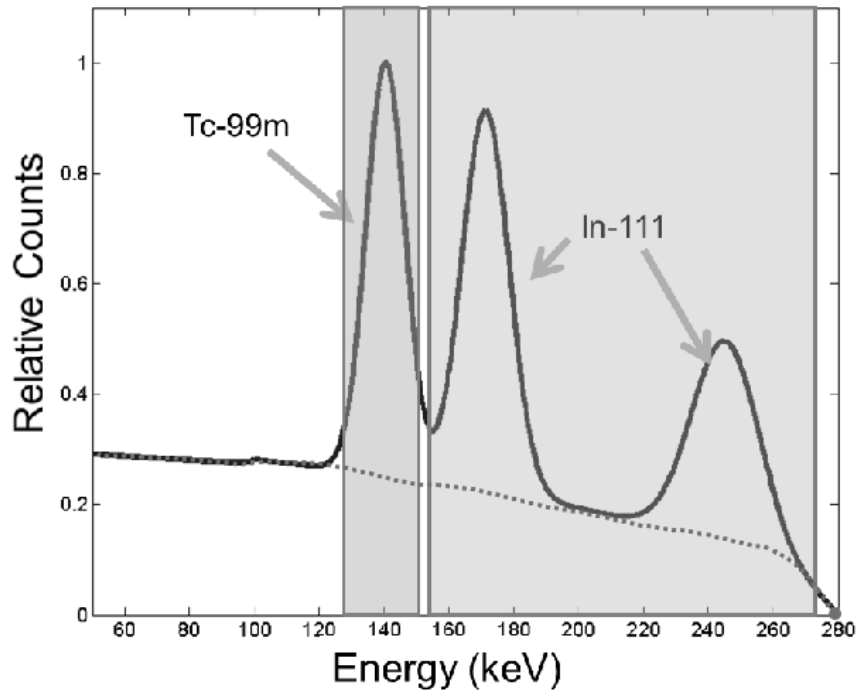


Figure 1-7: Schematic of an energy spectrum resulting from a dual isotope acquisition of Tc99m (140keV emission) & In111 (171 and 245keV) is the solid black line. The resulting Tc99m activity is overestimated due to a combination of self-scatter, as well as cross-talk caused by In111 scatter into the Tc99m window. Scatter is shown as the dotted line.

Some corrections for self-scatter can be modified to account for the combination of self-scatter and cross-talk. The following subsections discuss some common approaches to scatter correction, with the emphasis on correction for the combination of self-scatter and cross-talk when applicable. These include methods that use broad-beam—in contrast to narrow-beam—attenuation coefficients in the attenuation map,

Triple Energy Window (TEW) method, Dual Energy Window (DEW) method, convolution methods, analytic methods, and Monte-Carlo-based methods. Some thorough reviews of scatter correction in SPECT are available which go into more detail than this paper [21, 34, 35].

### 1.9.1 Adjusting the Attenuation Map

This method assumes that scatter causes an overestimation in images corrected for attenuation because narrow-beam geometry is assumed to correct for attenuation. In essence, this is a valid assumption to make: the scatter that is detected is the result of photons that have scattered *into* the detector. Attenuation correction using the narrow-beam assumption assumes that scattered photons are never detected. Broad beam effective attenuation coefficients can be used instead, which attempt to account for the presence of scatter into the detector. Therefore, the effective attenuation coefficient for broad-beam geometries is significantly lower than for narrow-beam geometries.

This approach works well for objects of uniform activity distributions in a uniform attenuating medium [11, 30]. In more complex situations, however, it does not properly take the spatial distribution of scatter into account, as it only corrects for the bias in the attenuation correction. Therefore, it fails in most applied situations [11].

### 1.9.2 DEW

The DEW, developed by Jaszczak et al [36] requires the acquisition of counts in an extra energy window below the photo-peak, called a scatter window. It is a pixel-by-pixel subtraction that can be done as a pre-correction on the projections or

implemented at the forward-projection step within the iterative reconstruction algorithm. It assumes that, for all points in space, the scatter detected inside the scatter window is proportional to the amount of scatter detected within the photo-peak. The straightforward computation is what makes this method popular for scatter correction in single-isotope studies.

The disadvantages of this approximation are that the computation relies on the constant of proportionality between the scatter in the scatter window and the scatter in the photo-peak window. This can change with geometry and composition of the subject. Also, this method assumes that the scatter profile in the scatter window has the same spatial distribution as in the photo-peak window. This is not ideal, since photons detected in the scatter window will have scattered by larger angles and/or have experienced more scatter events than the scattered photons in the photo-peak window.

The DEW would not be a helpful tool for correction of cross-talk, since the constant of proportionality between counts in the low scatter window and the photo-peak changes in the presence of an extra emitter at higher energies.

### 1.9.3 TEW

The TEW was developed by Ogawa [37]. This method uses counts recorded in two scatter windows on either side of the photo-peak in order to estimate scatter. The scatter profile in the photo-peak window is approximated using linear interpolation between the counts recorded in the two scatter windows, shown in equation 1-11:

$$Scatter = \frac{w_p}{2} \left( \frac{C_{high}}{w_{high}} + \frac{C_{low}}{w_{low}} \right). \quad 1-11$$

Here,  $w_p$  is the width of the photo-peak window,  $C_{high}$  and  $w_{high}$  are the number of counts recorded in the high scatter window and the width of the high scatter window, respectively, and  $C_{low}$  and  $w_{low}$  are the number of counts recorded in the low scatter window and the width of the low scatter window, respectively.

Unlike DEW, the TEW method does not rely on a constant of proportionality  $k$ . Therefore, it can be used to correct for the combination of self-scatter and cross-talk. This was noted by the same group who introduced the TEW two years after the TEW method was published, and tested using a mixed phantom of Tl201 & I123 [38]. If only 1 isotope is used, TEW is still effective in subtracting self-scatter, since the high scatter window will contain an empty image. The positioning of the scatter windows for dual-isotope Tc-99m and In-111 imaging is shown in Figure 1-8.

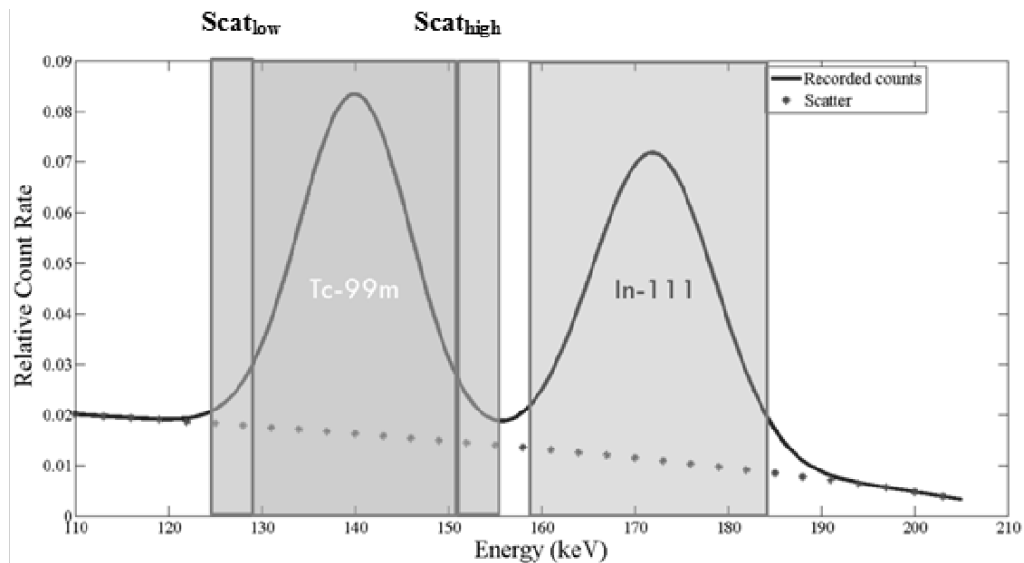


Figure 1-8: Simplified version of a Tc99m & In111 spectrum. The total counts are the solid black line, and the dotted curve is the contribution of scatter to the detected counts. The narrow windows surrounding the Tc-99m window ( $Scat_{low}$  and  $Scat_{high}$ ) are the TEW scatter windows. In this setup, scatter is over-estimated due to the presence of un-scattered photons in the scatter windows.

In contrast to DEW, the scatter windows used are narrow, and situated close to the photo-peak. This gives less of a discrepancy in the spatial distributions of the counts recorded in the scatter windows compared to the true scatter contribution to the photo-peak image. The downfall of this technique comes with the noise inherent with low-counting statistics in the narrow energy windows. Because of the low count rates in the Tc-99m window and adjacent scatter windows, the noise can cause many negative projection elements in the scatter corrected images due to over-subtraction in regions of mostly In-111. To compensate for this, filtering can be used. It must be applied to the scatter estimate with the goal of decreasing noise amplification while at the same time minimizing the introduction of bias [39]. The filtering has been applied separately on the sets of projections [40, 41] or on the TEW scatter estimate itself [39, 42].

Energy-window-based scatter correction methods are probably the most popular scatter correction methods, with many users clinically and in small animal SPECT. Their popularity is due to the speed, ease of implementation, and accuracy in correction for self-scatter, as well as for cross-talk with many combinations of isotopes.

#### **1.9.4 Modified TEW**

The TEW assumes that scatter windows contain purely scatter. For single-isotope imaging, it is usually possible to position the windows such that this is the case. However, depending on the emission energies of the isotopes used in multi-isotope imaging, this is not always possible.

For example, in dual-isotope imaging with Tc-99m and In-111, the proximity of the 171keV In-111 primary emission to the 140keV Tc-99m emission creates problems

for the TEW. The Gaussian distribution representing the detection of the un-scattered In-111 emission overlaps with the high scatter window used for the Tc-99m TEW scatter estimate. In order to lessen this overlap, Timmins narrowed the Tc-99m photo-peak window from 20% (standard for Tc-99m) to 15%. Scatter windows with 5% widths were used on either side of the photo-peak window [43]. This is similar to those optimized by Zhu [44]. Although this reduced the inclusion of un-scattered In-111 photons in the high scatter window, the proximity of this scatter window to the 140keV Tc-99m emission resulted in an overlap of the Tc-99m primary emission with the high scatter window. Due to the energy resolution of the system and the emission energies of the isotopes used, the inclusion of un-scattered photons in the high scatter window is unavoidable. This problem is outlined in Figure 1-9.

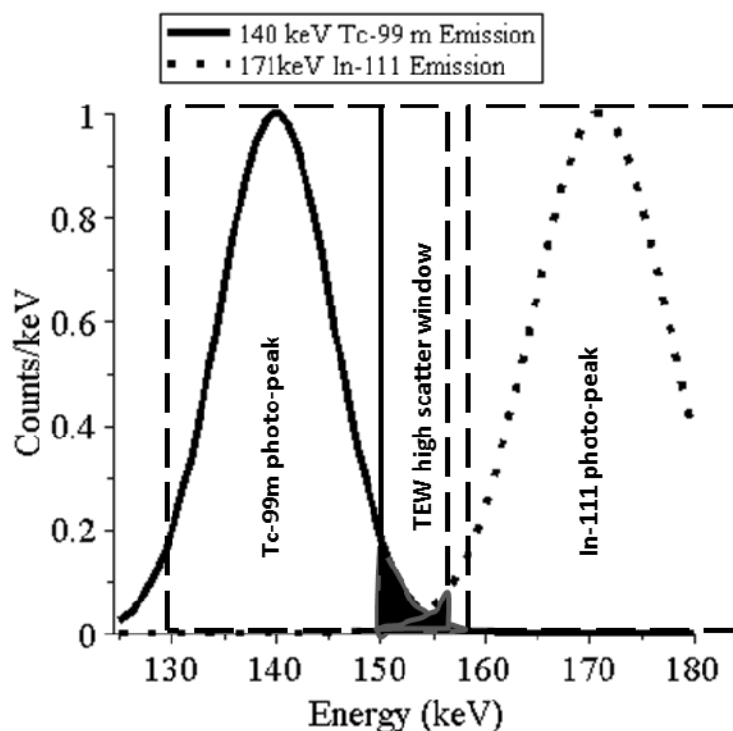


Figure 1-9: Depiction of the overlap of Tc-99m and In-111 un-scattered photons into the TEW high scatter window due to the proximity of the photo-peaks of the respective isotopes. The shaded regions represent the parts of the un-scattered photon energy distribution that are incorrectly assumed to be scattered photons.

The limited accuracy in the standard TEW becomes apparent with this setup when computing the integral of the Gaussian function describing the energy resolution of the system in response to Tc-99m and In-111 photons. In the setup described above, 3% of all un-scattered Tc-99m photons and 2% of 171keV In-111 photons are detected in the high TEW scatter window.

Timmins provided a modification to the TEW to compensate for the presence of un-scattered photons detected in the scatter energy-windows, by estimating and subtracting the primary components of In-111 and Tc-99m emissions from each scatter window before applying the TEW. The primary component of an emission to a particular

scatter window was assumed to be proportional to the counts recorded in the photo-peak window, assuming that the photo-peak contained no scattered photons.

With this modification in place, Tc-99m activity was accurately quantified within 5% in five phantoms containing mixtures of In-111: Tc-99m activity ratios between 4.5:1 and 1:8. In phantoms containing only In-111, however, the residual scatter in the Tc-99m images was greater than 10% of that before corrections were applied [43]. This overestimation in phantoms of mostly In-111 is likely caused by the fact that the modified TEW incorrectly assumes that there is no scatter present in the Tc-99m photo-peak when estimating the contribution of un-scattered photons to the scatter windows. Therefore, in regions of mostly In-111, the modified TEW subtracts too many counts from the scatter windows, resulting in an under-estimation of scatter.

### **1.9.5 Convolution Methods**

Convolution methods attempt to model the distribution of scattered photons without taking photon energy into consideration. The estimated distribution of scattered photons within a given photo-peak is based on the assumption that the scattered image can be represented as a convolution of the photo-peak image with an appropriate blurring kernel. Parameters of this blurring kernel can be determined experimentally or through Monte-Carlo simulations [21]. This method can be modified to facilitate correction for cross-talk [45] as well as self-scatter, using unique blurring kernels applied to both photo-peaks. The disadvantage of this approach is that it assumes a spatially invariant scatter distribution, which is not the case in most scenarios.

### 1.9.6 Analytic Models

Methods have been developed to analytically determine the probability distributions of un-scattered, Rayleigh-scattered, and Compton Scattered photons [46]. Some have been developed to correct for cross-talk for Tc-99m and I-123 SPECT [47] as well as Tc-99m and In-111 SPECT [48]. These types of models tend to be accurate but very computationally demanding because modelling first, second, and multiple order scatter events requires the evaluation of high order integrals. A further disadvantage of both analytic as well as other modelling approaches is that they are unable to account for out-of-FOV scatter sources.

### 1.9.7 Monte-Carlo (MC) Methods

Knowing the distribution of attenuation coefficients in the FOV, one can potentially use Monte-Carlo to simulate the full scatter distribution by modelling transport of a large number of photon paths. This has been used to model self-scatter as well as cross-talk [49] and has been shown to be superior in accuracy compared to the TEW [50]. It is often used along with experiment to validate other methods of scatter and attenuation correction. The main disadvantage of a fully simulated Monte-Carlo model is the amount of computation power and time required to simulate such a model. Studies have found that Monte-Carlo-based scatter compensation is more accurate than TEW, but the improvement in scatter estimation may not justify the larger computational requirements [50]

In order to take advantage of the power of Monte-Carlo, but reduce the computation time required, accelerated Monte-Carlo techniques have been developed. A

common method of speeding up the Monte-Carlo algorithm is called forced detection. In standard forced detection, photons at each Monte-Carlo-determined scatter point are forced towards the detector. Convolution-based forced detection has built upon this to provide an appropriate model with lower noise than a fully-Monte-Carlo method [51, 52, 53]. It works by stochastically forcing photons to the detector after each scattering event [21]. Therefore, less photon histories are required, lowering the time required to complete the simulations.

Monte-Carlo is excellent for dual isotope studies where the decays of the two isotopes are close, such as Tc-99m (140keV) and I123 (159keV), though larger energy differences are also possible. Ouyang et al developed a MC simulation-based multi-isotope and multiple-energy Ordered Subset Expectation Maximization (OSEM) reconstruction algorithm that simultaneously corrects for cross-talk and scatter within the reconstruction algorithm for applications in brain SPECT [53]. This method was also applied to In-111 SPECT in a torso phantom experiment and found to be superior to TEW, correcting for scatter of 245keV In-111 photons into its 171keV photo-peak window [54].

### **1.9.8 Effective Scatter Source Estimation (ESSE)**

The ESSE method uses an attenuation map, activity distribution and a set of scatter kernels (pre-calculated using Monte-Carlo) to model the distribution based on an initial estimate of scatter [55]. The scatter kernel describes the position-dependent distribution of scatter. It has been shown to provide superior defect detectability in myocardial perfusion SPECT compared to DEW [56]. In another study, ROC analysis of clinical

patient Tc-99m myocardial perfusion studies comparing TEW and ESSE found that ESSE performed slightly better. The authors noted, however, that clinical implementation of ESSE would be difficult due to the method's long computation time [57].

### 1.9.9 Iterative TEW

To avoid the disadvantages and complexities of convolution and model-based correction methods, yet address the limitations of the modified TEW method, in this thesis we have developed an iterative TEW approach. Iterative TEW is an extension of the modified TEW described in section 1.9.4. The approach to correction for cross-talk with the iterative TEW method has two components: iterative application of the modified TEW estimation followed by a Negative-Selective-Averaging (NSA) filter.

As described in section 1.9.4, the key assumption made by the modified TEW is that the fraction of un-scattered (primary) counts recorded in the scatter windows is proportional to the counts recorded in the primary window (uncorrected for scatter). In regions of mostly Tc-99m, or regions with comparable activities of In-111 and Tc-99m, it has been shown that this approximation is valid [43]. In regions of mostly In-111 activity, however, the uncorrected Tc-99m primary window can contain a large number of scattered In-111 photons. If this is the case, the amount subtracted from the scatter windows is overestimated prior to making the TEW scatter estimate, and the resulting TEW scatter estimate is low. As a result, Tc-99m activity is overestimated.

Generally, the iterative TEW looks to account for the shortfall of the modified TEW approach by first making a modified TEW scatter subtraction, and then using the primary counts in the scatter-subtracted Tc-99m window to update the estimate of

primary counts recorded in each scatter window. The TEW is then re-applied to form the new estimate of scatter in the primary window. This cycle, shown in equation 1-12, iterates until the resulting TEW scatter estimate converges.

$$Tc_{pri}(i + 1) = Tc_{pri}(0) - \frac{w_p}{2} \left( \frac{Scat_{low} - c_1 Tc_{pri}(i)}{w_{low}} + \frac{Scat_{high} - c_2 Tc_{pri}(i) - c_3 In111}{w_{high}} \right) \quad 1-12$$

Here,  $Tc_{pri}(i)$  represents the estimated un-scattered counts recorded in the Tc-99m primary window following the  $i$ th iteration of the modified TEW, In-111 is number of counts recorded in the energy window designated for In-111,  $w_p$ ,  $w_{low}$  and  $w_{high}$  represent the energy widths of the primary, lower, and upper scatter windows,  $Scat_{low}$  and  $Scat_{high}$  represent the counts recorded in the lower and upper scatter windows, and  $c_1$ ,  $c_2$ , and  $c_3$  are experimentally determined constants that represent the ratios  $\frac{Scat_{low}}{Tc_{pri}}$ ,  $\frac{Scat_{high}}{Tc_{pri}}$ , and  $\frac{Scat_{high}}{In111}$  in the absence of scatter. The windows used in this experiment are illustrated schematically in Figure 2-1.

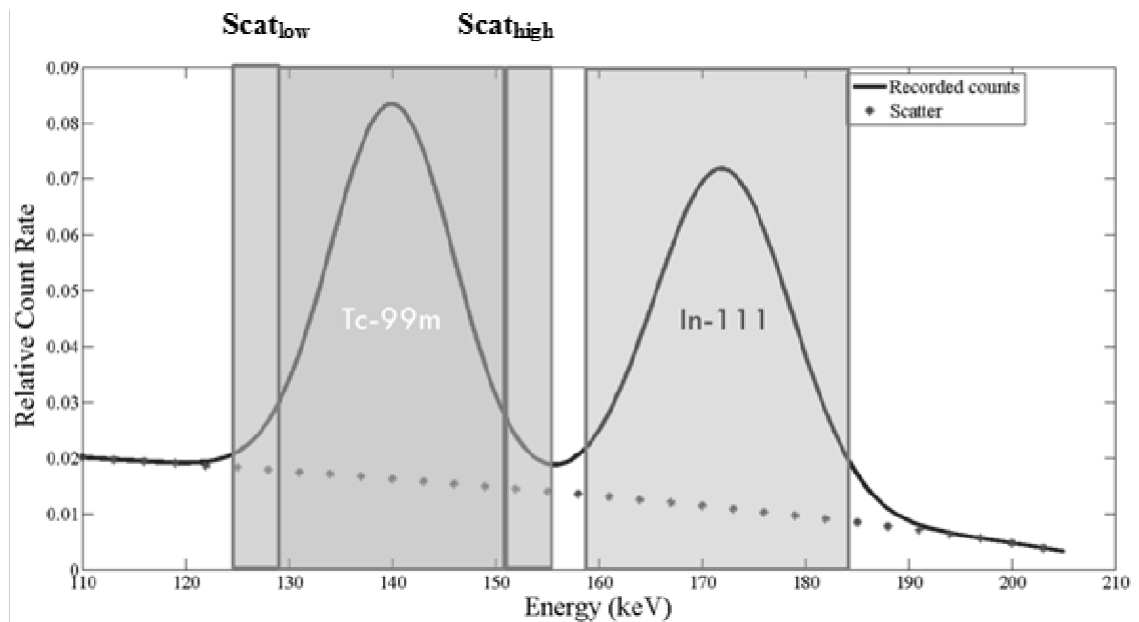


Figure 1-10: Simplified version of a Tc99m & In111 (245keV emission omitted) spectrum. The total counts are the solid black line, and the dotted curve is the contribution of scatter to the detected counts. The small windows surrounding the Tc-99m window ( $Scat_{low}$  and  $Scat_{high}$ ) are the TEW scatter windows.

The algorithm is considered to have converged when the relative change of estimated Tc-99m activity between iterations is less than 0.00001. It takes well under one minute to run with these convergence criteria in MATLAB version 8.0.0.783 (2012b), with an Intel® Core™, i5-2400 CPU @ 3.10GHz, 3.09 GHz, with 3.23GB of RAM so there is limited incentive to analyze the effect of relaxing the convergence criteria.

In order to remove negatives introduced due to noise when the signal measured in the energy windows is virtually all scatter, an extra filter is used specifically in the iterative TEW process. Between iterations (still in projection space) the Negative Selective Averaging (NSA) filter searches for negative projection elements and spreads this negative value equally among each of its neighbours. After doing this, the negative projection element is set to 0, conserving total counts. The filter does one pass through the projections, and can produce negative neighbours when spreading a given negative projection element. The goal of this filter is to conserve total counts, assuming that the negative projection elements only arise from noise. Since negative projection elements cannot be used as inputs to the iterative reconstruction algorithm, the NSA filter is used counteract the bias in the projections caused by truncating negative projection elements prior to the reconstruction step. A visual representation of this filter is shown in Figure 2-2.

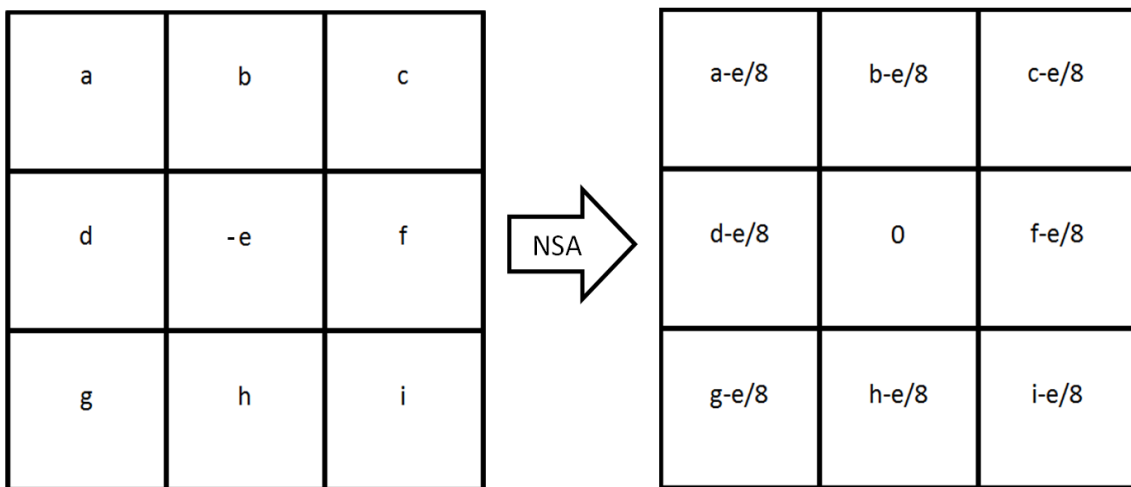


Figure 1-11: Depiction of the NSA filter. It takes a negative projection element (-e) and spreads the negative value evenly with each of its immediate neighbours, replacing its value with 0.

## 1.10 Partial Volume Effect Compensation (PVEC)

The partial volume effect is a problem that is related to modalities with a limited spatial resolution, such as SPECT. In SPECT, the reconstructed image is actually a 3-D convolution of the true activity distribution with the system resolution function. The spatial resolution can be determined by reconstructing the projections from a point source, and fitting the profile across the source with a Gaussian function. Depending on the method of reconstruction, the resolution may differ in the axial and in-plane directions. Measurement of a static point source does not, however, capture all of the factors that contribute to partial resolution losses. Resolution loss may also occur due to movement (such as cardiac and respiratory motion in the heart and lungs). Post-reconstruction filtering, which is commonly used to reduce the appearance of noise in SPECT imaging, will also degrade the image resolution. All of these factors should be considered when estimating the partial resolution effects.

In structures containing activity that are similar in size or smaller than the spatial resolution of the system, PVE becomes noticeable. For a small source with a low-activity background, for example, some counts will “spill-out” of the voxel into neighbouring voxels. This situation is shown in Figure 1-12, with a phantom diameter of 10units, and a system spatial resolution FWHM = 5 units.

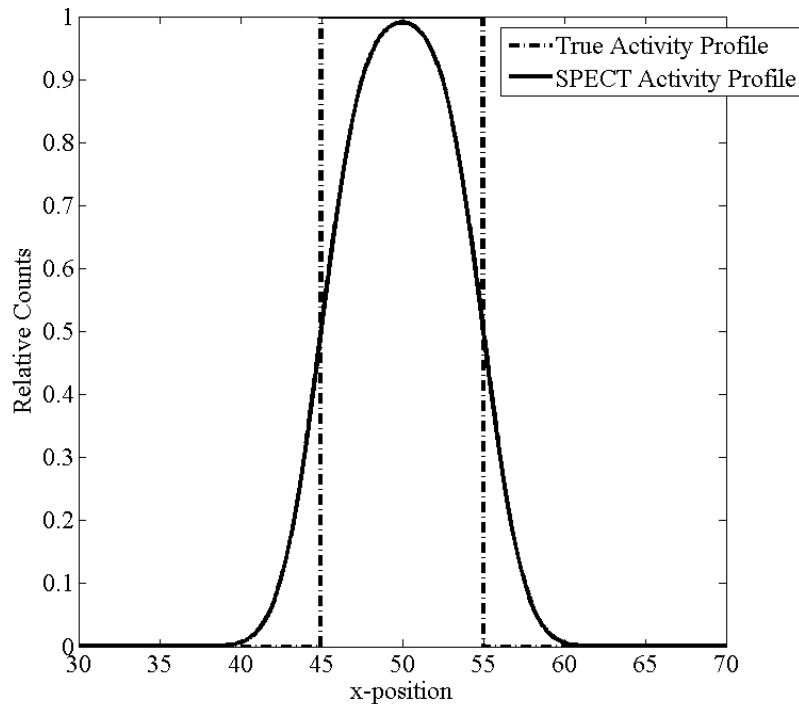


Figure 1-12: Simulated representation of PVE. The total activity of the true source (dashed line) is under-estimated because some photons originating within the ROI are placed outside the ROI in the reconstructed image due to non-zero spatial resolution of the system.

As a result of the limited spatial resolution, the true activity in the area of the source is underestimated, while the background is overestimated in regions near the source. In this example, the true activity would be underestimated by 16%. The recovery coefficient, termed as the fraction of true activity that the anatomically-defined region of

interest (ROI) contains, is 0.84. The recovery coefficients can also be expressed as an inhomogeneous array of values unique to each voxel. For instance, in Figure 1-12 the recovery coefficient is unity at the center of the image, but 0.5 at the edges.

*In vivo*, PVE becomes further complicated when two or more neighbouring structures containing activity can create mutual spill-in/spill-out scenarios, as shown in Figure 1-13 with three structures. This can occur between the heart and liver, for

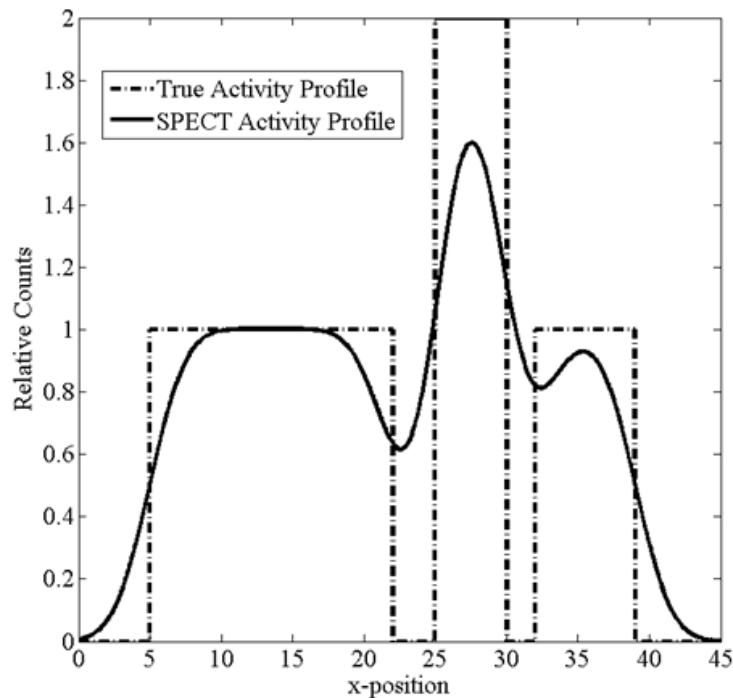


Figure 1-13: PVE with three neighbouring structures. Due to finite spatial resolution, there is a bias in SPECT activity estimates due to counts from the ROI placed outside the ROI in the reconstructed image, as well as counts from neighbouring structures detected within the ROI.

example, in cardiac imaging with Tc-99m-teboroxime [58]. The proximity of these two organs (and uptake of Tc-99m-teboroxime in the liver and stomach) causes extra-cardiac interference from photons in the liver due to a combination of motion and PVE. This can

be a problem clinically, and although cardiologists are trained to “read-around” artifacts such as these, it is sometimes substantial enough to prevent evaluation of the affected portions of the heart.

The following subsections describe ways to avoid or compensate for PVE. This is by no means an exhaustive review of PVE correction, and the interested reader is referred to a helpful review of PVE correction for emission tomography applied to neurology, cardiology, and oncology [59].

### 1.10.1 **Avoiding the problem**

Depending on the experiment or imaging situation, it may not be essential to correct for PVE. Often, it is sufficient to “read-around” the problem, or if it is necessary to obtain quantitative results, one can be clever in avoiding issues where PVE affects the results. For example, if activity *concentration* is the result you are looking for, it may be sufficient to draw a ROI deep within the structure, where edge effects will not play a role in the result. As can be seen in Figure 1-12, the relative counts at the center of the phantom (at position  $x = 14$ ) match up with the SPECT counts.

If one is interested in the total counts and there is a low-activity background, it may be sufficient to extend the ROI well beyond the edges of the physical region containing the activity to collect all of the counts from the SPECT image [60]. Often, phantoms created to determine the effectiveness of scatter and attenuation corrections can be made so that they avoid running into PVE. In these scenarios scatter or attenuation compensation can be fully analyzed, without being distorted by the possibility of inaccurate PVEC [32].

In the situation describing the profiles in Figure 1-13, a large ROI drawn over the whole image could be used to determine the total activity, but it would be difficult to avoid PVE if searching for the activity of only one of the three sources. In this case, PVE compensation must be considered.

### 1.10.2 **Fixing the problem at the source**

The best way to correct for PVE is to address the root cause of the problem. If there are any ways to improve the resolution of the system, these should be explored. This is a large area of study in SPECT, notably in areas where smaller organs are being imaged (small animal SPECT, cardiac SPECT). In these areas, much improvement has been achieved in spatial resolution by introducing multi-pinhole collimators [17], which improve the resolution without a substantial loss in sensitivity compared to parallel-hole collimation. In fact, pinhole collimation can yield a reconstructed spatial resolution that is better than the detector's intrinsic resolution, due to the magnification that occurs in the collimation process [61]. When sufficient reconstructed spatial resolution is not available, researchers have turned to addressing the symptoms of PVE.

### 1.10.3 **Template-Based approach**

The template-based approach generally works by using a template that is supposed to represent the true activity distribution, unaffected by PVE. Using this template, the template is convolved with a Gaussian function representing the resolution of the system. The original template is compared to the convolved template in order to determine the contribution of PVE to the SPECT image.

In order for the template-based approach to work for PVE correction, it is important to have a good segmentation of the object boundaries [62]. This can be achieved with a high-resolution modality such as CT [1] or Magnetic Resonance Imaging (MRI) [63]. Once the object boundaries are defined, the segmented regions are replaced with what the researcher believes to be a good representation of the true activity distribution. The image can be split up into various sub-images, based on the organs or objects involved. For a small source in a low-activity background, the template might be the average intensity value contained in the image, but one is not forced to use a homogeneous template. The background can be set to 0 if it contains negligible activity, or the background could be taken directly from the PVE-degraded image. This template image is then blurred by convolving it with a 3-D Gaussian function representing the true resolution of the system. The convolution can be accomplished by forward-projecting and back-projecting the template, since the SPECT reconstruction software models the point spread function (PSF) of the system [1].

An array of recovery coefficients covering each voxel in space can be produced as described in equation 1-13:

$$\mathbf{R} = \frac{\text{template}(1)}{\text{template}(0)}. \quad 1-13$$

In equation 1-13,  $\mathbf{R}$  is the array of recovery coefficients,  $\text{template}(0)$  is the original template, and  $\text{template}(1)$  is the forward-and-back-projected template. If there are multiple areas of uptake to correct for, the template can be produced by carefully examining each region of the PVE-degraded image and separately producing a template and array of recovery coefficients  $\mathbf{R}$  for each ROI. If two regions are far enough as to not

affect each other, they may be reconstructed together. If two regions have significant overlap, it may be difficult to determine the template to use, and in these cases, template-based approaches to PVEC may not be very accurate. The recovery coefficient is not limited to the range 0-1, as counts from high-activity neighbouring regions can “spill-in”, causing an overestimation of a voxel’s activity in a neighbouring region.

An iterative template-based approach was used in [1]. This method produces a first order PVEC image, and uses this image to adjust the template to better reflect the true activity distribution. The method was tested in a physical phantom simulating the human body, and filled the different phantom compartments with Tc-99m activity. The boundaries were defined using CT, and the templates were produced as the mean of the top 10% of counts in each respective ROI. The background values for the template were taken directly from the PVE-degraded image. With correction for attenuation, scatter, but no PVEC, the activity of large organs was accurately quantified, but the smaller organs were underestimated by 20%-40%. The non-iterative PVEC improved quantification within 3%-22%, and the iterative version fared slightly better with quantification errors between 5% and 15%. In organs of mostly spill-out, the non-iterative version was more accurate.

## 1.11 ***Ex-Vivo* Validation tools in SPECT**

In order to calibrate the SPECT camera and validate reconstruction, scatter correction, attenuation correction, and partial volume correction methods, it is important to have an external measurement of the source activity used in the experiment. It is also important, clinically and experimentally, to accurately measure the activity to be

administered. Two types of tools used in this thesis work are well counters (also called gamma counter) and dose calibrators (ionization chambers).

### 1.11.1 **Well counter (gamma counter)**

Similar to the gamma camera, the detector in most well counters uses a single block of NaI(Tl) crystal. A difference is that the detectors for gamma counters contain a hole for the insertion of a radioactive sample to be measured. Therefore, the detection process is similar to SPECT, using a PMT and analog-to-digital conversion of the signal to keep track of energy information. The main differences between the well counter and a SPECT camera are that:

- 1) There is no positional information required in well-counters
- 2) Well-counters have a much higher detection efficiency

The detection efficiency is very high, due to the absence of collimation and the large solid-angle coverage of the crystal. The only factors degrading detection efficiency are the hole in the crystal for insertion of the source and the intrinsic efficiency of the detector, itself. Standard well-counters have detection efficiencies greater than 90% [11]. Thus, these tools can measure the activity of a sample with high precision, but if the sample activity is too high, pulse-pileup can become a problem.

Pulse-pileup occurs when individual voltage-pulses produced by the PMT occur so close together that they can be recorded as a single event with increased energy. Thus, if the sample activity is high enough, a Tc-99m (140keV emission) sample could produce two energy peaks, one at 140keV and another at 280keV. This can result in inaccurate

activity measurements, as the recorded count-rate of the well-counter is no longer proportional to the sample activity at high enough activities. If this occurs, the sample should be split up into smaller samples and their activities summed together, or one should look into using a less efficient method of counting, such as an ionization chamber.

#### 1.11.1.1 Separation of two signals of different isotopes

Since a well-counter permits energy-windowing, it is possible to differentiate between the signals of two or more isotopes. However, just as in SPECT, cross talk can degrade the accuracy of activity measurements. The activity-time curve of two isotopes, for example, can be modelled as the sum of two exponential functions, as shown in equation 1-14.

$$A_{total}(t) = A_{10}e^{-\lambda_1 t} + A_{20}e^{-\lambda_2 t} \quad 1-14$$

In this equation,  $A_{total}(t)$  is the measured total count rate at time  $t$ ,  $A_{10}$  is the initial count-rate from isotope 1, and  $A_{20}$  is the initial total count-rate of isotope 2. These are the two constants that the researcher is looking for. In the exponents,  $\lambda_1$  and  $\lambda_2$  are the decay constants of isotope 1 and isotope 2.

If isotope 1 decays faster than isotope 2, there will exist a time when  $A_1(t) \approx 0$ , but  $A_2(t)$  is still countable.  $A_{20}$ , and consequently  $A_2(t)$ ,  $\forall t$  is known. With the model

for  $A_2(t)$  in place,  $A_1(t)$  and consequently  $A_{10}$  can be determined by a simple subtraction [11]:

$$A_1(t) = A_{total}(t) - A_2(t). \quad 1-15$$

### 1.11.2 Dose Calibrator

A dose calibrator is a specific type of ionization chamber that is used to assay activity before it is administered to subjects in SPECT studies. They are inefficient counters, and thus are better for measuring high-activity sources. Generally, dose calibrators are made up of an argon-filled chamber [11]. The photons of the source interact with the argon and produce charged ion pairs. There is an applied voltage across the chamber and, therefore, the charges produced will flow towards the anode or cathode and produce a current. If the voltage applied is set up correctly, the current collected will be proportional to the total number of ionizations. These proportionalities vary depending on the energy of the photon that interacts, and thus the dose calibrator can be calibrated for different sample isotopes [11]. The advantage of using a dose calibrator is that they can be used to measure high activities without significant errors. The disadvantage work is that these detectors cannot be windowed to select photons based on photon-energy and thus cannot separately measure the components of a mixed-activity sample.

## 1.12 Objectives/Hypotheses

The objective of this thesis was to improve the quantitative accuracy of small-animal dual-isotope SPECT with Tc-99m and In-111-labeled tracers. The iterative TEW

was hypothesized to perform a more complete scatter subtraction of In-111 cross-talk from the Tc-99m image in regions of mostly In-111, while keeping good quantification in regions of comparable activities. This hypothesis was examined both in phantoms and *in vivo*.

Using the nanoSPECT/CT system, Strydhorst et al. showed that the inter-scan reproducibility of LV systolic and diastolic volume measurements in rats ranged from 4%-7%, and ejection fraction measurements had a reproducibility of 3.1% [64]. Based on these reproducibilities, it was decided that a good objective for quantification would be to target activity estimations for In-111 and Tc-99m within 5% of truth.

# 2 Methods and Materials

The Iterative TEW cross-talk correction method, described in section 1.9.9, was validated experimentally using both phantom and *in vivo* rat experiments. The details of these experiments are provided in the remainder of this chapter while the results and associated discussion are given in Chapters 3 and 4, respectively.

In this chapter, experimental methods were developed to determine scatter and calibration constants critical to the implementation and assessment of the iterative TEW (section 2.1). The iterative TEW was assessed in comparison to the modified TEW, standard TEW, and no correction for cross talk in a physical phantom (section 2.2) as well as *in vivo* in the area of a rat's heart (section 2.3) based on the resulting Tc-99m activity quantification in the different imaging scenarios.

## 2.1 Scatter and Calibration Constants

The scatter correction constants in equation are dependent on the mean  $\mu$  and standard deviation  $\sigma$  of the energy distributions of In-111 and Tc-99m photons detected in the absence of scatter. They are also dependent on the position and size of the scatter windows  $Scat_{low}$  and  $Scat_{high}$ . The mean,  $\mu$ , is the emission energy of each isotope as the camera energy windows are adjusted for this just prior to acquisition. The standard deviation,  $\sigma$ , potentially differs for each detector head of the camera. The Bioscan nanoSPECT/CT manual quotes a limit on the FWHM of the detector response to Tc-99m photons to be 9.7% of the mean, resulting in  $\sigma = 5.80\text{keV}$ .

In order to get a more accurate measurement of the energy resolution specific to our camera, the resolution of each detector was separately measured. Small Tc-99m and In-111 sources (~0.1mL) were prepared by injecting a known volume of In-111-chloride and Tc-99m-pertechnetate into 1.5mL flex tubes [65].

Each source was raised above the rat-bed using Styrofoam to be close to the centre of the FOV of the camera in order to lessen the effects of back-scatter. The detector head being tested was rotated to be directly above the source. All other detector heads were turned off. A set of 5 minute planar images was acquired, sampling the energy spectrum at intervals of 2keV, using an energy-window width of 1% of the centroid energy. The 5-minute acquisition time was used to ensure that the Poisson counting error was less than 1% at each peak. A total of 32 data points were obtained for each spectrum. The sum of counts of each head was used, decay corrected to the time of the first acquisition. For Tc-99m, the spectrum was sampled from 118keV to 164keV, and for In-111, the spectrum was sampled from 148keV to 194keV, sampling the peak of the In-111 171keV emission. For each isotope and each head, the spectrum was fit with 5 parameters  $x_i$  defining a Linear + Gaussian function (equation 2-1). The function was fit in a least-squares sense using the MATLAB built in function called “lsqcurvefit.” The fitting function was chosen to represent the combination of a Gaussian intrinsic energy resolution and a linear scatter contribution, which is the same assumption made by TEW.

$$ydata = x_1 * xdata + x_2 + x_3 * e^{-\frac{(xdata-x_4)^2}{2x_5^2}} \quad 2-1$$

Parameter  $x_5$  (equation 2-1) provided the standard deviation  $\sigma$  of the energy spectrum. The linear portion described the small amount of scattered photons within the

source, collimator, and detector. Using the fitted parameters defining the mean and width of each Gaussian function, the constants  $c_1$ ,  $c_2$ , and  $c_3$  were determined using equations 2-2, 2-3 and 2-4 . Here, the Gaussian energy resolution function is integrated across each scatter window and primary window. The constants  $c_1$  and  $c_2$  represent overlap of the 140keV Tc-99m peak across the windows  $Scat_{low}$  and  $Scat_{high}$ , respectively, while  $c_3$  represents the overlap of the 171keV In-111 peak across the  $Scat_{high}$  window. Due to the fact that the camera limited us to the acquisition of counts in up to four energy windows, however, we were forced to use a single window to cover both In-111 emissions. In equation 2-4, the extra constant  $\epsilon$  is the fraction of total un-scattered In-111 counts detected as 171keV photons. This was determined using the theoretical emission frequency of the 171keV emission compared to the frequency of both the 171keV and 245keV emissions together, as well as the proportion of each emission covered by the large energy window designated to cover both In-111 emissions. The constant  $\epsilon$  was determined to be very close to 0.5.

$$c_1 = \frac{\int_{Scat_{low}} Gauss_{Tc99m}(\mu, \sigma) dE}{\int_{Tc_{pri}} Gauss_{Tc99m}(\mu, \sigma) dE} \quad 2-2$$

$$c_2 = \frac{\int_{Scat_{high}} Gauss_{Tc99m}(\mu, \sigma) dE}{\int_{Tc_{pri}} Gauss_{Tc99m}(\mu, \sigma) dE} \quad 2-3$$

$$c_3 = \frac{\int_{Scat_{high}} Gauss_{In111}(\mu, \sigma) dE}{\int_{In111} Gauss_{In111}(\mu, \sigma) dE} \epsilon, \quad 2-4$$

$$\epsilon = \frac{\int Gauss(In111_{171keV}) dE}{\int Gauss(In111_{171keV}) dE + \int Gauss(In111_{245keV}) dE}$$

The calibration factor for converting reconstructed SPECT count rate to absolute activity was determined using a 100 $\mu$ L Tc-99m source of known activity measured using the dose calibrator. The iterative TEW was applied to the projections before reconstruction. This subtracted approximately 4% from the total counts in the projections, which were predominantly scatter within the source, from the imaging bed, as well as some scatter inside the detector. The projections were reconstructed with attenuation correction as described in section 2.2.3. A large spherical ROI was used ensuring that all counts from the source were contained within the ROI. The resulting calibration factor,  $k$ , was determined using equation 2-5.

$$k = t * \frac{A_{truth}}{C_{spect}} \quad 2-5$$

Here,  $t$  is the time per projection in the SPECT acquisition,  $A_{truth}$  is the dose calibrator activity adjusted for decay between the dose calibrator measurement and the start of the SPECT acquisition, and  $C_{spect}$  is the counts measured inside a large ROI completely covering the reconstructed image of the calibration source. The calibration factor,  $k$ , was determined to be 0.000953 MBq/cps for Tc-99m and 0.000752 MBq/cps for In-111.

An open protocol, using one window over the entire spectrum, was used for gamma counting. In order to properly deduce the activity of a sample of In-111 or Tc-99m from the count-rate of the detector, it was necessary to calibrate it against the dose calibrator. For the Tc-99m calibration, six samples of Tc-99m-pertechnetate, each approximately 100 $\mu$ L in volume, were produced. The respective activity of each sample was measured

with the dose calibrator and then left to decay for two days. This was done so that the uncertainty in the dose calibrator measurement was low. Once the activity was low enough—on the order of  $1\mu\text{Ci}$ — with minimum count losses due to dead-time (pulse pile-up, etc.), the samples were measured every 40 minutes for the next two days to produce a calibration curve. The well counter specifications manual states that dead-time error is  $< 1\%$  if the count rate is  $< 2\text{Mcpm}$  [66].

## 2.2 Phantom Validation

The accuracy of the iterative TEW method was evaluated using a simple physical phantom. The phantom was the plastic cylinder shown in Figure 2-3. The different correction methods —standard TEW, modified TEW, iterative TEW— were compared qualitatively and quantitatively based on resulting images acquired within the Tc-99m photo-peak window.



Figure 2-3: The plastic cylinder phantom used in the study.

### 2.2.1 Phantom Preparation

Phantoms were prepared by injecting known activities of Tc-99m-pertechnetate and In-111-chloride into the plastic cylinder using a syringe. The empty plastic cylinder phantom had inner diameter  $18.0 \pm 0.5\text{mm}$ , height  $15.0 \pm 0.5\text{mm}$ , and mass  $1.965 \pm 0.002\text{g}$ . When preparing phantoms containing both isotopes, the Tc-99m activity was measured with a dose calibrator [67] directly from the phantom prior to the injection of In-111 into the phantom. The In-111 activity was measured as the difference in syringe activity before and after injection into the phantom. In phantoms containing only In-111, the In-111 activity was measured directly from the phantom post-injection. The activities used for the different phantoms are outlined in Table 2-1. Following the injection of known activities of both isotopes, the mixture was diluted with saline to a total volume of approximately 2mL and thoroughly mixed. For all phantoms the total volume of the solutions, measured using the CT images, ranged between 1.6mL and 2.2mL.

Table 2-1: Activities used in the mixed isotope phantom experiment are shown below. Errors represent the error in calibration for each isotope, quoted in the owner's manual.

$\frac{Tc-99m}{In-111}$ Activity fraction	Tc-99m Activity ( $\mu\text{Ci} \pm 2\%$ )	In-111 Activity ( $\mu\text{Ci} \pm 2\%$ )
0	0	220
0.15	112	734
0.28	124	436
0.52	147	279
0.99	197	198
2.47	270	109
6.90	729	106

The dose calibrator error was measured by determining the amount by which the activity measurement varied with position of the source within the chamber as well as the change in activity measurement when the activity was diluted. When the source was

positioned in the bottom of the cavity, the activity was underestimated by 3% compared to the centre of the chamber. At the edges of the chamber (in the axial direction) the activity measurement increased by 1% compared to measurement at the centre of the chamber. Attenuation effects (comparing activity measurement of a 0.1mL source in a syringe compared to a dilution to 0.9mL in the syringe) resulted in a decrease in activity measurement by  $< 0.5\%$ .

The dose-calibrator measurements for In-111 activity in the phantoms were performed differently than for Tc-99m. In-111 activity was measured as a difference in syringe activity before and after injection into the phantom, while Tc-99m phantom activity was measured directly from the phantom before the injection of In-111. Due to differences in geometry and attenuation in the source, these might not result in the same quantification. In order to assess this, ten plastic cylinder phantoms of Tc-99m were made. The activity was measured both as the difference in syringe activity and directly from the cylinder. The average per cent difference between the two measurement techniques over the set of ten phantoms was  $0.22\% \pm 0.69\%$ , and the per cent difference ranged between  $-3.1\%$  and  $+2.3\%$ . It was determined that based on the effects of geometry and measurement techniques, a 2% dose-calibrator error would be appropriate.

### **2.2.2 Data Acquisition**

A nanoSPECT/CT preclinical imager was used throughout the study [31]. It permits SPECT studies of animals of different sizes with interchangeable apertures and beds. In total, 48 SPECT projections were acquired with four camera heads  $90^\circ$  apart. This resulted in projections acquired  $7.5^\circ$  apart, covering  $360^\circ$ . The bed translated

between projections, resulting in a helical acquisition pattern. For this study, rat-designated multi-pinhole collimators were used with 9 pinholes (diameter = 2.5mm), to focus 9 projections of the image onto each NaI(Tl) detector panel. The system allows projections to be acquired in up to 4 different user-defined energy windows per scan. The energy windows used for all experiments in this study are presented in Table 2-2. Each projection was acquired for 150 seconds. This time was chosen so that in the lowest phantom activities used, Poisson counting error would be  $< 0.5\%$ . This is small next to our target accuracy of 5%. To gain anatomical information and to produce attenuation maps, CT acquisitions were performed prior to each SPECT acquisition without moving the phantom between scans. The x-ray tube voltage was 45kV<sub>p</sub>; the tube current was 177 $\mu$ A, and the exposure was 1500ms. 360 x-ray projections were acquired per CT scan.

Table 2-2: Energy windows used for all experiments

<b>Window Name</b>	<b>Centroid Energy (keV)</b>	<b>Width (keV)</b>
Tc-99m low scatter	126	6.3
Tc-99m high scatter	154	7.7
Tc-99m primary	140	21
In-111 primary	211	105.5

### 2.2.3 Image Processing

In order to reduce the effects of noise on the scatter estimates, all of the projection sets in the mixed isotope phantoms were pre-filtered with a 2-D Gaussian low-pass filter ( $\sigma=1.0$ mm). This filter was chosen because it is a non-negative filter in both the Fourier and Spatial domain. Noise is expected to be especially apparent in regions of only In-111. Where only scatter is present, noise in the scatter estimate can lead to negative values in the corrected projections which can cause problems during reconstruction.

Four separate sets of Tc-99m projections were collected:

1. No scatter correction
2. Standard TEW subtraction
3. Modified TEW subtraction
4. Iterative TEW subtraction

One set of In-111 projections was collected:

1. No scatter correction

The CT projections were reconstructed using the Feldkamp cone-beam reconstruction algorithm [68], with correction for beam hardening. The code was developed by Strydhorst and Wells [30]. The reconstructed CT voxel size was  $(0.2 \times 0.2 \times 0.2) \text{ mm}^3$ . The resulting CT scan was used to produce an attenuation map for the SPECT reconstruction [30].

The SPECT projections were reconstructed using OSEM code (32 total iterations) that was developed by Strydhorst and Wells [30]. It uses a CT-based attenuation map to correct for position-dependent attenuation, also correcting for decay of the isotope between projections. The system matrix was created by ray-tracing a digital model of the rat aperture. The OSEM splits the projections into 6 subsets for iterations 1-8, 4 subsets for iterations 9-16, 3 subsets for iterations 17-24, and all of the projections are used for the iterations 25-32. Therefore, a total of 32 iterations with 112 sub-iterations are used. Reconstructed voxel size is  $(0.6 \times 0.6 \times 0.6) \text{ mm}^3$ . Unless otherwise specified, post-reconstruction filtering was applied on all images with a 3-D Gaussian kernel with FWHM=0.6mm.

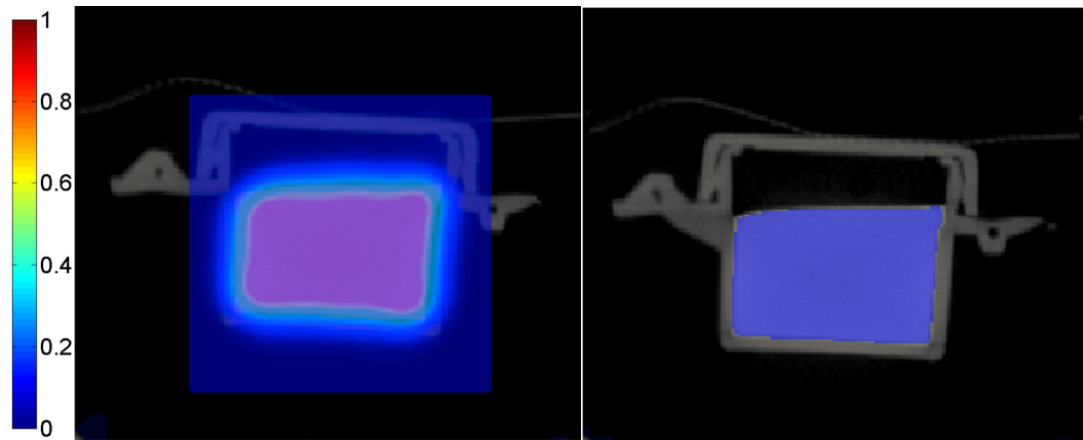


Figure 2-4: ROI used to determine activity of plastic cylinder phantoms (blue). The grayscale image is the CT scan and the jet colour-map image is the co-registered SPECT image, with voxel intensities normalized to 1. Left: ROI used in avoiding the partial volume effect. Right: ROI used when PVEC is applied. SPECT image is left out on the right for easier comparison of the ROI to the CT image.

#### 2.2.4 Image Analysis

The image analysis of the phantoms is split up into two parts: the first part uses the phantom containing only In-111. In this phantom, analysis was carried out in projection space and image space to determine the cross-talk fraction (fraction of In-111 counts falsely detected as Tc-99m), before and after the application of the different compensations for scatter. The second part contains analysis of the phantoms containing mixtures of different  $\frac{Tc-99m}{In-111}$  activity fractions. Analysis of these phantoms was carried out only in image space. Here, total SPECT activity estimates of reconstructed In-111 projections and different reconstructed Tc-99m projections (with and without corrections for cross-talk) were compared to the dose calibrator measurements.

### Only In-111

In order to quantitatively analyze the cross-talk fraction for each method, each phantom image from the In-111-phantom reconstruction was split up into ten sub-images consisting of the coronal slices with the highest total counts in the In-111 image. For each slice, the ROI was selected by including all counts that were greater than 35% of the maximum voxel in the respective slice of the In-111 image. The cross-talk fraction XTF of each slice in each Tc-99m-window image of  $Im_x$  was calculated using equation 2-6. In

$$XTF(Im_x) = \frac{\sum_{i(ROI)} Im_x(i)}{\sum_{i(ROI)} In111(i)} \quad 2-6$$

this equation, In-111 represents the In-111 image with no scatter correction.

The dependence of XTF on position of the slice in the phantom was analyzed, and the different scatter compensation methods were compared using t-tests and F-tests between these data sets. The most complete scatter compensation method was chosen as the method that produced an image with the lowest XTF and the smallest deviation between slices.

The XTF resulting from the different scatter compensation methods was also analyzed in projection space. Included in the analysis was the effect of pre-filtering all projections with a 0.5mm Gaussian low-pass filter before making the scatter estimate, truncating negative projection elements, and inclusion of the NSA filter on the negative projection elements. The effect of varying the standard deviation of the Gaussian low-pass filter applied to all sets of projections prior to making the scatter estimates was also explored.

## Mixed Tc-99m and In-111 Phantom

The reconstructed SPECT activity of each image was evaluated by placing a large cylindrical ROI over the phantom ensuring that all counts originating from the phantom were included. This large ROI, shown on the left side of Figure 2-4, was used in order to avoid PVE. The same ROI was used for all reconstructed images resulting from a given phantom acquisition. The sum of counts in the ROI was converted to SPECT activity using the calibration factor determined in section 2.1. For each image, the normalized activity recovery, defined as  $\frac{A_{SPECT}}{A_{dose\ calibrator}}$ , was used to quantify the effectiveness of the SPECT activity estimations. In this equation,  $A_{SPECT}$  is the SPECT activity estimate, while  $A_{dose\ calibrator}$  is the dose calibrator activity measurement.

In order to compare the effectiveness of the iterative TEW to the modified TEW, each phantom image was split up into the ten slices of highest activity. The ROI for each slice was selected using a threshold of 40% of the maximum voxel intensity in the given slice. This was chosen to ensure that PVE did not play a large role in the activity concentration calculation. For each slice, the SPECT activity concentration (modified TEW and iterative TEW) was compared to the true activity concentration determined using the CT-volume and dose calibrator activity measurements. Two paired t-tests were performed on each set of activity-slice concentrations. The first tested whether the iterative TEW was significantly lower (at 95% confidence) than the modified TEW Tc-99m activity estimate. The second paired t-test compared the accuracy of the two images, using the absolute difference between the SPECT activity concentration and the true activity concentration (at 95% confidence), described in equation 2-7. In this equation,  $A_{SPECT}(slice)$  is the SPECT activity measurement of a given slice,  $Volume(slice)$  is the

volume contained by the slice,  $A_{dose\ calibrator}$  is the total phantom activity determined using the dose calibrator, and  $Volume(phantom)$  is the total volume of the phantom, determined from the CT reconstructed image.

$$accuracy = \left| \frac{A_{SPECT}(slice)}{Volume(slice)} - \frac{A_{dose\ calibrator}}{Volume(phantom)} \right| \quad 2-7$$

In preparation for *in vivo* image analysis where visible background activity exists, a subset of the phantom images was analyzed in a different way. The CT-image was used to manually segment the part of the SPECT image that truly contained the activity, shown on the right side of Figure 2-4. There was good contrast between the walls of the phantom, the contents, and the background, leaving little ambiguity regarding the region to segment. Due to the high resolution of CT, the PVE was much less noticeable in the CT image of the phantom compared to the SPECT image.

Compensation for the partial volume effect was done using a template based approach similar to method M1 by Shcherbinin and Cellar [1], described in more detail in section 1.10.3. To perform PVEC for this plastic cylinder phantom, a template was used consisting of the top 10 per cent of counts within the ROI in the region of the phantom, and a background of 0. This template was chosen to represent an image more similar to the true image, in the absence of noise and resolution loss caused by the detection and reconstruction processes. The template was forward-projected and back-projected in order to determine the proportion of counts from inside the ROI in the true image that were placed outside of the ROI in the reconstruction (known as spill-out).

The recovery coefficient was given by the array  $R_i = \frac{C_{REPROJECTED_i}}{C_{TEMPLATE_i}}$ . This provides a unique recovery coefficient for each voxel, depending on the geometry. A voxel in the center of the ROI should not gain or lose much activity, and therefore  $R_i(\text{center}) \sim 1$ . The activity using template-based correction for the partial volume effect was compared to the activity determined using a large ROI.

## 2.3 *In vivo* Validation

The general procedure involved in the *in vivo* portion of the study can be described as follows:

- 1) Preparation of the animal model.
- 2) Acquire SPECT projections of cross-talk-degraded image, perform scatter corrections, and reconstruct the projections.
- 3) Determine “gold-standard” activity.
- 4) Compare gold-standard activity to different cross-talk corrected images.

### 2.3.1 Animal Model

Male Sprague-Dawley rats were chosen as the subjects, as they are commonly used in small-animal cardiac research, and many tracers are available for imaging with these animals. They have larger hearts than mice, which should result in less image degradation due to PVE and more accurate, albeit still limited, segmentation.

In order to generate cross-talk *in vivo*, it was necessary to use an In-111 tracer and a Tc-99m tracer that would be taken up in the same region. This would result in cross-talk

of In-111 photons into the Tc-99m energy window and cause an overestimate of Tc-99m activity.

For the tracers, In-111-liposome and Tc-99m-tetrofosmin were used. In-111-liposome is a blood-pool tracer and Tc-99m-tetrofosmin is a commonly used blood flow tracer that uptakes in the myocardium. It was hypothesized that the presence of In-111-liposome in the blood pool (ventricles, atria, and aorta) of the rats would scatter into the myocardium and be falsely detected as Tc-99m, resulting in an overestimation of Tc-99m myocardial activity. There would also be a contribution from the In-111 in the blood within the arteries and veins supplying blood to the myocardium. Here, due to the limited spatial resolution of SPECT, the image voxels would contain both Tc-99m and In-111, similar to the mixed state studied in the phantoms, resulting in the highest level of cross-talk. It would also scatter in the ventricles, and be detected as if there was Tc-99m present in the blood-pool, decreasing the contrast in the Tc-99m image between the myocardia and ventricles. Furthermore, it was hypothesized to uptake in the gut, creating extra-cardiac interference. Correction for the cross-talk was hypothesized to remove the false scattered counts in the myocardium and chambers detected as Tc-99m, improving the accuracy of Tc-99m total heart activity estimation and improving Tc-99m image contrast between the myocardium and heart chambers.

### **2.3.2 Data Acquisition**

The data acquisition is split up into two parts. The first makes up the acquisition of the *in vivo* SPECT data, and the second part makes up the acquisition of an independent *ex vivo* measurement for gold-standard comparison.

### ***In Vivo***

6 male Sprague-Dawley rats were used in this procedure. A small animal gating system was used to monitor the respiratory and heart rate of the rats, and the rat bed was kept at 35°C to maintain the temperature of the animals. Once the rat was anesthetized with 2-3% Isoflurane, it was weighed and placed on the bed in a supine position. Approximately 2.5mCi of Tc-99m-tetrofosmin (exact injected doses listed in Table 2-3) was injected into the tail vein of the rat. Following the injection, a scout radiograph of 500ms with tube energy 45kV<sub>p</sub> and tube current 177μA was performed. The scan range was chosen based on this scout scan. Following the selection of scan range, a circular CT acquisition was acquired of 360 projections, exposure time of 1500ms, with tube energy 45kV<sub>p</sub> and tube current 177μA. 45 minutes after the Tc-99m injection, two sequential helical SPECT acquisitions were performed, each consisting of 48 projections, 75s each, evenly spaced by 7.5°. The low acquisition time per projection (75s) compared to that of the phantom studies (150s) was done to shorten the total acquisition time. This allowed time to acquire multiple SPECT images and thereby estimate the biological clearance of the tracers from the heart. The projections were binned into 4 separate images using four different energy windows. They were the same windows used in the phantom experiments, outlined in Table 2-2.

Following two SPECT acquisitions of only Tc-99m-tetrofosmin in the FOV, approximately 1.5mCi of In-111-labelled-liposome was injected into the tail vein of the rat (Table 2-3). Approximately five minutes was required to wait for sufficient uptake of the In-111 tracer throughout the circulatory system, after which two further sequential SPECT acquisitions, identical to before, were performed. For these acquisitions, both

isotopes were present in the FOV; they were true dual isotope SPECT acquisitions. The injected activity of each isotope in the 6 rats is outlined in Table 2-3, and a simple block diagram of the SPECT/CT acquisition process is laid out in Figure 2-5.

Table 2-3: Mass, heart mass, Tc-99m injected activity and In-111 injected activity of each rat.

Rat#	Mass (g)	Heart Mass ( $\pm 0.05g$ )	Tc-99m injected activity ( $\pm 0.002mCi$ )	In-111 injected activity ( $\pm 0.002mCi$ )
1	274.0	1.15	2.091	1.426
2	285.3	1.20	1.905	1.431
3	470.4	2.15	2.354	1.304
4	494.5	1.55	2.146	1.346
5	455.4	1.50	2.529	1.407
6	500.2	1.55	2.441	1.432
<b>Mean</b>	413 $\pm$ 39	1.52 $\pm$ 0.13	2.24 $\pm$ 0.09	1.391 $\pm$ 0.020

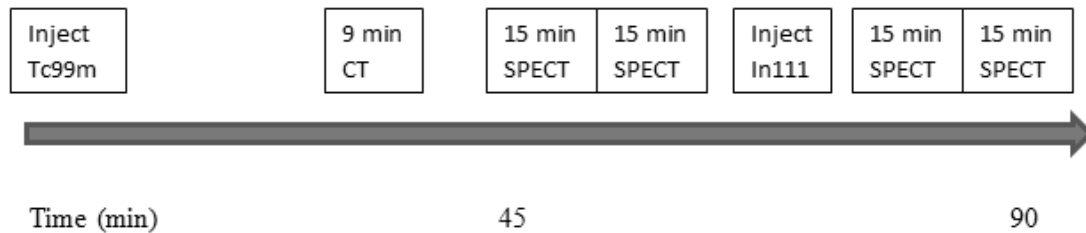


Figure 2-5: Block diagram describing the SPECT/CT acquisition process for each rat. A CT scan was acquired for attenuation correction and anatomical information. Four SPECT acquisitions were done for each rat: two with only Tc-99m-tetrofosmin present, and two with both Tc-99m-tetrofosmin and In-111-liposome present.

### **Ex Vivo (“Gold Standard”)**

Immediately following the fourth SPECT acquisition, the rat was taken out of the gantry and euthanized with an anesthetic overdose of sodium pentobarbital. The heart of the rat was removed approximately 5 minutes following the end of the SPECT acquisition. After allowing blood to seep out into a sample container, the heart was

weighed. The average heart mass was  $1.52 \pm 0.13$ g. The heart was then carefully cut into 40 small segments of roughly the same size, and each segment was placed into a 1.5mL Eppendorf sample container [65].

Three planar gamma camera acquisitions were performed using parallel-hole collimators to determine the relative Tc-99m activity lost to the tools during the sectioning of the heart. The same four energy windows were used, outlined in Table 2-2. The first scan was used to determine the background level, the second was done on the tools and cutting board after cutting up the heart, and the third was done on the samples. The resulting images are shown in Figure 2-6. The sample image was decay corrected to the time of the first image. The modified TEW was performed on the samples and tools images, using the sum of counts acquired in each energy window as the inputs, rather than on a pixel-by-pixel basis to reduce noise propagation in the scatter estimate. Using

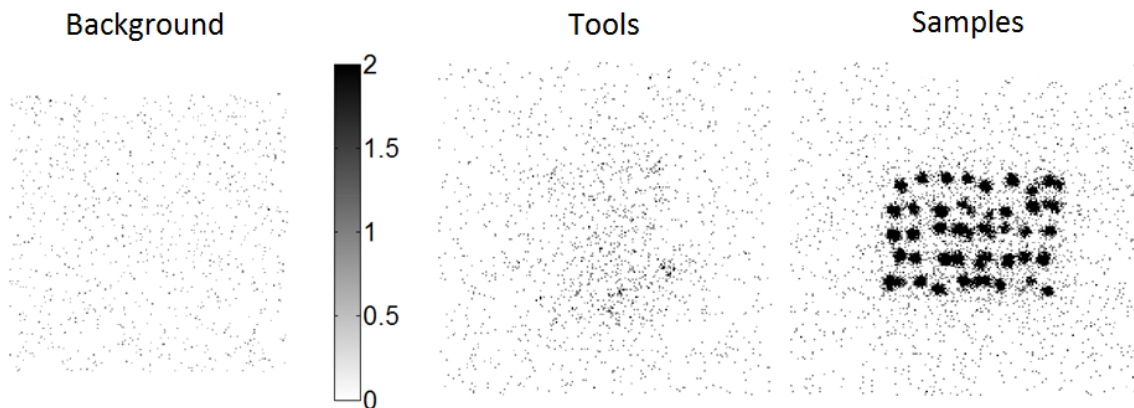


Figure 2-6: Tc-99m planar gamma camera image of background (left), tools (centre), samples (right). Quantitative information from these acquisitions was used to determine the fraction of Tc-99m heart activity retained in the samples after sectioning the heart into 40 pieces.

the modified TEW images, the fraction  $F_{samples} = \frac{C_{samples} - C_{bck}}{C_{tools} + C_{samples} - 2C_{bck}}$  was used to determine the amount of Tc-99m activity that was retained in the sample containers, and was used as a correction factor on the gold standard activity measurement.

Each heart sample was counted in the well-counter for 60 seconds twice per day for 7 days. Curve stripping (section 1.11.1.1) was used on the samples to separate the combination of exponential decay functions for the two isotopes. It was assumed that after approximately 3 days, only In-111 was present. After this period of time, the Tc-99m sample was < 0.03% of its day 0 activity.

### 2.3.3 Image Processing

Correction for scatter in the Tc-99m image was explored in the same way it was for the phantom experiments. The same sets of projections were produced as described in section 2.2.3.

The heart in the SPECT image was segmented manually using the image produced by the iterative TEW method. The left ventricle (LV) myocardium was segmented using a 40% threshold of the maximum voxel intensity value. In order to segment the right ventricle (RV) myocardium, the spline tool was used in 2-D on the different images using the transverse, sagittal and coronal views, shown in Figure 2-7. The 3-D rendered image (shown in Figure 2-8) was also used to view the resulting shape of the ROI. Obvious segmentation defects noticeable in the 3-D image were adjusted so that the resulting image had smooth, closed surfaces. The heart volume was determined using the measured heart weight and by assuming that the myocardium had a density of

1.055g/cm<sup>3</sup>. The segmented heart was constrained to have a volume within 0.5% of this calculated volume, which is much less than the uncertainty in the weight of the rat.

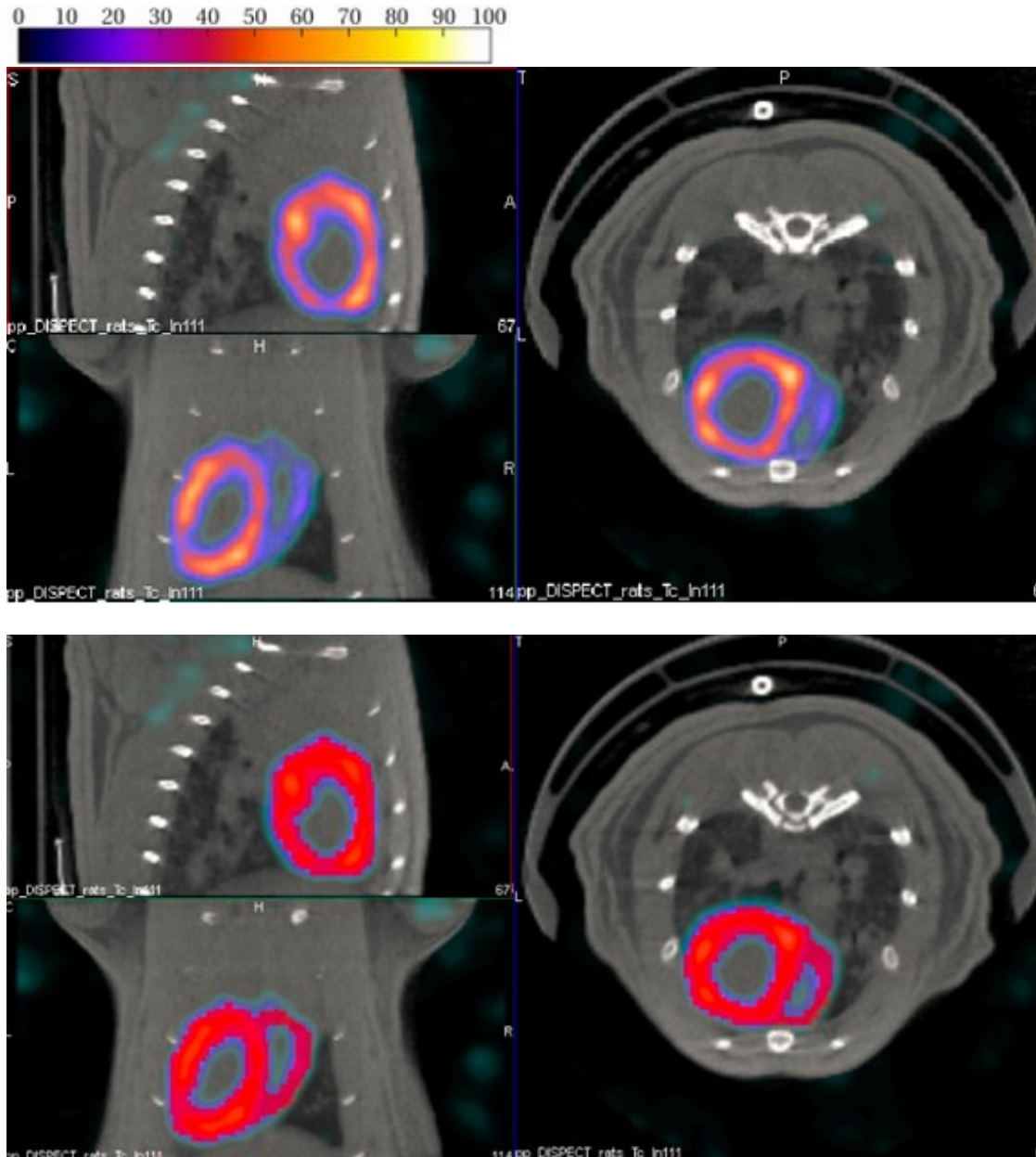


Figure 2-7 top: Coronal (bottom-left), sagittal (top-left), and transverse (right) slices of the heart (colour) after iterative TEW scatter correction co-registered with CT reconstruction (grayscale). The SPECT image is scaled such that the maximum voxel intensity value is 100.

Bottom: same image but different slices, with manually segmented ROI overlaid in red. These segmentations, along with PVEC, were used to quantify the total myocardial Tc-99m activity in the SPECT image.

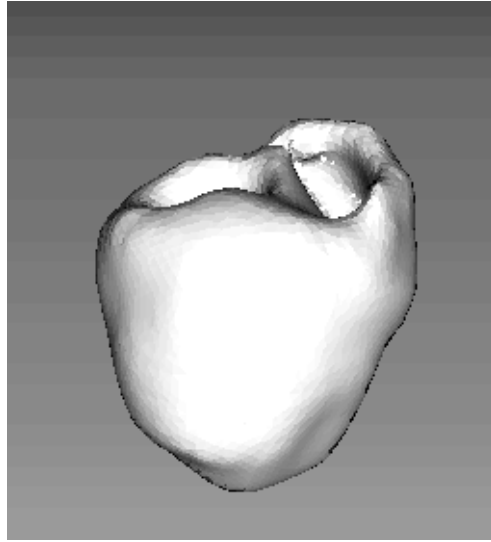


Figure 2-8: 3-D-rendered image of the heart ROI used to aid in manual segmentation of myocardia in SPECT images.

An accurate total heart activity measurement in a rat required accounting for PVE. A template-based approach similar to that done by Shcherbinin [1], as tested in the phantoms, was used to compensate for PVE. The template consisted of 2 regions: the background and the heart volume of interest (VOI).

**Background:** Unlike in the phantom experiments, there was non-negligible activity in the background that had to be taken into account. Tc-99m-tetrofosmin was taken up in the regions surrounding the heart (mostly lungs, liver and gut), and there remained some residual In-111 cross-talk following the iterative TEW correction. Shcherbinin and Cellar [1] used the actual non-uniform image of the background as the background template. I believe that for an image such as the rat heart, there would be too many spill-out counts from the heart included in the background image, overestimating the background contribution to the image. This may explain why his method underestimated the heart

activity by more than 10% in their phantom experiment. To avoid running into this problem, a different (but still simple) method was used to generate the background part of the template image. The heart VOI was dilated by 4.2mm, and the mean voxel intensity value of the surface of this VOI (Figure 2-9) was chosen as the uniform background in the template.

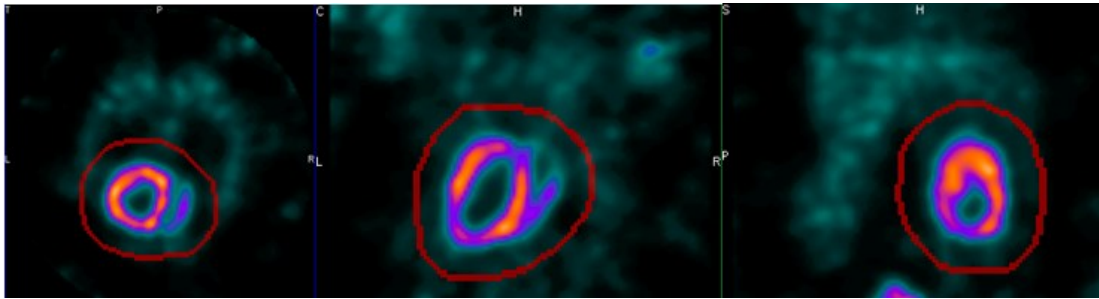


Figure 2-9: 3-D surface used to estimate average background activity in template-based PVEC (red ROI). Left to right: trans-axial, coronal, sagittal slices.

**ROI:** As done by Shcherbinin [1], the VOI template consisted of a uniform activity equal to the mean of the top 10% of voxels in the segmented heart image. This avoided using the noisy maximum voxel value, as well as the mean voxel value, which would be an underestimate of the true heart uptake. This template was forward-projected and back-projected with attenuation correction, using the same reconstruction software that produced the image. The activity recovery array (equation 1-13) represents a unique recovery coefficient for each voxel inside the VOI.

The iterative TEW images of each rat were used to generate unique PVEC templates, and these templates were applied to the other images (no scatter correction, modified TEW, standard TEW). For one rat, 5 separate segmentations for the heart were

used to generate 5 separate PVEC activity estimates. The PVEC total activity estimate varied by < 1% between segmentations.

### 2.3.4 Analysis

The reconstructed heart images were visually assessed in order to qualitatively determine the degradation in Tc-99m image due to the presence of In-111 cross-talk and to qualitatively determine the effectiveness of the cross-talk correction methods.

For semi-quantitative results, time activity curves (TACs) were produced for each cross-talk correction method, using the segmentation described in section 2.3.3 for each rat. The Tc-99m activity for each rat was normalized to the activity in the uncorrected scan 1 image. This curve is not intended as an important quantitative measure, but it is a good indicator of the presence of cross-talk in the uncorrected images, and the correction for this phenomenon.

For true, quantitative results, the “gold-standard” activity for each heart was calculated using equation 2-8:

$$A_{GoldStandard} = \kappa \frac{cpm(t_{scan})}{F_{samples}}. \quad 2-8$$

In this equation,  $\kappa$  is the calibration factor relating the cpm of the well-counter to absolute Tc-99m activity,  $cpm(t_{scan})$  is the decay corrected Tc-99m cpm of the well-counter to the start of the SPECT acquisition, and  $F_{samples}$  is the resulting fraction of total activity that was retained in the sample containers, determined using the planar gamma counter acquisitions. The SPECT estimate of total heart activity was determined using the sum of counts in the manually segmented image with PVEC described in section 2.2. For Tc-

99m activity estimate, the SPECT activity calibration factor from section 2.1 was used. For each reconstructed Tc-99m image, the normalized activity recovery was calculated using  $\frac{A_{SPECT}}{A_{GoldStandard}}$ . The average normalized activity recovery across the six rats was used to quantify the accuracy of each cross-talk correction method. The mean normalized total-heart activity recovery of the iterative TEW was compared to the modified TEW using t-tests. One t-test was used to determine if the iterative TEW activity estimate was significantly lower than the modified TEW, and the other was used to determine if one method was significantly more accurate (using the absolute accuracy) than the other.

In order to quantitatively assess the different cross-talk correction methods in regions of only In-111, a small ROI was placed in the central LV cavity of each rat, so as to minimize the inclusion of Tc-99m photons originating from the myocardium due to PVE. The amount of residual scatter in this region was compared between the modified TEW, iterative TEW, and standard TEW.

# 3 Results

In this chapter, important experimental results are presented. Results for experiments to determine scatter and calibration constants crucial for the implementation and comparison of the quantitative accuracy of the different corrections for cross talk are presented in section 3.1. Results for physical phantom and *in vivo* validation experiments are presented in section 3.2 and section 3.3, respectively.

## 3.1 Scatter and Calibration Constants

The resulting energy spectra for each head in response to Tc-99m and In-111 photons are shown in Figure 3-1 and Figure 3-2. The minimum peak counts/keV was approximately 40 000, which resulted in a Poisson counting error of 0.5%.

The energy resolution of each camera head in response to 171keV In-111 and 140 keV Tc-99m photons, as well as the  $R^2$  values representing the goodness of fit of the Gaussian + Linear functions to the sampled spectra are given in Table 3-1. For Tc-99m, it is apparent that the 95% confidence bounds of  $\sigma$ , and likewise the constants  $c_1$  and  $c_2$  described in equations 2-2 and 2-3, overlap for heads 2, 3 and 4.

For response to In-111 photons, heads 2 and 3 have similar energy resolutions, superior to the resolutions determined for heads 1 and 4. Due to the positioning of window  $Scat_{low}$ , the 171keV In-111 emission did not have any primary overlap with this window ( $\frac{Scat_{low}}{In-111} < 10^{-9}$ ).

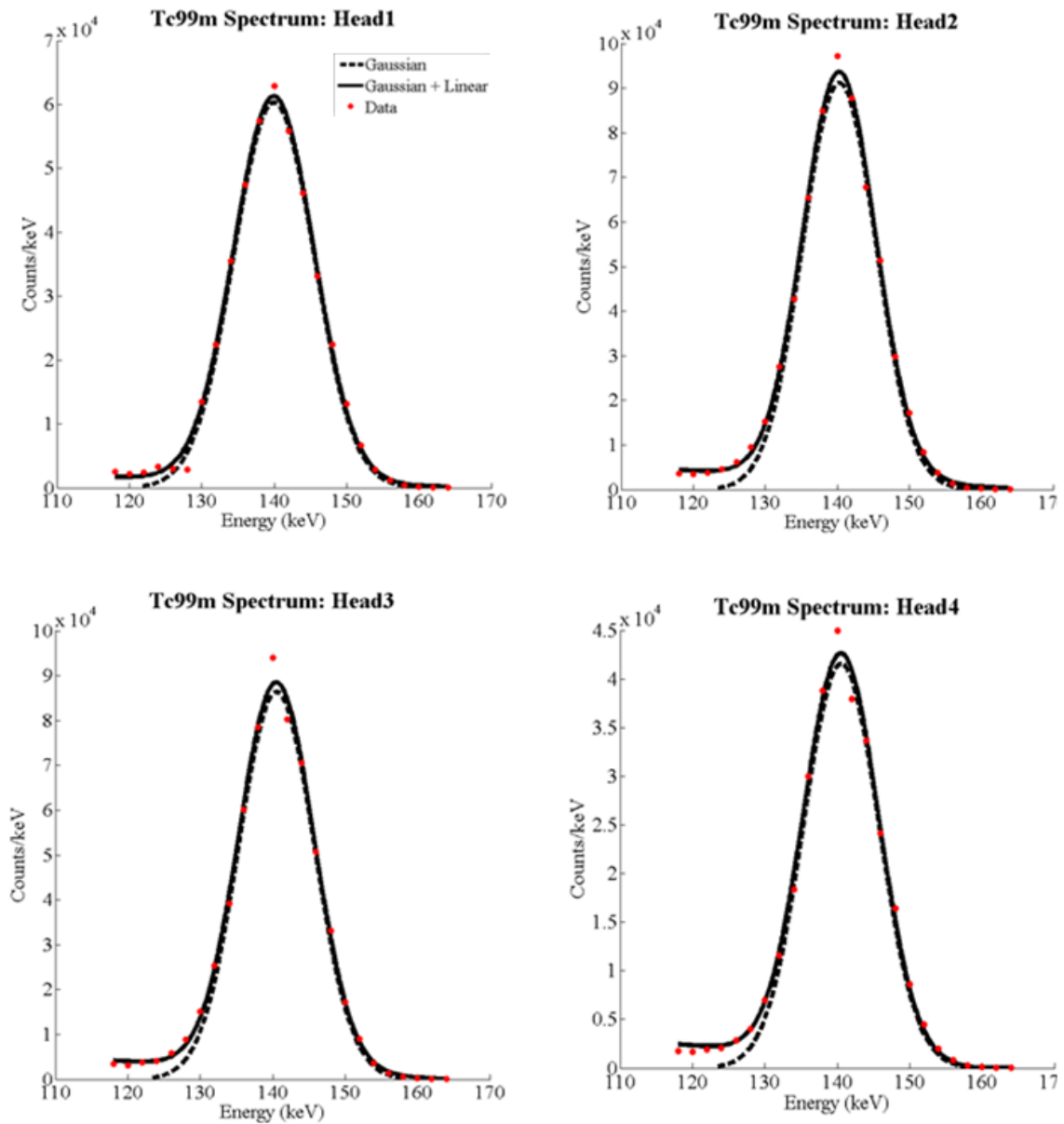


Figure 3-1: Energy spectra of the different camera heads in response to 140keV Tc99m photons. The red dots are the Counts/keV acquired in each bin, the solid black line is the result of the Gaussian + Linear fit of the spectrum, and the dashed black line is the Gaussian portion of the fit, which represents the scatter-subtracted energy spectrum.

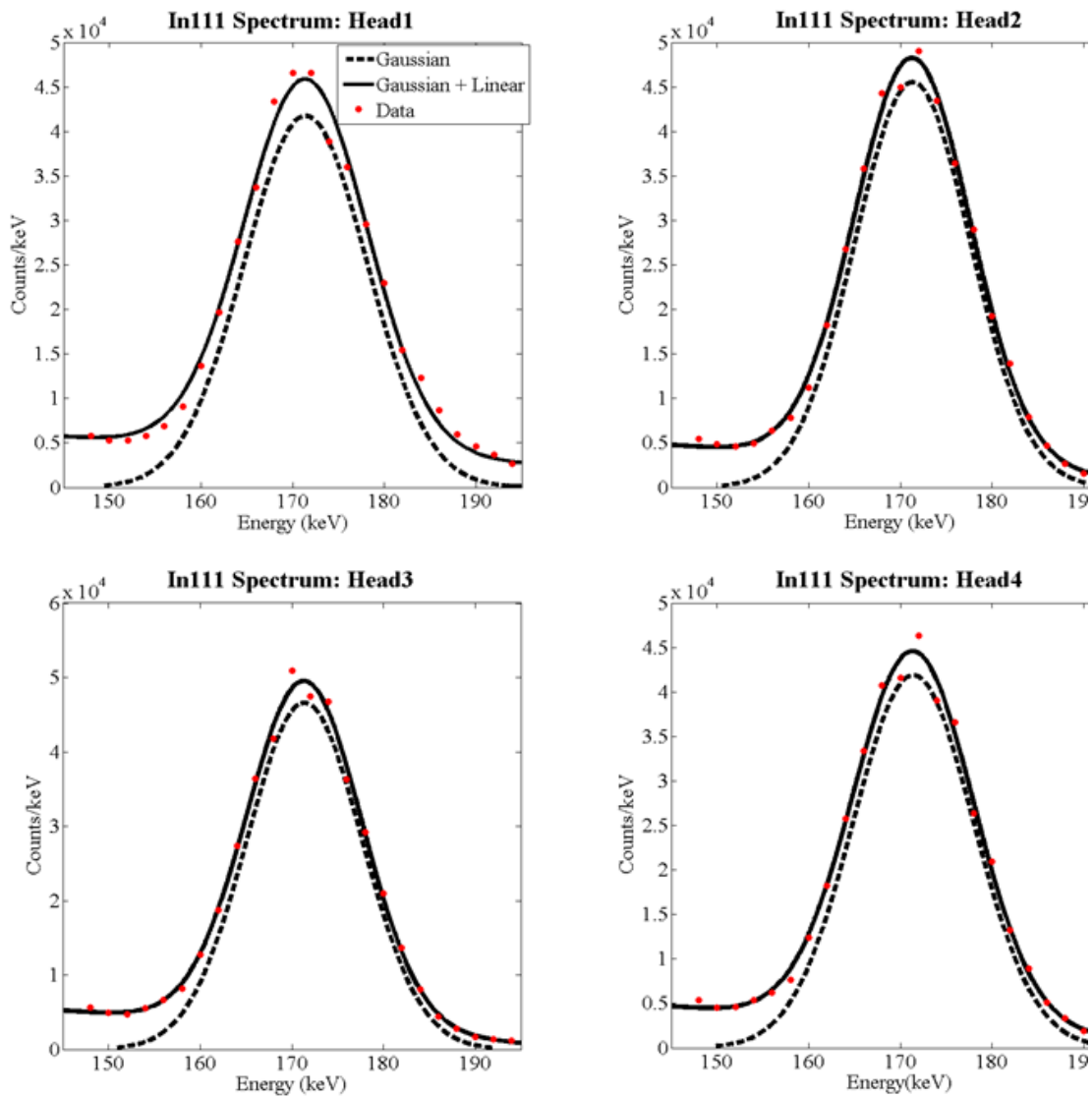


Figure 3-2: Energy spectra of the different camera heads in response to 171keV In-111 photons. The red dots are the Counts/keV acquired in each bin, the solid black line is the result of the Gaussian + Linear fit of the spectrum, and the dashed black line is the Gaussian portion of the fit, which represents the scatter-subtracted energy spectrum.

Table 3-1: Detector response to 140keV Tc-99m photons and 171keV In-111 photons.

<b>Detector response to 140keV Tc-99m photons</b>					
Head	$\sigma$ (keV) (95% conf. bounds)	FWHM (%)	$R^2$	$C_1$	$C_2$
1	5.5 (5.3, 5.7)	9.2	0.9922	0.0245	0.0334
2	5.0 (4.9, 5.2)	8.5	0.9981	0.0158	0.0225
3	5.2 (5.0, 5.3)	8.7	0.9967	0.0179	0.0252
4	5.1 (4.9, 5.4)	8.7	0.9954	0.0178	0.0251
<b>Detector response to 171keV In-111 photons</b>					
Head	$\sigma$ (keV) (95% conf. bounds)	FWHM (%)	$R^2$	$C_3$	
1	6.7 (6.3, 7.1)	9.2	0.9915	0.0111	
2	6.3 (6.1, 6.5)	8.6	0.9973	0.0082	
3	6.3 (6.1, 6.5)	8.6	0.9970	0.0082	
4	6.6 (6.3, 6.9)	9.1	0.9958	0.0103	

Comparing the energy resolution of each head to the Tc-99m resolution limit quoted by the nanoSPECT/CT manual (9.5%), heads 2, 3 and 4 had significantly better resolutions, while the quoted resolution limit was within the 95% confidence interval measured for head 1. The manual does not quote the energy resolution of the camera in response to 171keV In-111 photons.

The resulting well-counter calibration curve from the first of six sources is displayed in Figure 3-3. As can be seen, there is an excellent linear fit of the data in the range of count-rates examined ( $R^2 > 0.999$ ). The calibration factor for converting the count rate of the well counter to absolute Tc-99m activity was determined to be  $\kappa = (5.035 \pm 0.009) \times 10^{-7} \frac{\mu\text{Ci}}{\text{cpm}}$ . Here, uncertainty is the standard deviation of the mean slope value from the six sources.

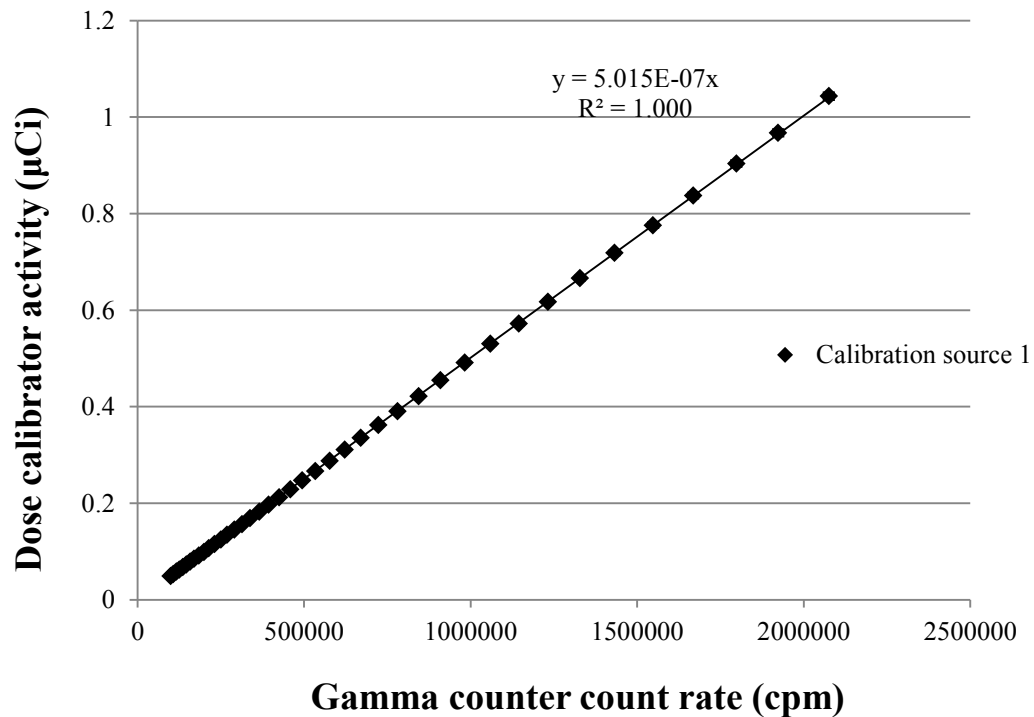


Figure 3-3: Calibration curve between gamma counter (cpm) and dose calibrator (μCi).

## 3.2 Phantom Validation

### Only In-111

The central coronal cross section of each resulting image is displayed in Figure 3-4. It is evident that the general In-111 distribution in the phantom—shown in Figure 3-4 (a)—can be inferred from the uncorrected scatter image in Figure 3-4 (b) due to cross-talk of In-111 photons in the Tc-99m energy window. Visually, the iterative TEW in Figure 3-4 (d) leaves less residual scatter than the modified TEW in Figure 3-4 (c), but does not perform as complete of a subtraction as the standard TEW in Figure 3-4 (e).

The cross-talk fraction in a given slice varied depending on the position in the container, as shown in Figure 3-5. In the image uncorrected for scatter, there existed a notable dependence of XTF on the spatial position within the phantom. The maximum XTF occurred near the center of the container, since the center of the container contained scattered photons originating from all directions. The different correction methods can therefore be assessed based on the curvature of the resulting cross-talk profile. Assuming that attenuation has been correctly accounted for, the best cross-talk correction method should result in a cross-talk fraction that is closest to 0, and does not vary with the depth of the phantom. Hence, the best cross-talk correction method should have the lowest remaining XTF with the minimum standard error.

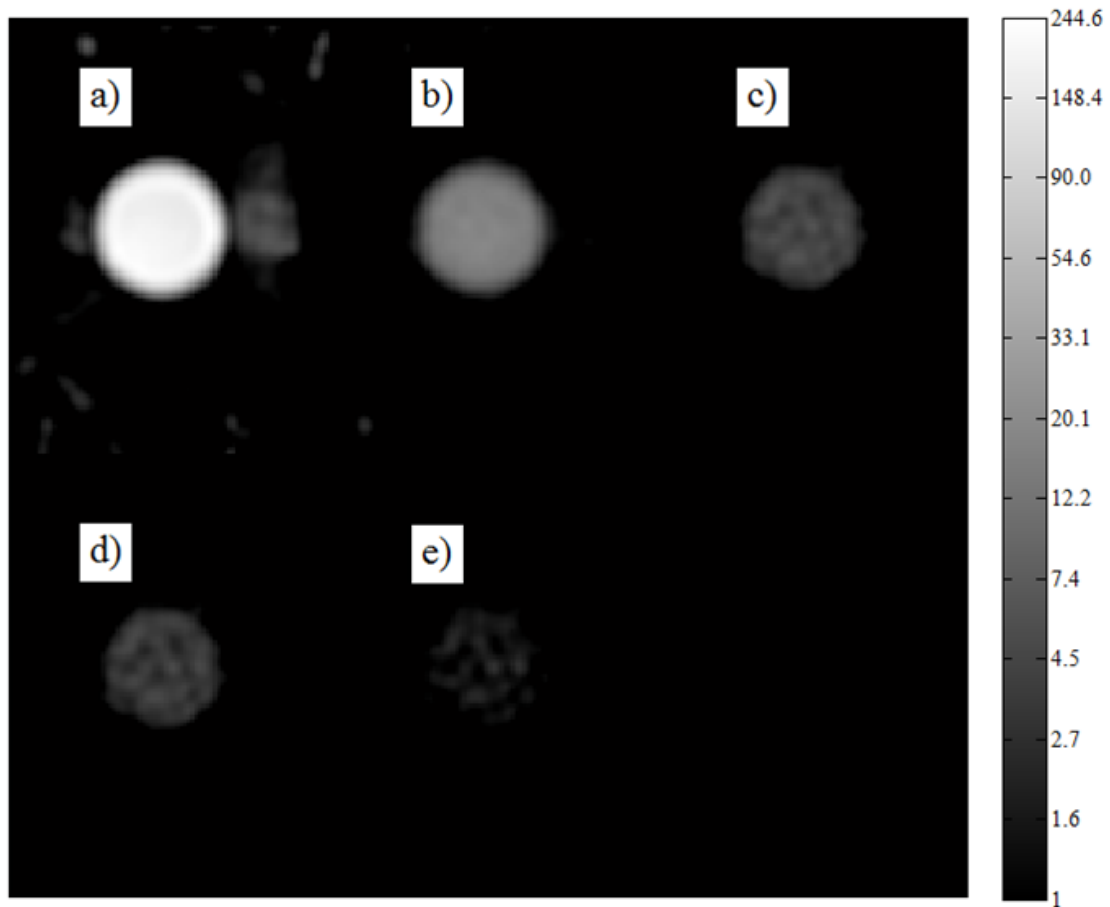


Figure 3-4: View of the central coronal slice of the plastic cylinder phantom containing only In111. (a) is the In111 window image, (b) is the uncorrected Tc99m image, (c) is the Tc99m image with modified TEW applied, (d) is the Tc99m image with iterative TEW applied, and (e) is the Tc99m image with standard TEW applied. The intensity values are transformed using the natural logarithm in order to view the full range of counts.

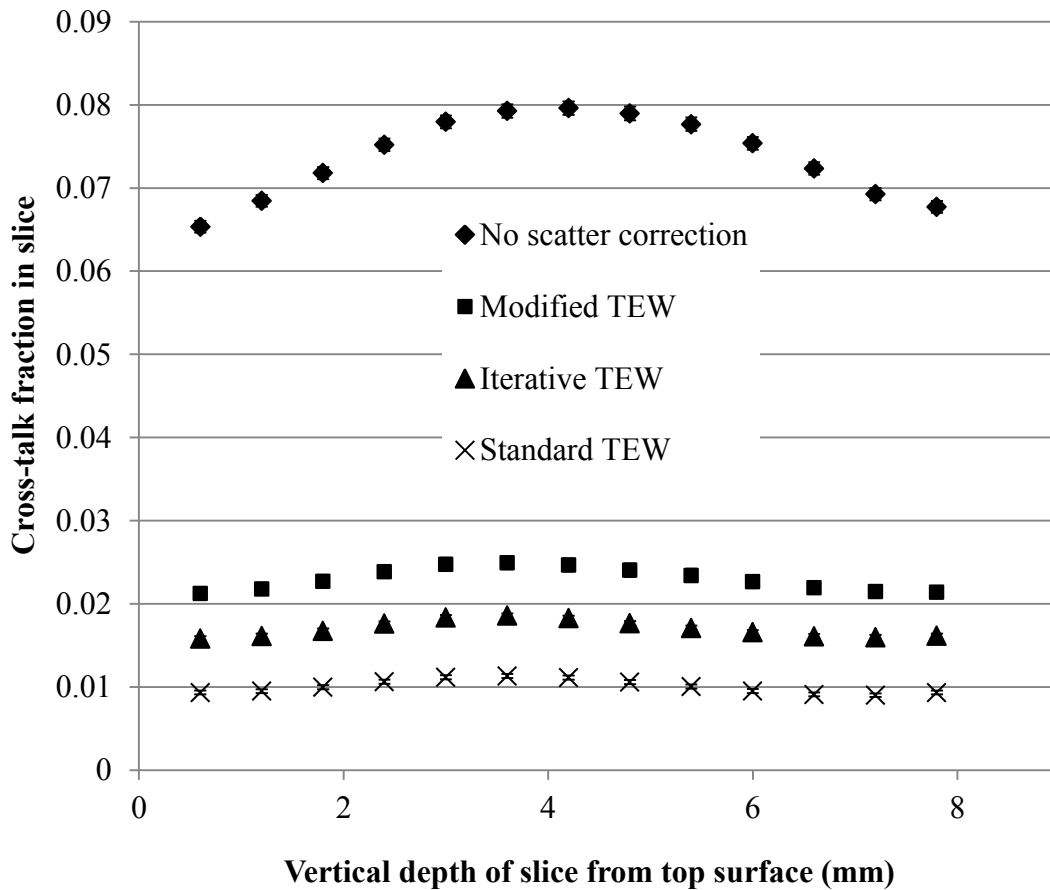


Figure 3-5: The amount of cross-talk present as a function of the depth from the top of the container. The left side represents slices selected at the top of the phantom, while the right sides of the curves represent slices selected at the bottom of the phantom.

The resulting cross-talk fractions, described as the mean XTF between slices of each image, are shown in Table 3-2. The error is the standard deviation of the mean XTF. In order to compare the different subtraction methods, paired t-tests were performed, assuming the XTF for each slice was an independent measurement.

Table 3-2: Cross-talk fractions with different corrections applied.

<b>Tc99m Scatter Correction</b>	<b>Cross-talk fraction (XTF)</b>
No scatter correction	$0.0738 \pm 0.0014$
Modified TEW	$0.0230 \pm 0.0004$
Iterative TEW	$0.0170 \pm 0.0003$
Standard TEW	$0.0101 \pm 0.0002$

The iterative TEW left significantly less cross-talk than the modified TEW ( $p < 0.001$ ), but was less effective than the standard TEW in the In-111 phantom ( $p < 0.001$ ). Using the F-test to compare the variance between the iterative TEW and modified TEW found no significance at a 95% confidence level. It is unsurprising that the standard TEW outperformed the other methods in the phantom of only In-111, since this method assumes—correctly, in this scenario—that there are no primary Tc-99m counts in the scatter windows. It is impossible to determine whether the standard TEW over-subtracted the scatter using the reconstructed image, since negative projection elements were set to 0 prior to reconstruction. In order to examine this properly, analysis was carried out in projection space.

The effect of negative projection elements resulting from noise in the subtraction of In-111 scattered photons in the Tc-99m image was substantial. Figure 3-6 shows that all three correction methods improve remarkably, independent of filtering, when the sums of projections are considered without truncating negative projections. It is apparent that with sufficient counting statistics by summing over projection space, the standard TEW

leaves a residual cross-talk fraction of 0.005, compared to a cross-talk fraction of 0.0738 without any correction.

However, the OSEM reconstruction cannot accept negative projections. After truncating, the residual cross-talk fraction jumps to 0.039, an 8-fold increase. Shown in Figure 3-6, pre-filtering the projections with a Gaussian low-pass filter as well as performing adaptive filtering on the negative projection elements improves the corrections, but is not able to spread the negative projections sufficiently to conserve total counts.

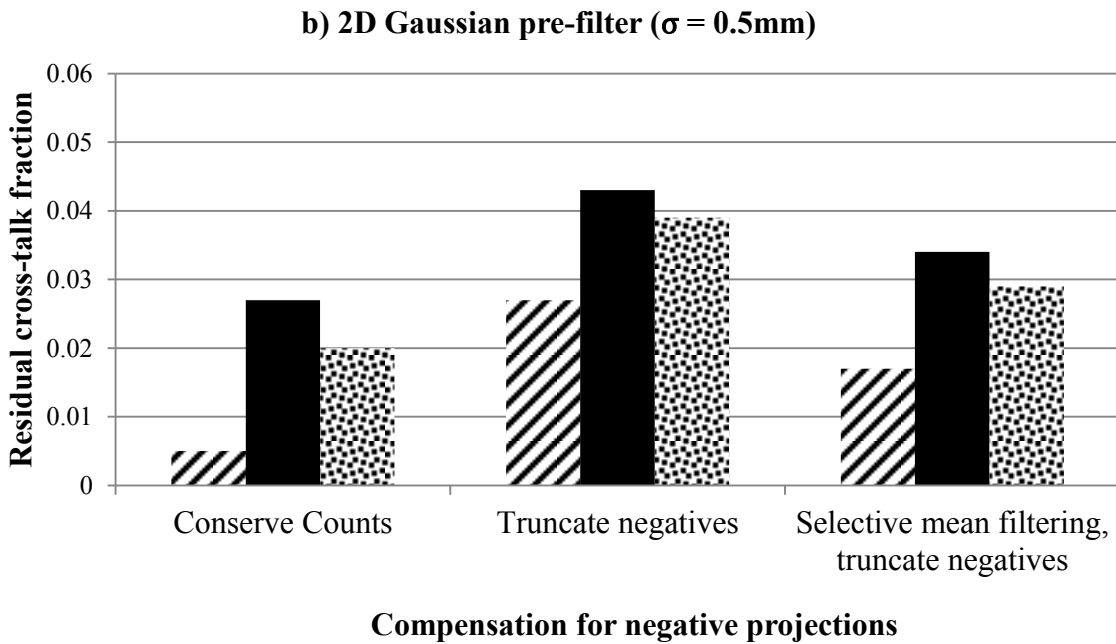
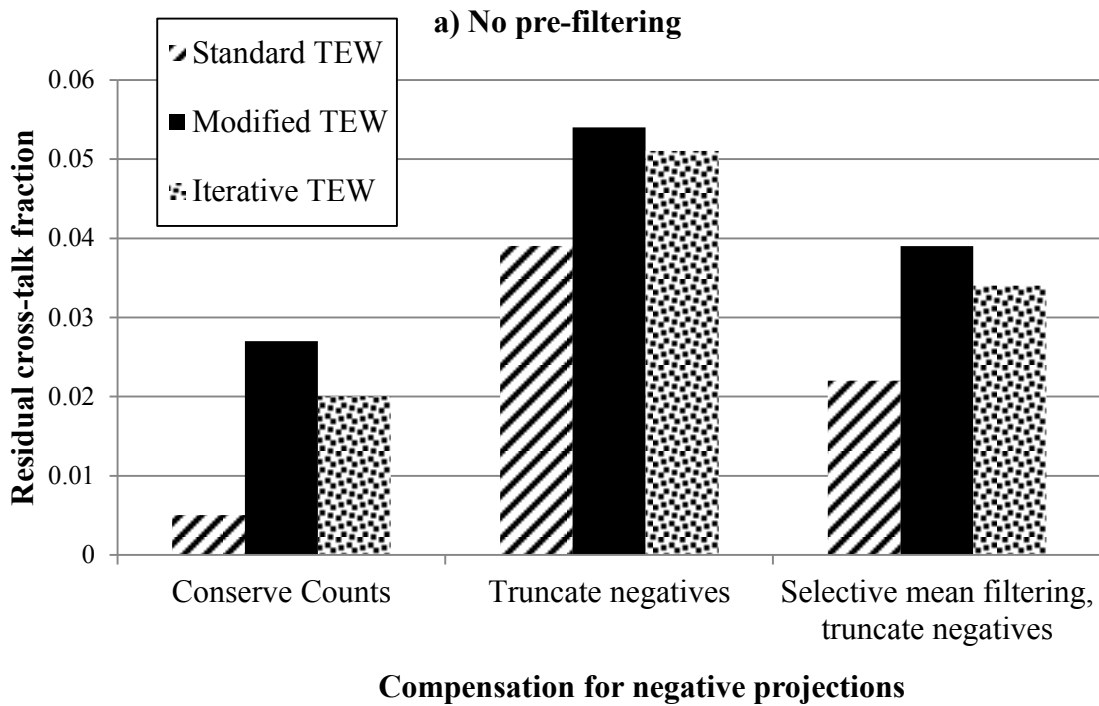


Figure 3-6: Comparison of the different correction methods in projection space. For each TEW-based method, the residual cross-talk fraction is determined after conserving counts, truncating negatives, and after doing selective mean filtering before truncating with projections a) not pre-filtered, and b) pre-filtered with a 2D Gaussian function ( $\sigma = 0.5\text{ mm}$ ). All errors are  $<0.0001$ .

As shown in Figure 3-7, the effect of filtering all raw projections with a 2-D Gaussian low-pass filter of increasing widths prior to the TEW scatter estimation was explored. The proportion of residual scatter was calculated as  $\frac{\sum Tc99m_{corrected}}{\sum Tc99m_{raw}}$  for the three different scatter correction algorithms under study. Negative projections were truncated before making the calculation.

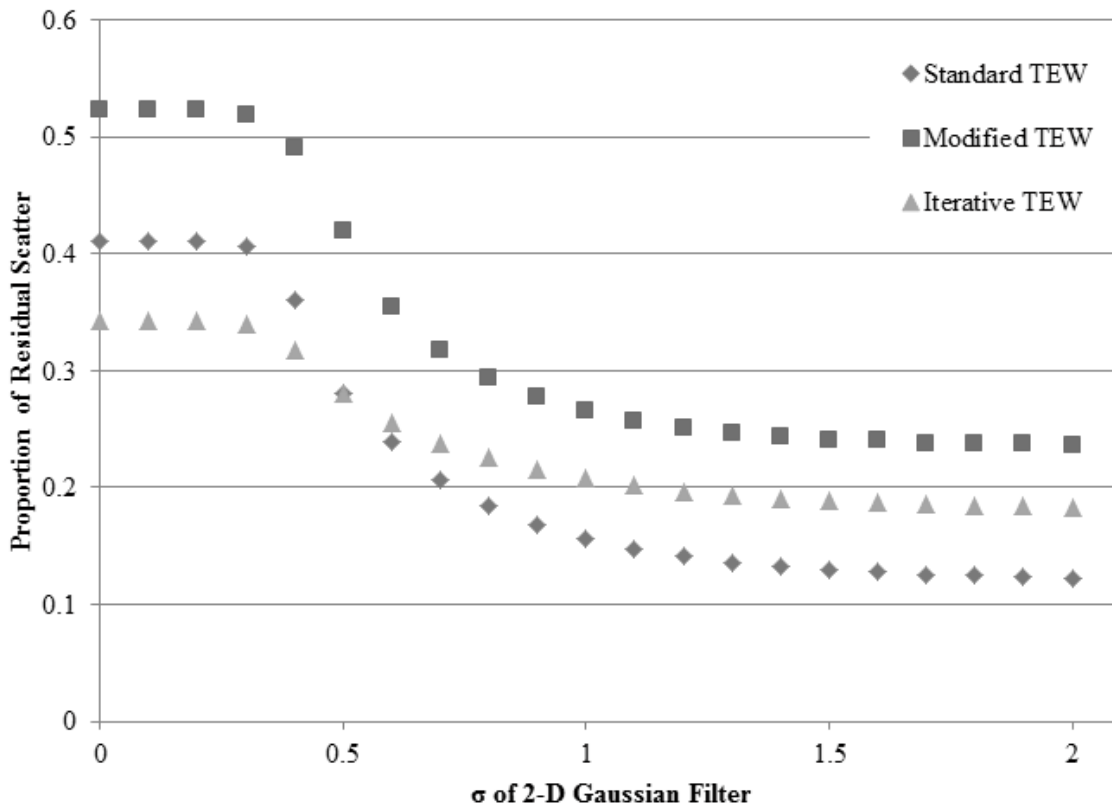


Figure 3-7: The effect of filtering projections analyzed in projection space. Error for all residual scatter measurements assuming Poisson counting statistics was < 0.001 and therefore error bars are too small to be seen in this figure.

It is evident that filtering the projections prior to making the scatter estimate results in less residual scatter. It was determined that a 2-D Gaussian pre-filter of  $\sigma = 1.0\text{mm}$  would be a good compromise between a decrease in spatial resolution and an

increase in the bias of the scatter estimate, since it minimizes residual scatter and minimizes the loss in spatial resolution inherent in low-pass filtering of the images.

The iterative TEW appears to be least sensitive to the change in pre-filtering. This is due to the fact that the iterative TEW approach includes using selective mean filtering of negative projection elements prior to the truncation of negative elements between iterations.

### **Mixed In-111 and Tc-99m Phantom**

Figure 3-8 shows the normalized activity recovery ( $\frac{A_{SPECT}}{A_{dose\ calibrator}}$ ) of the Tc-99m image without correction for cross-talk (solid line, square), with modified TEW scatter correction (dotted line, triangle), with iterative TEW scatter correction (dashed line, x), and with standard TEW scatter correction (dash-dot-dot line, diamond). Also included is the activity recovery of In-111 without correction for self-scatter (dash-dot line, circle). Error bars on this curve represent the variation of the mean voxel intensity value between slices, using a threshold of 40% of the maximum voxel intensity value of each slice to define the 2-D ROIs. Due to the partial volume effect, slices near the top and bottom of the phantom were avoided in these calculations. Propagated with this error is the error due to the dose calibrator measurement (assumed to be 2% of the measured value). This error was determined using the measurements described in section 2.2.1.

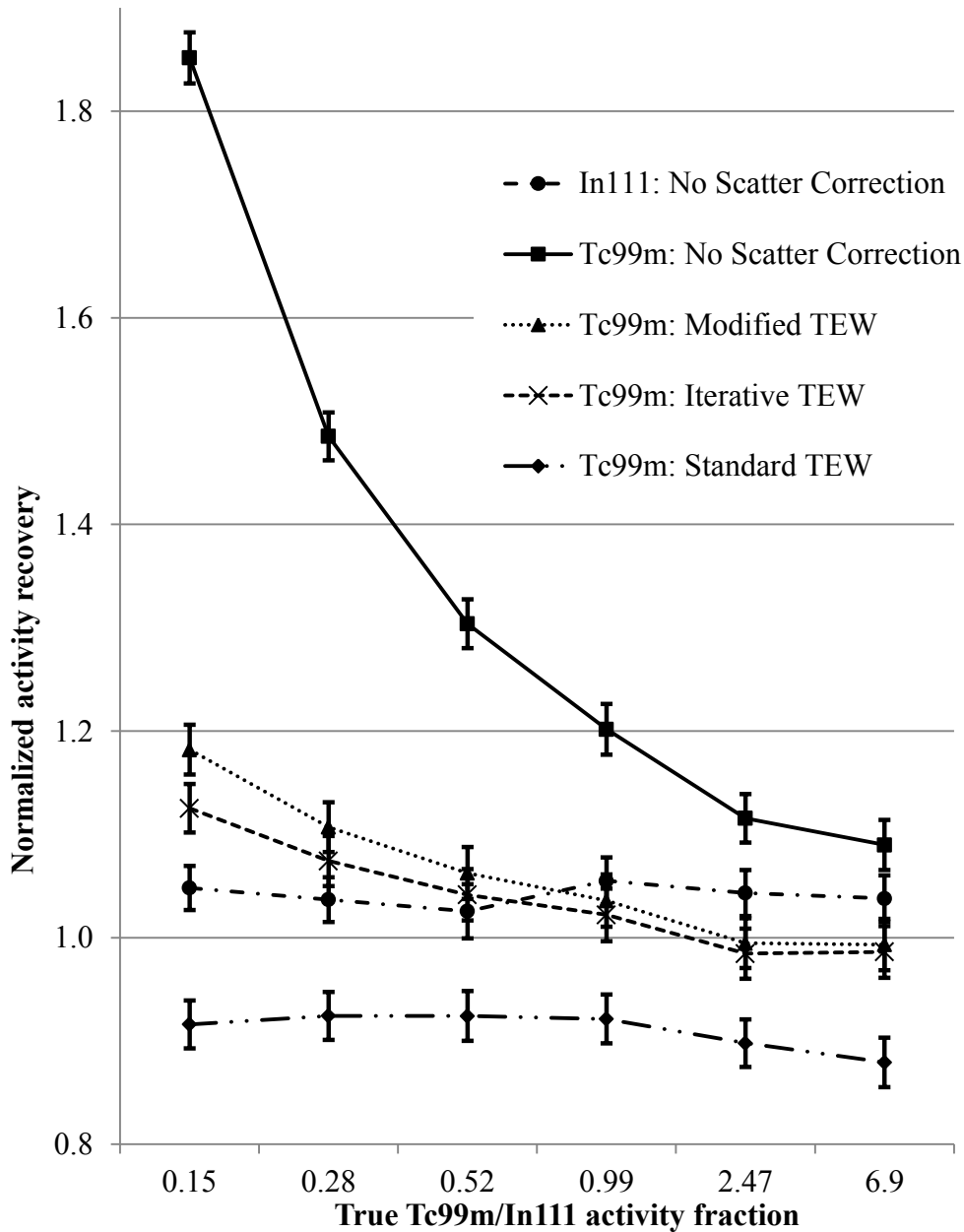


Figure 3-8: Quantitative results of the mixed Tc99m/In111 phantom experiment. Without correction for scatter, In-111 activity is overestimated by less than 5%, but is not dependent on the Tc-99m activity present. Without scatter correction, measured Tc-99m activity is dependent on the relative activity of In-111. Standard TEW consistently over-subtracts. Modified TEW and iterative TEW produce similar results if the Tc-99m/In-111 activity fraction is  $> 1$ . Iterative TEW is significantly more accurate in phantoms with activity fractions  $< 1$ .

Without correction for cross-talk, there was a 5% overestimation of Tc-99m activity in phantoms of mostly Tc-99m, but an 80% overestimation in phantoms with the lowest Tc-99m activity fraction.

The standard TEW, although demonstrating the best subtraction of scatter in the Tc-99m image in the pure In-111 phantom (Figure 3-5), consistently underestimated the Tc-99m activity across all activity fractions in the mixed-activity phantom experiment. This can be attributed to the presence of un-scattered Tc-99m counts and un-scattered In-111 photons in the scatter windows, biasing the standard TEW estimate. The modified TEW improved upon the standard TEW by accurately estimating the Tc-99m activity (within 5% of truth) in all phantoms with Tc-99m activity fractions greater than and including 0.99. Below this fractional Tc-99m activity, the modified TEW underestimated the cross-talk. As mentioned in section 1.9.4, this underestimate was probably caused by the assumption that the Tc-99m photo-peak window did not contain any scatter when determining the number of counts to subtract from the scatter windows.

The results of the paired t-tests, comparing the modified TEW and iterative TEW based on the magnitude and accuracy of the reconstructed images, are shown in Table 3-3. The iterative TEW always resulted in a significantly lower activity estimate than the modified TEW (95% confidence). The iterative TEW provided a significant improvement in accuracy compared to the modified TEW for phantoms with activity fractions below and including 0.52. In phantoms containing higher activity fractions, there was no significant difference between the accuracy of the modified TEW and iterative TEW activity estimates.

Table 3-3: Comparison of iterative TEW (ITER) to modified TEW (MOD) across the different activity fractions based on total activity and accuracy of activity estimate.

Activity Fraction ( $\frac{Tc-99m}{In-111}$ )	Is iterative TEW Tc-99m SPECT activity measurement significantly lower than modified TEW estimate (95% confidence)?	Is any correction significantly more accurate in returning activity concentration (95% confidence)?
0.15	YES	ITER
0.28	YES	ITER
0.52	YES	ITER
0.99	YES	NO
2.47	YES	NO
6.90	YES	NO

The mean In-111 normalized activity recovery estimation without correction for scatter was  $1.041 \pm 0.004$ .

As mentioned in section 2.2.4, large ROIs were selected in order to quantify the respective activities of both isotopes to avoid the partial volume effect. Since there was very little background (total counts outside the ROI used to make the SPECT activity measurement was always  $<0.5\%$  of the ROI=counts), it was safe to generate an ROI on the image that was a much larger cylinder concentric with the phantom.

In order to quantify the impact of PVE, the same plastic cylinder phantom experiment was used with known Tc-99m activity. Rather than creating a large, concentric ROI, however, the true volume containing activity was manually segmented in the CT image. Without accounting for partial volume effect, the normalized Tc-99m activity recovery of the iterative TEW was 0.85 in the 1:1 activity ratio phantom. Therefore, 15% of counts had spilled out of the phantom due to the limited system spatial resolution and the applied filtering. Using template-based PVEC resulted in an underestimation of the activity in the phantom of  $< 4\%$ .

### 3.3 *In Vivo* Validation

It is easy to see the degradation of the Tc-99m-tetrofosmin image after the injection of the In-111-liposome (Figure 3-9). One can also see the restored contrast between the myocardium and LV cavity due to the application of the modified TEW and iterative TEW. Although the iterative TEW subtracts significantly more scattered photons in the LV cavity, it is difficult to visually see this, as visually, the modified TEW also does a relatively good job in restoring image quality.

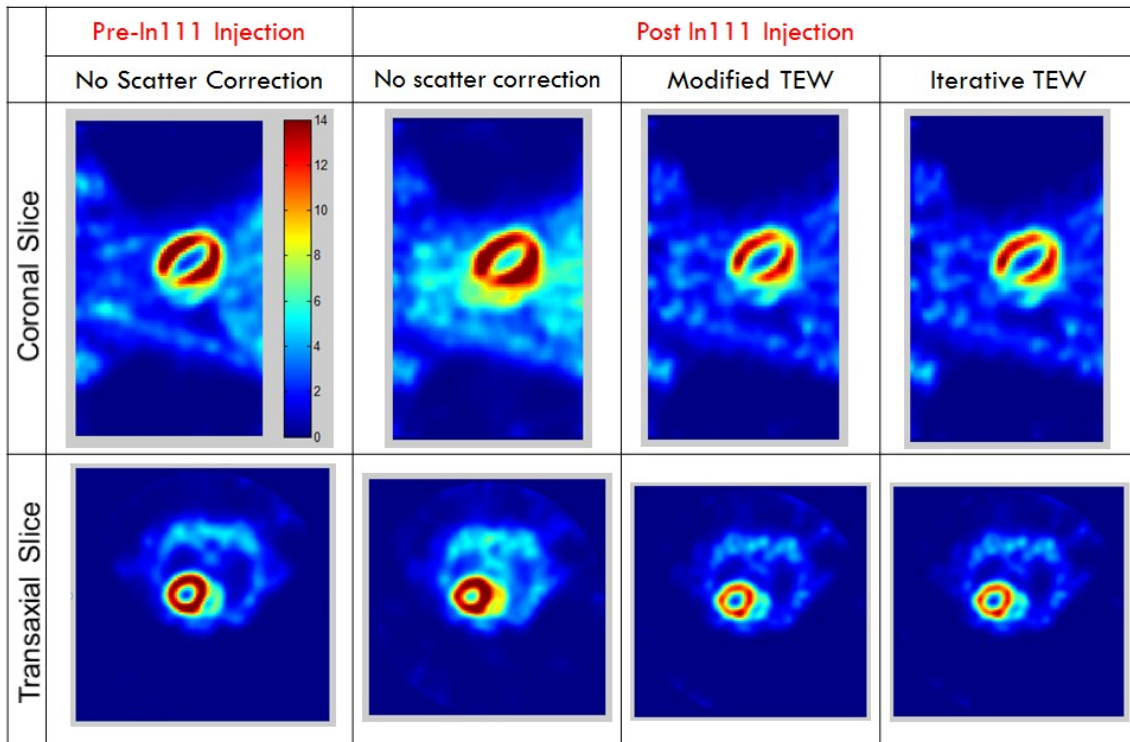


Figure 3-9: Central coronal and trans-axial slices of rat 1 images. The left images are uncorrected for scatter before the injection of In-111-liposome. The right side shows the reconstructed images after the injection of In-111 liposome uncorrected for scatter, with modified TEW scatter correction, and with iterative TEW scatter correction. The injection of In111 degrades contrast between the myocardia and heart chambers in the uncorrected Tc99m image. The modified TEW and iterative TEW visually restore the lost contrast.

The time activity curves (TACs) for the SPECT-estimated Tc-99m activity are shown in Figure 3-10. In the absence of In-111, one would expect an exponential decay of total heart activity with time due to physical decay and biological clearance. After In-111 was injected before scan 3, however, the increase in total heart activity in images uncorrected for scatter is clearly visible. The different scatter corrections removed this dramatic increase, restoring the exponential appearance expected.

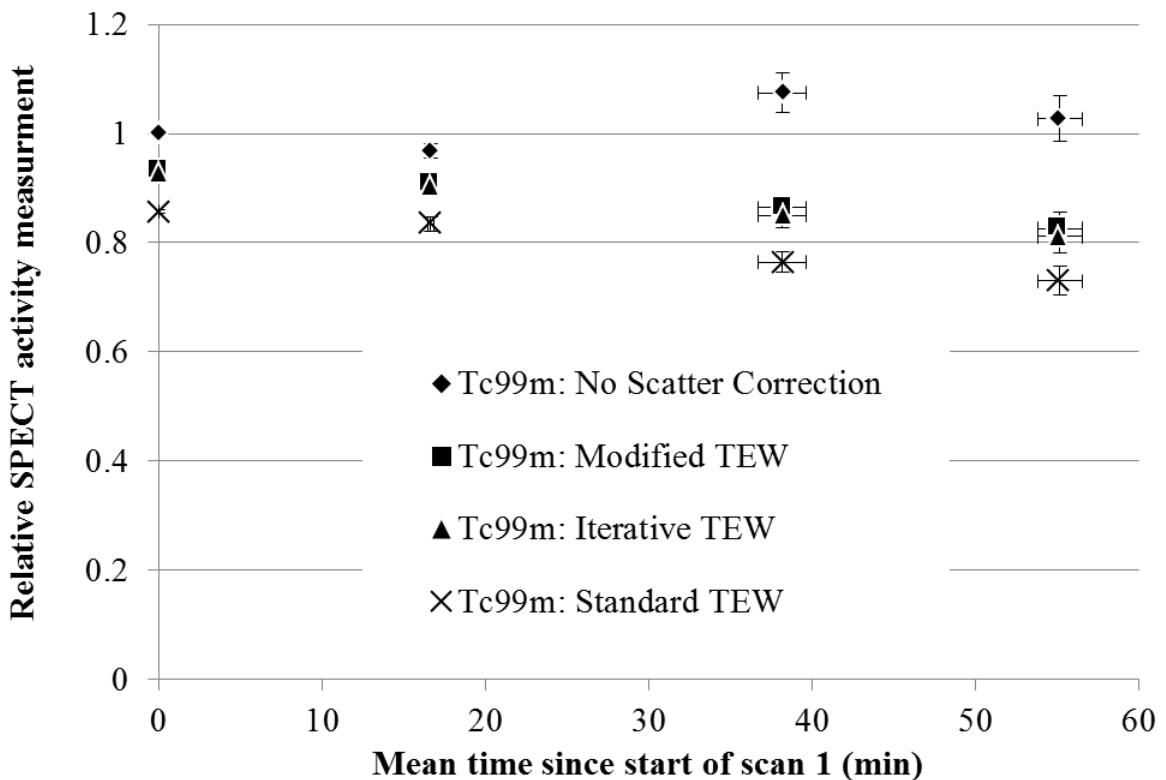


Figure 3-10: TACs for total-heart SPECT Tc99m activity, normalized to the total heart activity in the uncorrected images from scan1 for each rat. Vertical error bars represent standard deviation of the mean normalized activity between the 6 rats. Horizontal error bars represent the standard error on the time of each acquisition since the start of scan 1. Uncorrected for cross-talk, the uncorrected Tc-99m activity increased noticeably after the injection of In-111-liposome. Corrections for cross-talk all removed this increase, and restored the general exponential clearance.

The results of the well-counter curve-stripping (section 1.11.1.1) analysis for Rat 3 are presented in Figure 3-11. The time  $t=0$  refers to the time of the first well-counter measurement. The three separate curves represent the total count-rate model of the well counter (solid line), the In-111 count-rate model (dashed line), and the Tc-99m model (dot-dash line). The three sets of scattered data represent the total count rate measurements with only In-111 activity remaining (purple diamonds), the total count rate with both isotopes present (red circles), and the inferred Tc-99m count rate (Total data – In-111 cpm model). The In-111 and Tc-99m model curves were forced to have decay constants as defined in literature ( $T_{1/2}$  In-111 = 2.80days,  $T_{1/2}$  Tc-99m = 6.0 hours). Good agreement between the models and measured data points indicate that the true count-rate of Tc-99m at the time of the first measurement is known with little uncertainty.

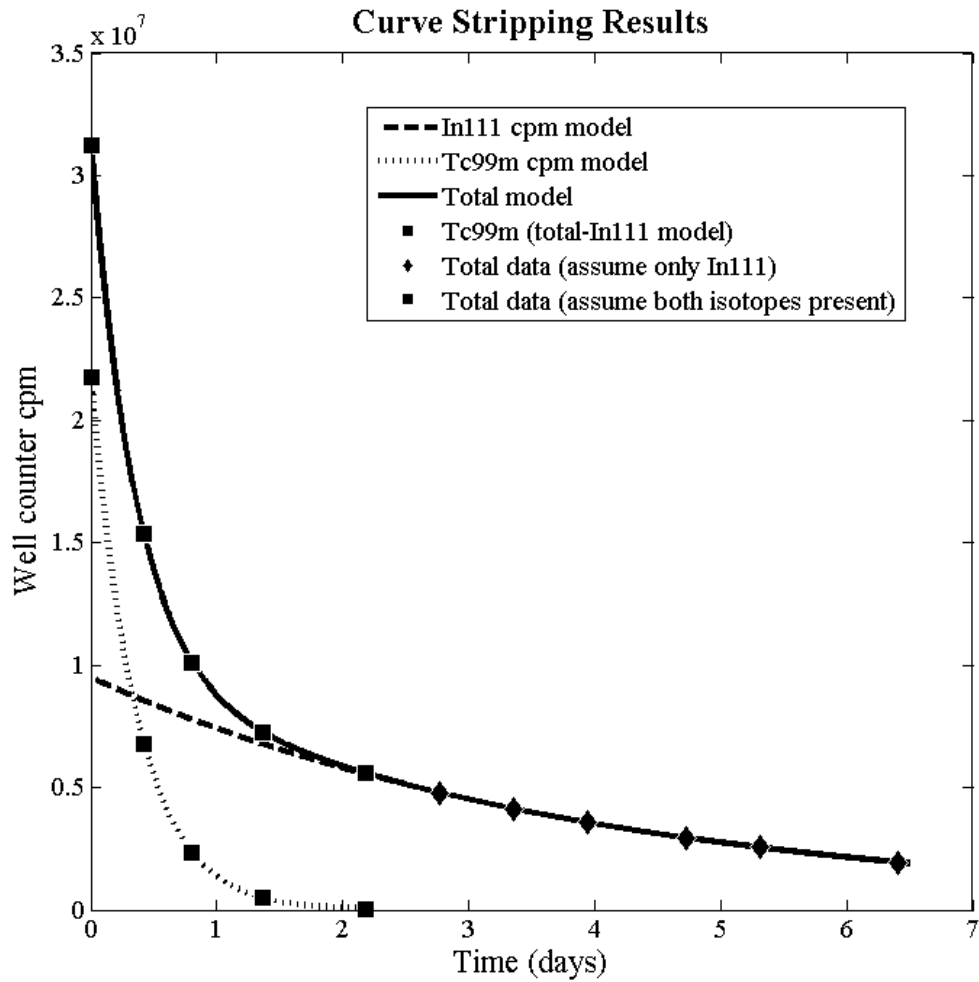


Figure 3-11: Curve stripping used to delineate Tc99m activity from In111 activity. Error bars representing Poisson noise in counting and summing 40 samples for each data point are too small to be seen. Beyond day 2, it is assumed that only In-111 activity is present (diamonds). The data in this time-range is used to model the In-111 count-rate present between day 0 and day 2 (dashed line). Tc-99m count-rate (dots) is determined by subtracting the In-111 model from the measured total count-rate (squares).

The results of the planar acquisition to determine the Tc-99m activity lost to the tools during the sectioning of the heart are shown in Figure 3-12. Error bars represent the propagation of counting errors onto the calculations assuming Poisson counting statistics for the total counts accumulated in each window. In the far right set of data, the modified TEW was applied to the Tc-99m window counts using the total sum of all counts acquired in the scatter windows, In-111 window, and Tc-99m window. The modified TEW was used to reduce the influence of In-111 scattered photons on the calculation of fractional Tc-99m activity retained in the sample containers after physically sectioning the heart into 40 pieces.

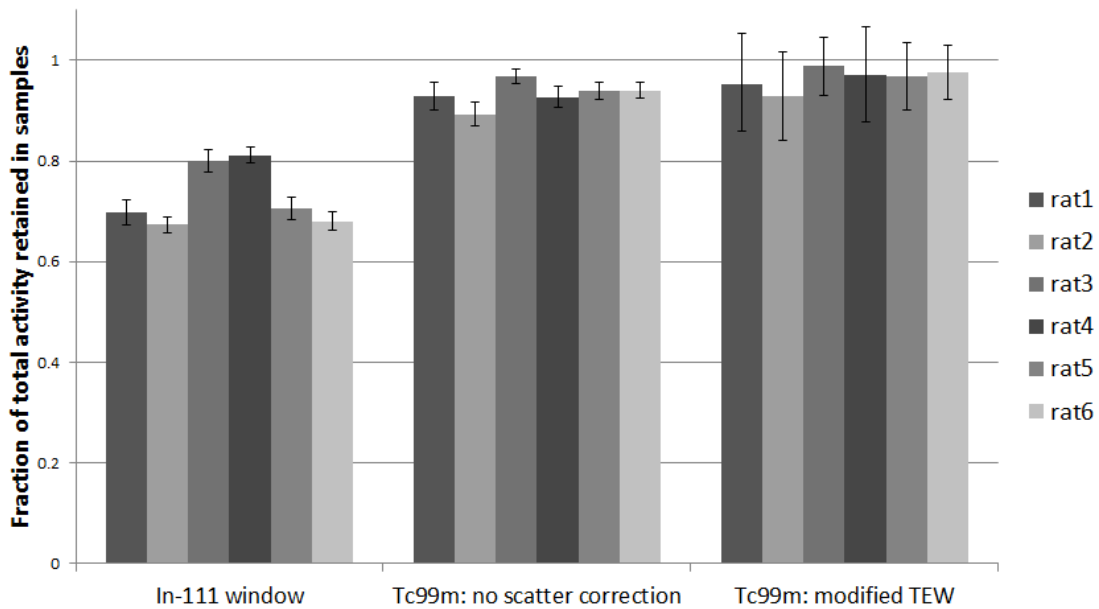


Figure 3-12: Fraction of counts retained in samples based on the planar gamma camera acquisitions. The modified TEW results (right hand side) were used to determine the fraction of total activity that was retained in the samples after physically sectioning each of the hearts into 40 pieces.

The fractional activity retained in the samples, as well as the gold-standard activity estimations, decay corrected to the time corresponding to the beginning of the final SPECT acquisition, are given in Table 3-4.

Table 3-4: Fractional activity present in samples, as well as gold standard activities for each rat, decay corrected to the beginning of the 4<sup>th</sup> helical SPECT acquisition. The asterisk represents the larger uncertainty present in rat 4 gold standard activity measurement due to one of the samples being counted outside of the linear range of the well-counter.

<b>Rat#</b>	<b>F<sub>samples</sub></b>	<b>Gold Standard Tc-99m Activity (μCi)</b>
1	0.952	22.2
2	0.928	21.7
3	0.988	52.6
4	0.971	25.0*
5	0.968	36.8
6	0.976	34.9
Mean	0.964 ±0.009	33±6

The normalized activity recoveries for individual rats in the images containing the different corrections for cross-talk are summarized in Table 3-5. PVEC increased the SPECT activity estimate by an average factor of  $1.32 \pm 0.01$ . A paired t-test shows that iterative TEW activity estimation was significantly lower than modified TEW ( $p < 0.01$ ), but there was no significant difference between the accuracies of the two methods.

Table 3-5: Normalized activity recovery for total-heat activity compared against the well-counter measurements.

<b>Rat #</b>	<b>No Scatter Correction</b>	<b>Standard TEW</b>	<b>Modified TEW</b>	<b>Iterative TEW</b>
1	1.31	0.89	1.01	0.99
2	1.42	0.90	1.05	1.02
3	1.14	0.85	0.95	0.94
4	1.17	0.81	0.93	0.91
5	1.17	0.80	0.98	0.96
6	1.20	0.88	0.98	0.97
<b>Mean</b>	<b>1.24 ± 0.04</b>	<b>0.855 ± 0.017</b>	<b>0.983 ± 0.017</b>	<b>0.965 ± 0.016</b>

The different TEW-based methods were compared based on their ability to remove cross-talk of In-111 scattered photons in the Tc-99m window in the area of the LV cavity in Table 3-6. The results are presented as the mean proportion of residual scatter between the different rats, with the error being the standard deviation of the means over the set of 6 animals. Paired t-tests performed indicate that the iterative TEW left significantly less scatter than the modified TEW ( $p < 0.001$ ) and the standard TEW left significantly less scatter than the iterative TEW ( $p < 0.001$ ).

Table 3-6: Residual scatter left in the LV cavity by three different scatter-subtracted images: modified TEW, iterative TEW, and standard TEW.

<b>Scatter Correction Method</b>	<b>Mean Proportion of Residual Scatter <math>\frac{C_{sc}}{C_{uncorrected}}</math></b>
<b>Modified TEW</b>	0.53 ± 0.03
<b>Iterative TEW</b>	0.49 ± 0.03
<b>Standard TEW</b>	0.39 ± 0.03

According to the results in Table 3-6, one might conclude that none of the scatter-correction methods performed very well in removing In-111 cross-talk in the Tc-99m

image in the region of the LV cavity. However, PVE may be to blame here. Despite the fact that attempts were made to avoid including counts close to the myocardium in the calculation, it is very possible that Tc-99m counts from the myocardium could have spilled into the ROI specifying the LV cavity.

# 4 Discussion

In dual isotope Tc-99m and In-111 SPECT, cross-talk caused by scattered In-111 photons detected with energies within the Tc-99m window cause an overestimate of Tc-99m activity. The iterative TEW correction for cross talk provided comparable quantification accuracy to the modified TEW in regions with similar activities of In-111 and Tc-99m, achieving our goal of accuracy within 5% of truth for activity ratios ranging from 0.52 to 6.90. The iterative TEW method improved on the modified TEW method by providing significantly superior accuracy in regions of mostly In-111 in phantoms and *in vivo* in rats. These results support the use of Iterative TEW for quantitative dual-isotope SPECT imaging. There are, nevertheless, certain limitations to the validation experiments that we would like to discuss.

Although I acquired sufficient counts to have <0.5% error due to Poisson counting statistics at the peak of each spectrum, the error may have still been significant in the less probable portions of the spectra. Looking back at Figure 3-1 and Figure 3-2, at the edges of the peak, the Tc-99m and In-111 acquisitions had bins of approximately 2000 and 5000 counts, with error of 1.5% and 2%, respectively.

Curiously, the fitted curves provided a good representation of the sampled Tc-99m spectra, except at the peak, where it was underestimated. This could be due to the energy calibration of the detector, or a rise in scatter at this range in energy. This fitting method, just as the TEW, assumes that scatter within the photo-peak is a linear function. This may

not be a perfect representation of reality, and may thus contribute to the observed discrepancy.

The fits of the In-111 spectra were worse than those for Tc-99m. This is most likely due to the more complicated scatter scenario that exists with the 171keV In-111 peak. The sampled spectra contain scattered photons that originated from the 245keV In-111 emission as well as self-scatter from the 171keV emission, although a small 100 $\mu$ L source was used in an attempt minimize this contribution. For heads 2-4, there appear to be very few 245keV scatter counts to the right of the 171keV peak. For head 1, just as with Tc-99m, the fit to the In-111 spectrum had the lowest r-squared value. It also had higher count-rates in the energy range above the 171keV In-111 peak. When acquiring the counts for all heads, the geometry was exactly the same. This discrepancy might be caused by more Compton scatter events occurring in the scintillation crystal, or simply be a problem related to the worse energy resolution and energy uniformity of this camera head.

Another possible source of error could be that the bin sizes were not exactly the same for each data point. The camera does not allow the user to specify energy windows of absolute sizes. The user defines an energy window by choosing the centroid energy and the width (expressed as a percentage of centroid energy). The problem with this setup is that the percentage can only be expressed as a positive integer (ex: 1%, 2%, 3%, etc.). Thus, I kept the bin width at 1% for my acquisitions and incremented the centroid energy by 2keV in between acquisitions. In order to account for the variation in bin size, each sampled count-rate was normalized to the bin-width. This assumes that the function was linear within the bin, which is not entirely true. In order to analyze the error in making

this assumption, the resulting Gaussian + Linear function from the fit was integrated across the true bin size and compared to the assumption that the spectrum was linear within the bin. This error was at a maximum of 1% at the peak of the spectrum, and over the scatter windows it was on the order of 0.1%. Compared to the error of the important parameters due to the fitting procedure, this is low, and assumed not to play an appreciable role in our scatter estimates.

In order to calibrate the reconstructed SPECT counts into absolute activity, we were unable to create a scenario in the camera with no scatter and no attenuation. The camera did not allow an acquisition without the rat bed in the FOV, and we were thus left with some attenuation and scatter in our image. The attenuation correction used has been shown to work well [30], but the scatter correction used (iterative TEW) is the same correction being evaluated in this work. It subtracted 4% of total counts from the calibration source, but we have no other independent measurement as a basis for comparison.

In the phantom containing only In-111 activity, it is curious that the standard TEW, without truncating negative projection elements, still leaves some residual scatter in the projections (Figure 3-6). This goes against the hypothesis that the standard TEW overestimates the scatter in all scenarios due to the presence of un-scattered In-111 and/or Tc-99m photons being detected in the scatter windows. This may be explained by the fact that the fundamental assumption of the TEW—that the scatter profile is linear between the scatter windows—may not be a perfect assumption. If the scatter was more complex, such as is shown in Figure 4-1, this could be what creates the under-estimate of scatter in the only In-111 phantom. The situation similar to what is shown in Figure 4-1 may arise

if the Compton edge from the In-111 exists within the Tc-99m primary window. In such a scenario, the presence of the In-111 primary counts actually creates a positive bias in the standard TEW scatter estimate, making it closer to the truth.

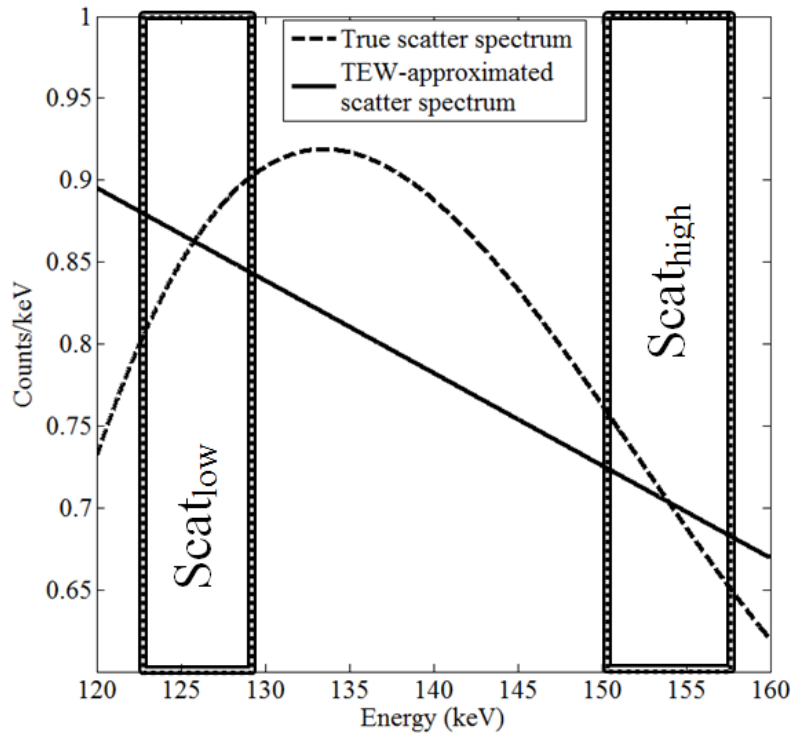


Figure 4-1: Depiction of a scatter spectrum that would result in a TEW under-correction due to the non-ideal assumption that the scatter profile (dashed line) between the scatter windows (boxes) is linear (solid line).

Error for the mixed phantom experiments was determined using the propagation of SPECT error and dose calibrator error in the normalized activity recovery calculation. SPECT error was determined as the variation of the mean voxel intensity value between slices, using a threshold of 40% of the maximum voxel intensity value of each slice to define the 2-D ROIs. The dose calibrator error used was 2% of the activity measurement. This represents the uncertainty in the activity measurement due to the geometry of the

source in the dose calibrator, as well as the variation of dose calibrator sensitivity with position.

In order to determine the efficacy of this error assumption, five phantoms with a  $\frac{Tc99m}{In111}$  fraction of  $\sim 1.0$  were developed and the statistical fluctuation of the normalized Tc-99m activity recovery estimate was analyzed. The standard deviation of the mean normalized activity recovery between the five phantoms was found to be within approximately 10% of that calculated by the slice-by-slice method (section 0).

The loss of effectiveness in both the modified TEW and iterative TEW in phantoms containing mostly In-111 might be attributable to incorrect parameters used to determine the fraction of un-scattered In-111 photons that are detected in  $Scat_{high}$ . Therefore, the sensitivity of the scatter estimate to the value of  $\epsilon$  in equation 2-4 was analyzed in the phantom containing mostly In-111 ( $\frac{Tc99m}{In111}$  activity fraction = 0.15) by varying it between 0 and 1 in projection space prior to reconstruction. Each data point represents the normalized Tc-99m activity recovery in the reconstructed image. The most important range of  $\epsilon$  is [0.45, 0.55], as this is the reasonable range of possible values that  $\epsilon$  might take. This is shown in Figure 4-2.

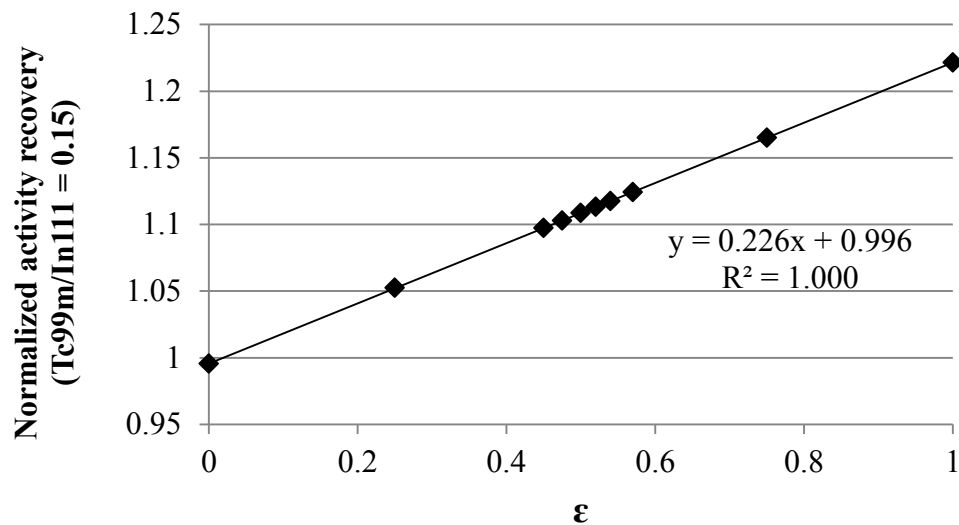


Figure 4-2: Determining the sensitivity of the normalized activity recovery to  $\epsilon$ , the scaling of the estimated proportion of In-111 primary counts appearing in  $\text{Scat}_{\text{high}}$ .

The result is a linear dependence on the normalized activity recovery with  $\epsilon$ . This means, with the slope of the curve being 0.226, if  $\epsilon$  is off by 0.1 in this phantom, the error in the resulting activity will be 2.26%. A normalized activity recovery of 1 would only occur if  $\epsilon \rightarrow 0$ . Values of  $\epsilon$  close to 0 are not practical, since I have shown in the calibration of parameters section (section 3.1) that there is a non-negligible component in the  $\text{Scat}_{\text{high}}$  energy window that comes from the 171keV In-111 un-scattered emission. The loss of effectiveness most likely does not result in the Tc-99m overlap factors either, since both the iterative TEW and modified TEW are effective in phantoms of only Tc-99m.

The Gaussian overlap factors are sensitive to the energy window sizes and positions. Consequently, if the camera is not peaked properly, the resulting Gaussian energy spectrum may shift by 2-3keV in either direction. This would degrade the

accuracy of the modified TEW and iterative TEW methods and may contribute to the error that is most prominent in phantoms with high ratios of In-111.

Despite their limitations, the modified TEW and iterative TEW were both accurate (within 5% of truth) in phantoms containing mostly Tc-99m and comparable activity concentrations of both isotopes. For many *in vivo* applications, the limitations of the scatter correction methods may not be apparent.

In determining the gold standard total heart activity using curve-stripping of the well-counter curves (rat 3 shown in Figure 3-11), all of the curves had small uncertainty except for rat 4. The Tc-99m model did not match very well with the data, and the measured decay constant of Tc-99m varied depending on the time selected for assuming only In-111. As a result, there was much more uncertainty in the gold standard measurement for rat 4. Further analysis lead to a variation of approximately 1-2 $\mu$ Ci (~3-6%). Upon closer examination of the well-counter outputs, 1 out of the 40 samples for rat4 had a much higher activity than the others (count rate > 5Mcpm). Since important well-counter measurements were performed at a count-rate where noticeable dead-time effects were present, this most likely explains the discrepancy.

The rat experiments were done in sets of 2, and each set of rats had the same age, but it varied between sets due to camera difficulties between experiments. The asterisk next to the gold standard total heart activity measurement for rat 4 (Table 3-4) represents the large degree of uncertainty for the gold standard activity estimate for rat 4 due to pulse-pileup present in 1 out of the 40 samples. The asterisk is also present because the injection of Tc-99m into the tail vein of rat4 was interstitial, and therefore a large amount of activity was not injected directly into the blood supply. Consequently, one should not

expect the total heart activity uptake of rat 4 to be similar to that of rat 3, even though they were similar in age and size at the time of acquisition. One should also expect there to be more of a discrepancy in the normalized activity recovery for this rat due to the well-counter uncertainty. Removing rat 4 from the sample resulted in improvements in normalized activity recovery by approximately 1% for all 3 cross-talk correction methods.

Many steps were involved, each with quite noticeable levels of uncertainty and error, in determining the normalized activity recovery of the rats. In determining the gold standard activity, the largest source of error was probably in determining the fractional Tc-99m activity retained in the samples after cutting the heart into 40 pieces ( $F_{\text{samples}}$ ). Between rats, this ranged between 0.93 and 0.99. In order to avoid cross-talk affecting this calculation, the modified TEW was applied, using the sum of counts in each window to determine the estimate of total scatter. This was done to avoid errors due to low counting statistics that would have been prevalent if a pixel-by-pixel subtraction was done. Since spatial information was not required here, this method worked well.

It is somewhat of a circular argument to use the modified TEW as part of the process in developing the gold standard to test the modified TEW. We would have liked to use the In-111 window information to determine  $F_{\text{samples}}$ ; however, the In-111 information gave us significantly different results. There was much more In-111 activity lost to the tools compared to Tc-99m. This is probably due to the nature of the molecules that the tracers were bound to. Tc-99m-tetrofosmin binds to the heart muscle tissue, and probably did not easily stick to the tools. In-111-liposome stays with the blood, and blood clotted to the tools and cutting-board. In order to avoid this problem, it may have been

possible to wash the tools and cutting-board with paper towel and count the paper towel in the well-counter, just as we had done with the true heart samples. This way, we could have been confident that all of the activity retained in the samples, eliminating a source of error from the experiment.

The *in vivo* SPECT activity measurements carry their own sources of error due to limitations in segmentation as well as limitations in corrections for attenuation, scatter, and PVE. The PVEC used in the plastic cylinder phantom underestimated by 4% the SPECT activity determined using a large ROI, so there may also be such a discrepancy with the rats. *In vivo*, PVEC and segmentation were done using a unique template for each rat, based on the iterative TEW image. This created a bias, as different images may have different recovery coefficients, or lead to a bias in the manual segmentation process.

The cross-talk correction may have under-corrected for scatter, and this error could have been hidden by insufficient correction for spill-out (PVEC) of Tc-99m myocardia activity. This is a comparable situation to when one reconstructs an image without correction for attenuation or scatter. The apparent activity recovery of an uncorrected image is higher than what it should be, due to the presence of scattered counts. For example, in mouse-sized-phantom Monte-Carlo simulations, without including scatter, quantification accuracy was degraded by -18% with Tc-99m. The inclusion of scatter effects into the simulation improved the accuracy to -12% [27]. In this case, the two image-degrading processes just happen to work in opposite directions.

Using the same reconstruction and attenuation correction software along with the DEW for scatter correction but without PVEC, Strydhorst was able to get the Tc-99m-

tetrofosmin SPECT reconstructed image of the rat myocardia to agree with the well-counter measurements within error. However, he notes that the ROI used was a cylindrical volume placed over the heart region and it may have contained activity external to the myocardium [30]. Therefore, it is difficult to use this as a basis for comparison.

The effectiveness of the TEW-based corrections depends on the position of the two scatter windows ( $Scat_{low}$  and  $Scat_{high}$ ) relative to the emission energies of the isotopes. In our study, the Tc-99m primary and scatter windows were chosen similar to the windows optimized for a planar SPECT Tc-99m/In-111 study [44].

The difference is that we used a single window for In-111, since our camera was limited to four total windows per acquisition. This did not limit the effectiveness of In-111 quantification in phantoms, as there was approximately a 4-5% overestimation in activity due to scatter in this geometry. The amount of scatter present in the In-111 window may be much higher in an *in vivo* scenario, but the accuracy of the In-111 image was not analyzed in the rats. Ideally, separate windows would be used to cover each In-111 emission (171keV, 245keV). In our study, the use of a large window with a width of ~100keV resulted in the inclusion of more scattered counts (from the 245keV In-111 emission) in the parts of the spectrum between the two emissions. If we were not limited to 4 windows, it would be best to apply the TEW on each In-111 emission separately in conjunction with the Tc-99m TEW in order to more completely correct for scatter. This implementation would require the use of 8-9 energy windows. If we were limited to 5 windows rather than 4, we would be able to separately window the two In-111 emissions,

decreasing the amount of detected scatter. This, in itself, may have been sufficient for proper In-111 quantification.

It may be beneficial to test the TEW methods across different positions and sizes of scatter windows. The  $\text{Scat}_{\text{high}}$  window is quite limited to its current position, as it is located between the 140keV Tc-99m emission and the 171keV In-111 emission. The  $\text{Scat}_{\text{low}}$  window could be moved further away from the Tc-99m peak in order to eliminate the detection of un-scattered Tc-99m photons in this window. Moving this window further away from the Tc-99m primary window comes at a cost, as photons detected in this window will have a broader spatial distribution than the scattered photons in the primary Tc-99m window. Increasing the scatter window sizes would reduce the effects of noise, but also change the spatial distribution of detected scatter. Decreasing the size of the scatter windows would further increase the noise in the scatter estimate.

Our scatter estimate and subsequent subtraction was carried out on the projections prior to reconstruction. It can also be included as part of the forward projection operation in the MLEM algorithm described in section 1.7.2. This method may decrease the noise in the scatter estimate, and also reduce the problems that occurred with the negative projection elements [21].

# 5 Conclusions and Future Directions

This chapter summarizes the important results of this work and discusses the impact that this work has on the field of small animal SPECT. The future of scatter correction in SPECT, and the impact of SPECT on field of small animal molecular imaging are also examined.

## 5.1 Conclusions

In the plastic cylinder phantom containing only In-111, the standard TEW left the least residual scatter, while the iterative TEW left significantly less residual scatter than the modified TEW in image space and in projection space.

In the plastic cylinder phantoms containing various  $\frac{Tc-99m}{In-111}$  activity fractions, In-111 cross-talk resulted in overestimations of Tc-99m activity by up to 80% in phantoms of mostly In-111. The standard TEW consistently overcompensated for scatter with  $\sim -10\%$  accuracy due to the presence of un-scattered counts in the scatter windows.

Applying the modified TEW in projection space resulted in a quantitative accuracy within 5% of truth in phantoms containing  $\frac{Tc-99m}{In-111}$  activity fractions greater than 0.5.

Applying the iterative TEW in projection space resulted in a quantitative accuracy within 5% of truth in phantoms containing activity fractions greater than 0.25, improving on the range of phantoms where the modified TEW was accurate. The iterative TEW was

significantly more accurate than the modified TEW (with 95% confidence) in phantoms of  $\frac{Tc-99m}{In-111}$  activity fractions less than and including 0.5.

*In vivo*, the presence of In-111 in the rat heart cavities as well as in the vasculature of the myocardium resulted in a mean overestimation of Tc-99m activity by  $24\% \pm 4\%$ . The standard TEW resulted in quantitative accuracy of  $-14\% \pm 2\%$ . The application of the modified TEW and iterative TEW both resulted in mean quantification within 5% of truth. The iterative TEW left significantly less residual scatter in the LV cavity ( $p < 0.001$ ), where only In-111 was present.

## 5.2 Future Directions

In single isotope SPECT, the necessity for scatter correction becomes apparent only after attenuation correction has been applied. Although the effects of scatter and attenuation are less noticeable in small animal SPECT than clinical SPECT, they are still incredibly important if the researcher is looking for reliable quantitative accuracy. The rise of the SPECT/CT combination both clinically and in small animal SPECT cameras allows for the creation of an accurate inhomogeneous attenuation map based on the CT acquisition. This permits accurate correction for attenuation to be incorporated directly into the iterative reconstruction algorithm.

Since accurate quantification is the direction that small animal research is headed, there is demand for improvement in fast and reliable techniques for scatter corrections. Dual isotope SPECT studies may result in unreliable qualitative and quantitative images of the lower-energy-isotope due to cross-talk, and therefore correction for cross-talk becomes

necessary even if the researcher is not looking for quantitative results. The TEW-based methods are not limited to this specific combination of isotopes, but due to the different emission energies, the effectiveness will differ depending on the isotopes used. For example, with Tc-99m (140keV) and Tl-201 (~70-80,135,167 keV) or I-123 (159keV), TEW-based approaches may not work very well due to significant overlap of the primary emissions due to the energy resolution (~10% FWHM) of NaI(Tl)-based detectors.

New detectors based on semiconductors have more recently become commercially available with a great improvement in energy resolution. They generally are optimal at very low temperatures, however, and lose practicality for clinical and research applications due to the costs associated with cooling. As an exception to this rule, Cadmium-Zinc-Telluride (CZT) detectors have been shown to be acceptable for clinical and pre-clinical use at room temperature with improvement in energy resolution by more than a factor of 2 for Tc-99m [69]. With this improvement in energy resolution, scatter and cross-talk are reduced and multiple-isotope studies become more attractive. Semiconductor detectors have their own unique problems, however. For example, CZT spectra contain a “tail” below the photo-peak, caused by incomplete charge collection in the CZT crystal [11]. Therefore, the introduction of these detectors necessitates new correction strategies.

In both detector types, simple methods based on the TEW have given somewhat reliable results, but due to the simplified approximations made by the TEW, there is a limit to the effectiveness of this method. The modified and iterative TEW discussed in this paper require very little time to operate and can be important in order to obtain improvements in quantitative accuracy in such dual-isotope experiments. As noticed in

the research of this thesis, the noise that is present in the TEW-based methods leads to a significant number of negatives in the corrected projections, particularly in regions of mostly In-111 (the higher-energy-isotope), leading to a loss of accuracy.

The future of scatter correction most likely involves the complete modelling (for example, MC-based modelling) of the scatter distribution. Although these methods tend to require much more computer power, they have the potential to provide robustness that simple approximation methods cannot compete with. Computer processors have been dramatically increasing in speed and with that, the obstacle to Monte-Carlo models is disappearing. Until this technology becomes more widespread, however, TEW-based corrections for scatter and cross-talk will continue to play a role in both clinical and pre-clinical SPECT.

The future of small animal research, which involves small-animal-specific SPECT imaging, is exceptionally bright. The use of small animal models has been essential in the development of specific drugs, genetic engineering and repairing damaged tissues. Small animal SPECT has played a role in furthering our understanding of disease process at the molecular level, rather than the anatomical level. SPECT plays a role in this research due to the large number of research targets that can be labelled with radioactive tracers [70]. Challenges in translation of animal models to human models exist, and a small animal model for disease will not always provide a clear picture for how a similar disease originates and progresses in humans [6]. Continuous improvement in spatial resolution, energy resolution, and scatter correction in SPECT will increase the accuracy of this research tool. This will aid in addressing these challenges and assist in translating the basic animal research of today into the clinical tools of tomorrow.

# References

- [1] S. Shcherbinin and A. Cellar, "Assessment of the severity of partial volume effects of two template-based correction methods in a SPECT/CT phantom experiment," *Physics of Medicine and Biology*, pp. 5355-5371, 2011.
- [2] J. L. Prince and J. M. Links, *Medical Imaging: Signals and Systems*, Upper Saddle River, NJ: Pearson Education, Inc., 2006.
- [3] N. Ahituv, E. M. Rubin and M. A. Nobrega, "Exploiting human-fish genome comparisons for deciphering gene regulation," *Human Molecular Genetics*, pp. R261-R266, 2004.
- [4] J. T. Eppig, J. E. Richardson, J. A. Kadin, C. J. Bult, J. A. Blake and Mouse Genome Database Group, "The Mouse Genome Database (MGD): premier model organism resource for mammalian genomics and genetics," *Nucleic Acids Reserach*, p. Vol 39. Database issue, 2011.
- [5] I. Ovcharenko, L. Stubbs and G. G. Loots, "Interpreting mammalian evolution using Fugu genome comparisons," *Genomics*, pp. 890-895, 2004.
- [6] D. J. Rowland and S. R. Cherry, "Small-Animal Preclinical Nuclear Medicine Instrumentation and Methodology," *Seminars in Nuclear Medicine*, pp. 38:209-222, 2008.
- [7] F.-C. Ma, P.-H. Lyu, Q. Yao, L. Yao and S.-J. Zhang, "Publication trends and knowledge maps of global translational medicine research," *Scientometrics*, pp. 98:221-246, 2014.
- [8] G. B. Saha, *Physics and Radiobiology of Nuclear Medicine*, New York City: Springer, 2006.
- [9] E. Vallejo, M. Morales, I. Sanchez, G. Sanchez, J. C. Alburez and D. Bialostozky, "Myocardial perfusion SPECT imaging in patients with myocardial bridging," *Journal of Nuclear Cardiology*, pp. 12(3): 318-323, 2005.
- [10] P. D. Acton, D. Thomas and R. Zhou, "Quantitative imaging of myocardial infarct in rats with high resolution pinhole SPECT," *The International Journal of*

- Cardiovascular Imaging*, pp. 22:429-434, 2006.
- [11] S. R. Cherry, J. A. Sorenson and M. E. Phelps, *Physics in Nuclear Medicine*, Fourth Edition, Philadelphia, PA: Elsevier Inc., 2012.
- [12] H. E. Johns and J. R. Cunningham, *The Physics of Radiology: Fourth Edition*, Springfield, Illinois: Charles C Thomas, 1983.
- [13] J. N. Aarsvold and M. N. Wernick, *Emission Tomography: The Fundamentals of PET and SPECT*, San Diego: Elsevier Academic Press, 2004.
- [14] Y. Li, J. Oldendick, O. E. Caesar and W. Chang, "Analytic Derivation of Pinhole Collimator Sensitivity for A General source Distribution," in *IEEE Nuclear Science Symposium Conference Record*, 2009.
- [15] T. Dai, S. Wang, Y. Liu, Z. Wu, Y. Jin and T. Ma, "Design and Feasibility Studies of a High-resolution and Low-cost Small Animal SPECT System," in *IEEE Nuclear Science Symposium Conference Record*, 2009.
- [16] R. Golestani, C. Wu, R. A. Tio, C. J. Zeebregts, A. D. Petrov, F. J. Beekman, R. A. J. O. Dierckx, H. H. Boersma and R. H. J. A. Slart, "Small-animal SPECT and SPECT/CT: application in cardiovascular research," *European Journal of Nuclear Medicine and Molecular Imaging*, pp. 37:1766-1777, 2010.
- [17] F. Beekman and F. van der Have, "The pinhole: gateway to ultra-high-resolution three-dimensional radionuclide imaging," *European Journal of Nuclear Medicine and Molecular Imaging*, pp. 34:151-161, 2007.
- [18] S. D. Metzler, R. J. Jaszczak, N. H. Patil, S. Vemulapalli, G. Akabani and B. B. Chin, "Molecular Imaging of Small Animals With a Triple-Head SPECT System Using Pinhole Collimation," *IEEE Transactions on Medical Imaging*, pp. 24:853-862, 2005.
- [19] S. D. Metzler, J. E. Bowsher, M. F. Smith and R. J. Jaszczak, "Analytic determination of pinhole collimator sensitivity with penetration," *IEEE Trans. Med. Imag.*, pp. 20:730-741, 2001.
- [20] D. Paix, "Pinhole imaging of gamma rays," *Physics of Medicine and Biology*, pp. 4:489-500, 1967.
- [21] B. F. Hutton, I. Buvat and F. J. Beekman, "Review and current status of SPECT scatter correction," *Physics in Medicine and Biology*, pp. R85-R112, 2011.

- [22] Y. H. Chung, T. Y. Song, J. H. Jung, G. Cho, Y. S. Choe, K.-H. Lee, S. E. Kim and B.-T. Kim, "Evaluation of Maximum-Likelihood Position Estimation With Poisson and Gaussian Noise Models in a Small Gamma Camera," *IEEE Transactions on Nuclear Science*, pp. 51:101-104, 2004.
- [23] S. P. Mok, Y. Wang and B. M. W. Tsui, "Design of a Novel Pinhole Collimator System for SPECT Imaging of Small Animals with Different Sizes," *IEEE Nuclear Science Symposium Conference Record*, pp. 2649-2652, 2005.
- [24] M. A. Kupinski and H. H. Barrett, *Small-Animal SPECT Imaging*, New York City: Springer Science + Business Media, Inc., 2005.
- [25] A. C. Kak and M. Slaney, *Principles of Computerized Tomographic Imaging*, Philadelphia: Society for Industrial and Applied Mathematics, 2001.
- [26] F. J. Beekman, C. Kamphuis, M. A. King, P. P. van Rijk and M. A. Viergever, "Improvement of image resolution and quantitative accuracy in clinical Single Photon Emission Computed Tomography," *Computerized Medical Imaging and Graphics*, vol. 25, pp. 135-146, 2001.
- [27] C.-L. Chen, Y. Wang, J. J. S. Lee and B. M. W. Tsui, "Toward Quantitative Small Animal Pinhole SPECT: Assessment of Quantitation Accuracy Prior to Image Compensations," *Molecular Imaging and Biology*, pp. 11:195-203, 2009.
- [28] J. A. Patton and T. G. Turkington, "SPECT/CT Physical Principles and Attenuation Correction," *Journal of Nuclear Medicine Technology*, pp. 36(1) 1-10, 2008.
- [29] S. C. Blankespoor, X. Wu, K. Kalki, J. K. Brown, H. R. Tang, C. E. Cann and B. H. Hasegawa, "Attenuation Correction of SPECT Using X-Ray CT on an Emission-Transmission CT System: Myocardial Perfusion Assessment," *IEEE Transactions on Nuclear Science*, pp. 43(4): 2263-2274, 1996.
- [30] J. Strydhorst and R. G. Wells, "Quantitative Multiplexed Multi-pinhole Small-Animal SPECT," Carleton University, Ottawa, 2013.
- [31] Bioscan, "NanoSPECT/CT Preclinical Imager: Technical Brochure & Specifications Guide," Bioscan, Inc., Washington, DC, 2007.
- [32] C. Wu, F. van der Have, B. Vastenhouw, R. A. J. O. Dierckx, A. M. J. Paans and F. J. Beekman, "Absolute quantitative total-body small-animal SPECT with focusing pinholes," *Eur J Nucl Med Mol Imaging*, pp. 37:2127-2135, 2010.

- [33] L.-T. Chang, "A Method for Attenuation Correction in Radionuclide Computed Tomography," *IEEE Transactions on nuclear Science*, pp. 25(1):638-643, 1978.
- [34] H. Zaidi and K. F. Koral, "Scatter modelling and compensation in emission tomography," *Eur J Nucl Med Mol Imaging*, pp. 31:761-782, 2004.
- [35] K. Ogawa, "Image distortion and correction in single photon emission CT," *Annals of Nuclear Medicine*, vol. 18, no. 3, pp. 171-185, 2004.
- [36] R. J. Jaszczyk, K. L. Greer, C. E. Floyd, C. C. Harris and E. R. Coleman, "Improved SPECT Quantification Using Compensation for Scattered Photons," *Journal of Nuclear Medicine*, pp. 25:893-900, 1984.
- [37] K. Ogawa, Y. Harata, T. Ichihara, A. Kubo and S. Hashimoto, "A Practical Method for Position-Dependent Compton-Scatter Correction in Single Photon Emission CT," *IEEE Transactions on Medical Imaging*, pp. 10(3):408-412, 1991.
- [38] T. Ichihara, K. Ogawa, N. Motomura, A. Kubo and S. Hashimoto, "Compton Scatter Compensation Using the Triple-Energy Window Method for Single- and Dual-Isotope SPECT," *Journal of Nuclear Medicine*, pp. 34:2216-2221, 1993.
- [39] M. A. King, D. J. deVries, T.-S. Pan, P. H. Pretorius and J. A. Case, "An investigation of the filtering of TEW scatter estimates used to compensate for scatter with ordered subset reconstructions," *IEEE Transactions on Nuclear Science*, pp. 1140-1145, 1997.
- [40] J. Feng, *IEEE Nuclear Science Symposium Conference Record*, pp. 1562-1566, vol.3, 2002.
- [41] J. Hashimoto, A. Kubo, T. Amano, Y. Fukuuchi, M. Nobutoku and T. Ichihara, "Scatter and Attenuation Correction in Technetium-99m Brain SPECT," *J Nucl Med.*, pp. 38:157-162, 1997.
- [42] J. Xiao, T. C. de Wit, S. G. Staelens and F. J. Beekman, "Evaluation of 3D Monte Carlo-Based Scatter Correction for 99m-Tc Cardiac Perfusion SPECT," *Journal of Nuclear Medicine*, pp. 1662-1669, 2006.
- [43] R. Timmins, "Master's Thesis Dissertation," 2012.
- [44] X. Zhu, M. A. Park and S. C. Moore, "Quantitative Simultaneous In-111/ Tc-99m Planar Imaging of the Foot," *IEEE Nuclear Science Symposium Conference Record*, pp. 2684-2687, 2006.

- [45] L. Qian and Z. Cao, "A convolution-subtraction technique to compensate for downscatter effects in simultaneous Tl-201/Tc-99m cardiac SPECT," *IEEE Transactions on Nuclear Science*, pp. 45(3):1207-1211, 1998.
- [46] R. G. Wells, A. Celler and R. Harrop, "Analytical Calculation of Photon Distributions in SPECT Projections," *IEEE Transactions on Nuclear Science*, pp. 45(6):3202-3214, 1998.
- [47] S. Shcherbinin, A. Celler, M. Trummer and T. Humphries, "An ADP-based Iterative Reconstruction Method for Simultaneous Technetium-99m/Iodine-123 SPECT Imaging," *IEEE Nuclear Science Symposium Conference Record*, pp. 2058-2062, 2006.
- [48] S. Schherbinin and A. Celler, "Simultaneous Crosstalk Compensation for a ROI Activity Estimation in Dual-Isotope SPECT Imaging," *IEEE Nuclear Science Symposium Conference Record*, pp. 3256-3261, 2009.
- [49] H. W. A. M. de Jong, F. J. Beekman, M. A. Viergever and P. P. va Rijk, "Simultaneous 99mTc/201Tl dual-isotope SPET with Monte Carlo-based downscatter correction," *European Journal of Nuclear Medicine*, vol. 29, no. 8, pp. 1063-1071, 2002.
- [50] Y. K. Dewaraja, M. Ljungberg and J. A. Fessler, "3-D Monte Carlo-Based Scatter Compensation in Quantitative I-131 SPECT Reconstruction," *IEEE Transactions on Nuclear Science*, pp. 53(1):181-188, 2006.
- [51] M. I. Karamat and T. H. Farncombe, "Simultaneous 99mTc/111In SPECT Image Reconstruction using Convolution based Forced Detection," *IEEE Nuclear Science Symposium Conference Record*, pp. 2625-2631, 2011.
- [52] H. W. A. M. de Jong, E. T. P. Slijpen and F. J. Beekman, "Acceleration of Monte Carlo SPECT Simulation using Convolution-Based Forced Detection," *IEEE Transactions on Nuclear Science*, vol. 48, no. 1, pp. 58-64, 2001.
- [53] J. Ouyang, G. El Fakhri, S. C. Moore and M. F. Kijewski, "Fast Monte Carlo Simulation Based Joint Iterative Reconstruction for Simultaneous 99mTc/123I SPECT Imaging," *2006 IEEE Nuclear Science Symposium Conference Record*, pp. 2251-2256, 2006.
- [54] J. Ouyang, G. El Fakhri and S. C. Moore, "Improved activity estimation with MC-JOSEM versus TEW-JOSEM in In111 SPECT," *Medical Physics*, pp. 35(5):2029-

2040, 2008.

- [55] E. C. Frey and B. M. W. Tsui, "A New Method for Modeling the Spatially-Variant, Object-Dependent Scatter Response Function in SPECT," *IEEE*, pp. 1082-1086, 1997.
- [56] D. Devakumar, X. He and E. Frey, "Comparative Assessment of ESSE and DEW Scatter Compensation Methods for Myocardial Perfusion SPECT," *IEEE Nuclear Science Symposium Conference Record*, pp. 4472-4474, 2007.
- [57] M. Narayanan, P. H. Pretorius, S. T. Dahlberg, J. A. Leppo, N. Botkin, J. Krasnow, W. Berndt, E. C. Frey and M. A. King, "Evaluation of Scatter Compensation Strategies and Their Impact on Human Detection Performance Tc-99m Myocardial Perfusion Imaging," *IEEE Transactions on Nuclear Science*, pp. 50(5):1522-1527, 2003.
- [58] A. Sitek, E. V. R. Di Bella, G. T. Gullberg and R. H. Huesman, "Removal of liver activity contamination in teboroxime dynamic cardiac SPECT imaging with the use of factor analysis," *Journal of Nuclear Cardiology*, vol. 9, no. 2, pp. 197-205, 2002.
- [59] K. Erlandsson, I. Buvat, P. H. Pretorius, B. A. Thomas and B. Hutton, "A review of partial volume correction techniques for emission tomography and their applications in neurology, cardiology and oncology," *Physics in Medicine and Biology*, vol. 57, pp. R119-R159, 2012.
- [60] S. Shcherbinin, S. Chamoiseau and A. Cellar, "Simulation-based reconstruction of absolute activities from the 99mTc/111In dual-isotope SPECT/CT: phantom experiments and imaging of neuroendocrine tumors," *Physics in Medicine and Biology*, pp. 58:3339-3357, 2013.
- [61] S. Deleye, R. Van Hoken, J. Verhaeghe, S. Vandenberghe, S. Stroobants and S. Staelens, "Performance evaluation of small-animal multipinhole microSPECT scanners for mouse imaging," *Eur J Nucl Med Mol Imaging*, pp. 40:744-758, 2013.
- [62] B. F. Hutton, A. Olsson, S. Som, K. Erlandsson and M. Braun, "Reducing the influence of spatial resolution to improve quantitative accuracy in emission tomography: A comparison of potential strategies," *Nuclera Instruments and Methods in Physics Research*, pp. 462-466, 2006.
- [63] K. Inoue, H. Ito, R. Goto, M. Nakagawa, K. Shigeo, T. Sato, K. Sato and H. Fukuda, "Apparent CBF decrease with normal aging due to partial volume effects: MR-based partial volume correction on CBF SPECT," *Annals of Nuclear Medicine*, pp.

19(4):283-290, 2005.

- [64] J. H. Strydhorst, F. H. Leenen, T. D. Ruddy and G. Wells, "Reproducibility of Serial Left Ventricle Perfusion, Volume, and Ejection Fraction Measurements Using Multiplexed Multipinhole SPECT in Healthy Rats and Rats After Myocardial Infarction," *The Journal of Nuclear Medicine*, pp. 52(8):1285-1292, 2011.
- [65] "Eppendorf Flex Tubes," Eppendorf, [Online]. Available: [http://eshop.eppendorf.ca/products/Eppendorf\\_Flex-Tube\\_microcentrifuge\\_tube](http://eshop.eppendorf.ca/products/Eppendorf_Flex-Tube_microcentrifuge_tube). [Accessed 20 July 2014].
- [66] "Instrument Manual: WIZARD Gamma Counter," PerkinElmer Life and Analytical Sciences, Turku, Finland, 2008.
- [67] "CRC-25R Owner's Manual," Capintec, Inc., Ramsey, NJ, 2007.
- [68] L. A. Feldkamp and J. W. Kress, "Practical cone-beam algorithm," *J Opt Soc Am*, pp. 612-619, 1984.
- [69] D. J. Wagenaar, J. Zhang, T. Kazules, T. Vandehei, E. Bolle, S. Chowdhury, K. Parnham and B. E. Patt, "In Vivo Dual-Isotope SPECT Imaging with Improved Energy Resolution," *IEEE Nuclear Science Symposium Conference Record*, pp. 3821-3826, 2006.
- [70] R. Weissleder and U. Mahmood, "Molecular Imaging," *Radiology*, pp. 219:316-333, 2001.
- [71] R. C. Thompson, "The problem of radiotracer abdominal activity in myocardial perfusion imaging studies," *Journal of Nuclear Cardiology*, pp. 159-161, 2008.
- [72] "Medical Isotopes-Frequently Asked Questions," 31 08 2009. [Online]. Available: <http://www.hc-sc.gc.ca/dhp-mps/brgtherap/activit/fs-fi/isotopes-med-faq-eng.php>. [Accessed 01 07 2014].
- [73] R. van Noorden, "The Medical Testing Crisis," *Nature*, pp. 504:202-204, 2013.
- [74] K. Yoshinaga, B. J. W. Chow, K. Williams, L. Chen, R. A. de Kemp, L. Garrard, A. L.-T. Szeto, M. Aung, R. A. Davies, T. D. Ruddy and R. S. B. Beanlands, "What is the Prognostic Value of Myocardial Perfusion Imaging Using Rubidium-82 Positron Emission Tomography?," *Journal of the American College of Cardiology*, pp. 48(5):1029-1039, 2006.

- [75] H. Farhad, V. Dunet, K. Bachelard, G. Allenbach, P. A. Kaufmann and J. O. Prior, "Added prognostic value of myocardial blood flow quantitation in rubidium-82 positron emission tomography imaging," *European Heart Journal-Cardiovascular Imaging*, pp. 14:1203-1210, 2013.
- [76] H. W. de Jong and F. J. Beekman, "Rapid SPECT simulation of downscatter in non-uniform media," *Physics in Medicine and Biology*, vol. 46, pp. 621-635, 2001.